BEHAVIORAL MODULATION OF SUPRAMOLECULAR ASSEMBLIES VIA COVALENT AND NON-COVALENT INTERFACIAL TRANSFORMATIONS

A Dissertation Presented

by

ANN CANDICE FERNANDEZ

Submitted to the Graduate School of University of Massachusetts-Amherst in partial fulfillment of the requirements for the degree of

DOCTOR OF PHILOSOPHY

September 2021

Chemistry

BEHAVIORAL MODULATION OF SUPRAMOLECULAR ASSEMBLIES VIA COVALENT AND NON-COVALENT INTERFACIAL TRANSFORMATIONS

A Dissertation Presented

by

ANN CANDICE FERNANDEZ

Approved as to style and content by

DocuSigned by:
S. Thai Thayumanavan
5AE72FB729054E4...
S. Thayumanavan, Chair

DocuSigned by:
Min Chen
DCB539E7A2A44E3...
Min Chen, Member

DocuSigned by:
Kevin Kittilstved
ED720E0B49494C7...
Kevin Kittilstved, Member

DocuSigned by:
Maria Santore
B84E83B7791D443...
Maria Santore, Member

DocuSigned by:
Ricardo Metz
A6F1B347E80E447...
Ricardo B. Metz, Department Head
Chemistry Department

DEDICATION

To my parents, for their unconditional love and constant support.

ACKNOWLEDGEMENTS

Firstly, I would like to thank Prof. S. Thayumanavan, for being a wonderful mentor throughout the course of my Ph.D. Your guidance was effective in shaping me as a critical thinker and a good science communicator. Thank you for providing me with numerous opportunities to help me grow, diversify my skills and work as an independent scientist. Additionally, I wouldn't have been able get this far without my committee members, Professors Min Chen, Mike Knapp, Maria Santore and Kevin Kittilstved. Your insightful feedback and constructive criticism during my candidacy examinations were all immensely beneficial to progress my work in the right direction.

I am grateful to the members of the Thai lab, both past and present, whom I had the absolute pleasure to work with. Thank you, Dr. Celia Homyak, for taking me under your wing when I first joined the group, and for being such an incredible first mentor. You were instrumental in developing my technical skills, especially in microscopy, and I am ever grateful for our time together. Thank you. Dr. Jiaming Zhuang, for your in-depth insight and feedback on the TMAc project. I am certainly appreciative of all your ideas and expertise that helped me carry the TMAc, as well as other projects forward. Thank you, Dr. Manisha Shivrayan, for being extremely helpful as a collaborator for the CCI projects, and a friend these past years. Thank you, Dr. Francesca Anson, for your perspective on the biological side of my projects. Dr. Thameez Koyasseril and Dr. Vikash Kumar, I am thankful to you both for your mentorship and friendship. Ritam Das, Pintu Kanjilal and Jithu Krishna, thank you all, for your generous support to carry my projects forward. Thank you, Karen Hakala, for being such a wonderful person and for constantly being there to support us in the Thai lab. Thank you, Leyla Keough, for all the administrative support you extended during your time in the Thai lab for the CCI projects.

I wouldn't have made it this far if it weren't for my friends at High Street - Steph Le, Jenny Huynh, Kaitlynn Chhe, Ari Chattopadhyay, and Jessa Makabenta. Thank you for all the fun, giggles, food, movie nights, silly banter, and of course, boba. Theo Prachyathipsakul and Roshni John, thank you, for all your emotional support. I am grateful to you all for helping me through this journey. I will certainly cherish my relationship with you all for years to come.

To my constant cheerleaders in life – my parents, Cyril Fernandez and Shirley Fernandez, words cannot express my love and appreciation for you both. Thank you for believing in me, and for making me the person that I am today. You are both vital to my success. To my baby sister, Cathy Fernandez, thank you for making me laugh and helping me get through this challenging adventure. Fr. Zack Skariya and Aleyamma Skariya, I am immensely grateful to you both for your constant love and support. And finally, to my fiancé and best-friend, Ashlin Skariya, thank you for being my rock and for encouraging me every step of the way all these years. I truly couldn't have done this without you.

ABSTRACT

BEHAVIORAL MODULATION OF SUPRAMOLECULAR ASSEMBLIES VIA COVALENT AND NON-COVALENT INTERFACIAL TRANSFORMATIONS

SEPTEMBER 2021

ANN CANDICE FERNANDEZ

B.Sc. and M.Sc., STELLA MARIS COLLEGE

Ph.D., UNIVERSITY OF MASSACHUSETTS AMHERST

Directed by: Professor S. Thayumanavan

There are several molecular level mechanisms at the origin of biological functions that serve as inspiration for the development of the "next generation" of materials that display adaptive and interactive properties. However, it will take time for synthetic materials to approach the level of complexity, robustness, and adaptability of biological systems. Although there are switchable platforms that respond via sensitized molecular components, there are currently no examples of materials that truly possess the type of autonomous behavior seen in biological systems. Even though these concepts are common in living organisms, their translation into a synthetic platform remains challenging to this day. The development of such systems requires the unraveling of the structural and energetic bases that underlie autonomous processes at the molecular level, and this work focuses on fundamentally understanding some of these concepts. By bringing about covalent and non-covalent transformations at the interface of supramolecular assemblies, we have investigated how these modifications can cause systemic energy changes, which in turn dictates overall outcome of these interfacial modifications. An insight into these processes would support the future development of supramolecular platforms that display autonomous behavior.

TABLE OF CONTENTS

Page

LIST OF TABLES

Page

LIST OF FIGURES

Page

LIST OF SCHEMES

Page

CHAPTER 1

1.1 INTRODUCTION

Living systems respond to changes in external energy to reconfigure themselves and perform functions via signal amplification and self-replication.[1] Nature has engineered flawless responsive networks wherein an interplay of molecular recognition, self-organization, and response activation by a vast array of biomolecules leads to the formation of intricate biological networks for autonomous control and coordination.[1-2] The immune system, for example, relays information by either secreting compartmentalized signaling molecules from cellular components, producing downstream effects,[2-4] or directly via cell-cell interfacial contact, mediated by covalent or non-covalent interactions.[5-9] These processes are also characterized by the presence of feedback loops, tightly controlled by chemical signals to form regulatory networks of independent sub-oscillators with different characteristic timescales, making efficient communication possible. [10-11]

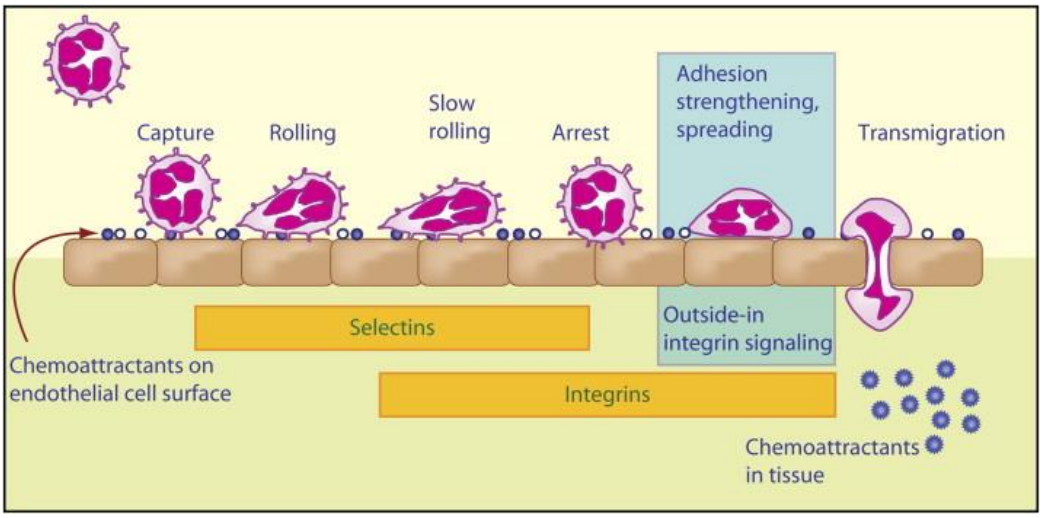

FIGURE 1.1: Leucocyte surface rolling and adhesion cascade triggered by a regulatory network of signals (image reused from Reference 36 in this section with copyright permission).

Another feature exhibited by highly evolved autonomously functioning systems is the ability to move.[12-13] Motion requires the conversion of energy into work by biological molecular motors, optimized for specific functions, such as intracellular transport, micro-propulsion, or macroscopic

motion. The property of adaptation, which is the capacity to sense and respond to environmental cues, also facilitates survival in autonomous organisms. All these complex mechanisms orchestrated by feedback loops rely on non-equilibrium dynamics and involves constant energy dissipation and kinetic control.[12]

The process of self-assembly, where individual functional components come together to form a higher order structure, is quite inspiring. All forms of life contain self-assembling units and a fundamental understanding of the process can give us a better insight into the nuances of biological processes.[14] During self-assembly, complex structures can be "autonomously manufactured" in a simple bottom-up fashion and seems simple, however, synthesizing a functional system can be challenging since the individual components need to be designed and programmed in such a manner that they can orient themselves correctly during the self-assembly process.[15-16] Stimuli-sensitive units that respond to various stimuli such as temperature, pH and light can also be incorporated into these building blocks, making it possible to use supramolecular assemblies for various nanomedicine-based and biomimetic applications.[38, 49, 52] With self-assembly, it has also been possible to incorporate interactions that may seem "disjoint" into a single system by combining individual components capable of displaying multiple properties within the same system.[17-20] Progress in the synthesis of intrinsically functional building blocks, and hybridization with inorganic or organic or biological moieties have all greatly contributed to reach a high level of structural control through molecular design.[21-22] As a result, significant progress has been made in the field of self-assembled micelles and vesicles with bioinspired functions such as compartmentalization, transport, catalysis, motion, and self-replication using triggerable/responsive materials.[14] However, we are far from achieving the level of complexity seen in biological platforms, and the development of synthetic materials that exhibit fully

autonomous behavior remains a challenge. Due to lack in design principles required to synthetically "manufacture" such platforms, this work focuses on understanding fundamentally, the structural and energetic effects that underlie autonomous processes at the molecular level by using responsive surfactant-, lipid- and oligomer-based supramolecular assemblies. A deeper understanding of these processes can guide the future development of artificial materials that can exhibit truly autonomous behavior and can have implications in nanomedicine, agriculture, controlled release, and sensing applications.

1.2 SUPRAMOLECULAR SELF-ASSEMBLY

As noted in the previous section, self-assembly is a process by which individual functional molecules come together spontaneously to form higher ordered structures.[14-16] The self-assembly process at the molecular level is driven by factors such as shape, charge, or polarizability of the units, and subsequently determines the nature of attractive or repulsive forces. These forces are predominantly non-covalent interactions, such as $\boldsymbol{\pi}$-$\boldsymbol{\pi}$ and van Der Waals interactions, electrostatic forces, hydrogen bonding, metal coordination, and hydrophobic interactions.[40-42] In addition to these, self-assembly can also make use of kinetically labile bonds to bring about equilibration between aggregated and non-aggregated states, and providing the system responsive properties to various stimuli.[17-20] The relative volume and nature of the building blocks also dictate the shape of the assembly that is formed and is associated with an important parameter known as the critical aggregation concentration (CAC).[43] It is important to note that the CAC is usually large for amphiphilic building blocks such as small molecule surfactants and exhibits low mechanical stability. However, macromolecules such as amphiphilic polymers display low CAC values, and higher stability is often seen in these systems.[43] Self-assemblies also have the capacity to

encapsulate hydrophilic and/or hydrophilic contents, and have vast implications in therapeutics, diagnostics, and controlled release applications.[17-20]

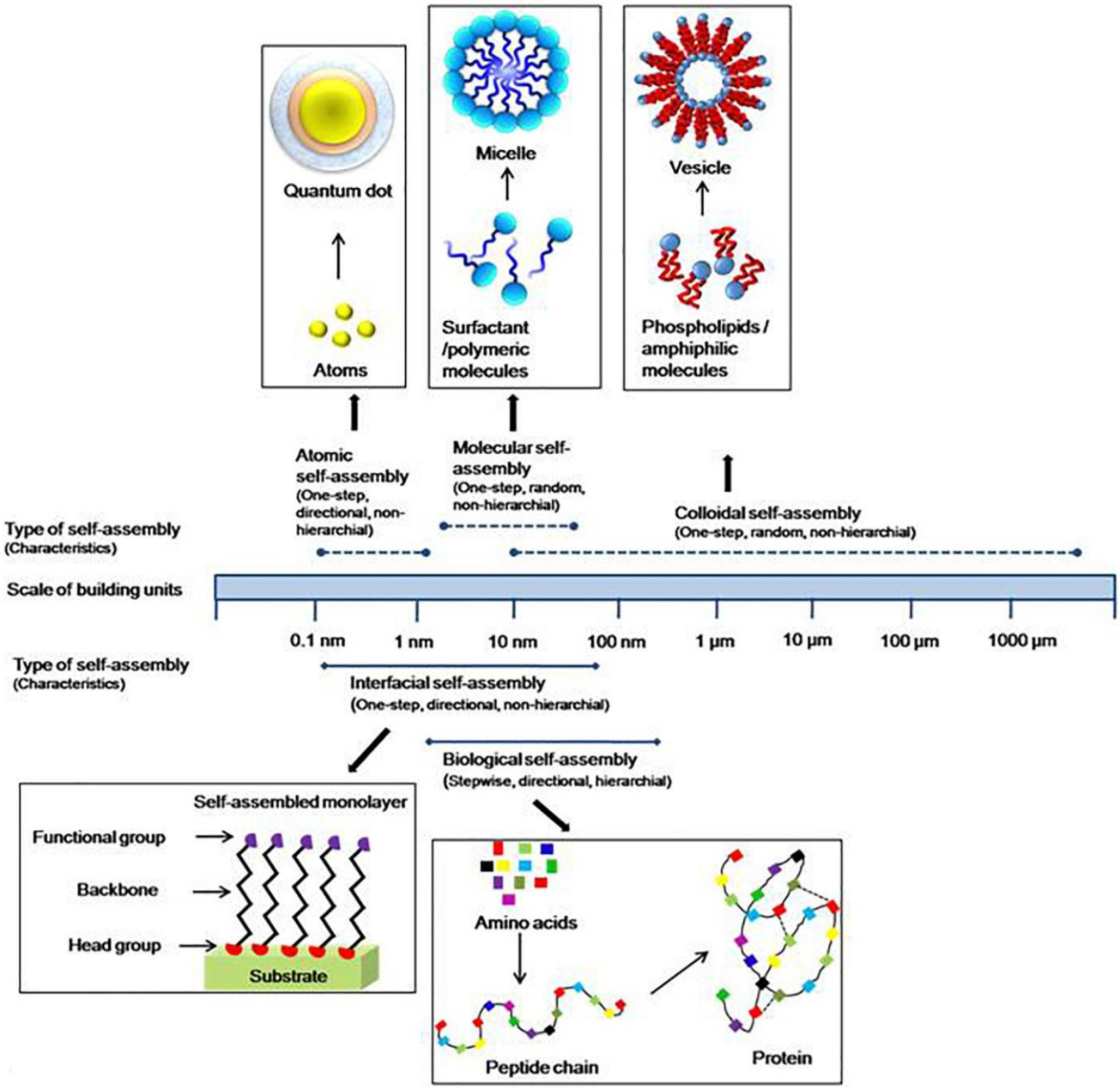

FIGURE 1.2: Self-assembly process based on the nature of building blocks (image reused from Reference 39 in this section with copyright permission).

1.3 STIMULI-RESPONSIVE SUPRAMOLECULAR PLATFORMS

Natural systems use a simple repertoire of building blocks such as lipids and polymers to perform sophisticated functions such as self-healing, signal amplification, homeostasis, and camouflage.[5-13] These are a result of subtle environmental changes, and materials that mimic these natural processes find a myriad of useful applications. Stimuli responsive assemblies built from small molecule surfactants, lipids and polymers, and sensitized to triggers such as pH, temperature, light, redox and enzyme is an emerging strategy for applications pertinent to areas such as nanomedicine, agriculture, sensing, purification, and tissue engineering.[17-20] For example, in drug delivery, changes in pH and redox can be used to initiate morphology or stability changes in the self-assemblies, thereby allowing them to deliver encapsulated bioactive contents at the site of interest.[17-20] Similarly, self-assemblies sensitized to various enzymes, can lead to a triggered release in environments containing the specific enzyme, or initiate an uptake process into a cell through complementary binding to the enzyme. Depending on the type of trigger used, covalent as well as non-covalent modifications can be made in the self-assembly platform to induce desired outcome.[12,14, 17-20]

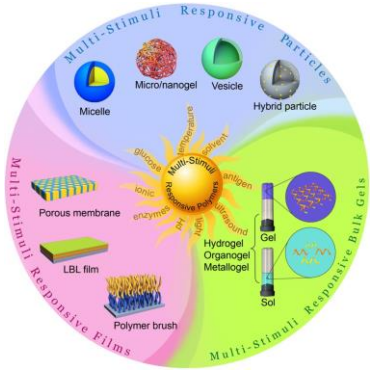

FIGURE 1.3: Stimuli-responsive materials (image reused from Reference 38 in this section with copyright permission).

1.4 SELF-ASSEMBLY PROCESSES OUTSIDE CONDITIONS OF EQUILIBRIUM

The process of self-assembly in systems is under thermodynamic equilibrium and the process is controlled by various thermodynamic parameters.[14] This has been studied for decades,

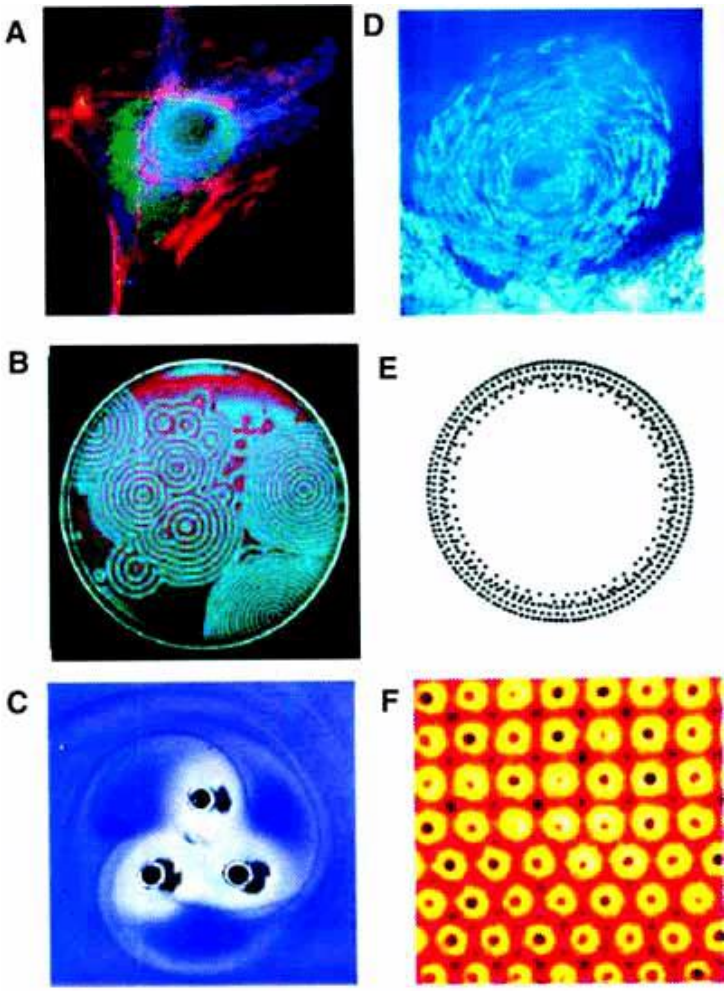

FIGURE 1.4: Examples of dynamic self-assembly. a) An optical micrograph of a cell with fluorescently labelled cytoskeleton and nucleus; microtubules (~24 nm in diameter) are colored red. b) Reaction-diffusion waves in a Belousov-Zabatinski reaction in a 3.5-inch Petri dish. c) A simple aggregate of three millimeter-sized, rotating, magnetized disks interacting with one another via vortex-vortex interactions. d) A school of fish. e) Concentric rings formed by charged metallic beads 1 mm in diameter rolling in circular paths on a dielectric support. f) Convection cells formed above a micropatterned metallic support. The distance between the centers of the cells is ~2 mm. (Figure and figure title reused from Reference 14 in this section with copyright permission)

however, the conditions of thermodynamic equilibrium do not include the order maintained in a system at the cost of an externally delivered energy. Biological systems exhibiting adaptive and self-regulated behavior rely on dynamic self-assembly.[24] Stable non-equilibrium structures are maintained in a steady state by a constant supply of energy, and subsequently dissipated via entropy producing processes associated with the system. The highly complex but ordered characteristics of these systems lies greatly under the control of various nonlinear processes, and this could provide clues for constructing autonomous artificial systems.[12] Relatively little is known about the principles of dynamic self-assembly, and the ways by which it can be extended into synthetic platforms.[14] Reconfiguration processes occurring under external energy are promising, since self-assembly can now be thought of outside the conditions of equilibrium to create life-like and intelligent autonomously functioning materials which are sensitive, adaptable, and capable of evolving. Adaptive and autonomous devices, and sensors are certainly one key aspect of autonomous materials, while implants and biomaterials that can actively adapt and interact with the body provide other great opportunities for complex molecular systems.

1.5 SELF-REGULATION IN ARTIFICIAL SYSTEMS

Inspired by the phenomenon of self-regulation in biological processes, smart polymers and gels that utilize chemical oscillators have been developed and are reminiscent of the self-regulation behavior seen in Nature.[14] Another example of a system that demonstrates primitive self-regulation are alloys that exhibit shape alteration in response to temperature changes. Hydrogels combined with embedded microfibrils, inorganic nanoparticles, nanosheets and surface attached micropillars have also been designed, however they rely on passive actuation mechanisms.[44] In addition to assemblies that can be triggered by a single stimulus, there has been interest in developing systems

that can be triggered by a combination of two or more triggers, to form logic gates. While there are several reports developed using small molecules, supramolecular logic gates are still relatively limited. Examples include logic-gated systems that use fuel driven transient self-assemblies or temperature-responsive structures to undergo tailored chemo-mechanical oscillations in response to a limited set of stimuli.[9-15, 45]

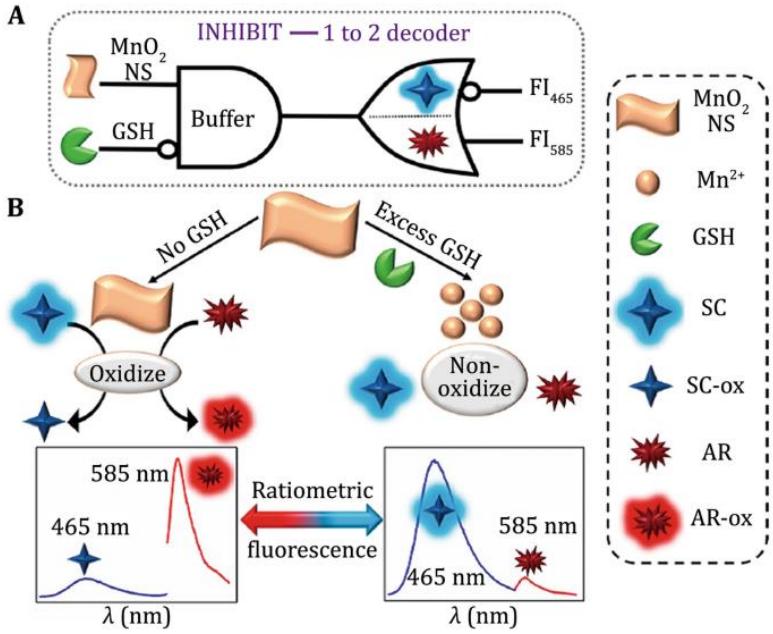

FIGURE 1.5: Example of a logic-gated system to produce an output (image reused from Reference 37 in this section with copyright permission).

Most systems currently inspired by the self-regulation behavior seen in biological systems utilize positive and negative feedback loops, where multiple components are introduced to control a single system.[27–33] While engineering such feedback loops, compartmentalization, immobilization and control of diffusion of reactants and catalysts are also important to gain a deeper understanding of feedback mechanisms extending beyond the possibilities of homogenous bulk solutions to obtain the intricacy seen in biological platforms.[23] While there has been success in the direction of logic operations, computational algorithms, sensing and communication, some

of the more unsolved fundamental challenges refer to concepts of self-replication and self-evolution. [34-35] When it comes to diverse molecular effectors of these mechanisms, characteristic time scales must be defined, and as a result, engineering time delays is crucial.[14] Towards real-life applications, it is also desirable to foster the integration of established and emerging concepts into materials. However, compared to complex biosystems which have taken centuries to evolve as robust self-regulated networks, artificial systems that have been developed so far are greatly simplified. Fully autonomous, synthetic supramolecular systems capable of exhibiting properties seen in biological platforms via complex molecular recognition events are rare.

1.6 THESIS OVERVIEW:

There is an increasing number of molecular mechanisms at the origin of various biological functions that serve as a source of inspiration for the development of next-generation molecular materials with adaptive and interactive properties. Although it will take time for synthetic materials to approach the level of complexity, robustness and adaptability of biological systems, the goal is certainly achievable. Currently, there are switchable materials that can function via responsive molecular components; however, they do not possess truly autonomous behavior. The switching of states is dependent on an outside trigger, and aside from simple relaxation events, autonomy is largely absent without the trigger.[12,14, 48-50] For such synthetic materials to be truly life-like and autonomous, the capabilities to accumulate work, sense, adapt and communicate would have to depend on dissipative chemical systems and integrated via efficient feedback loops. The creation of autonomous structures is, thus, a grand challenge in Chemistry. The development of far-from-equilibrium systems that are fueled and feedback-controlled could bring about the next disruptive change in soft matter property profiles. Such systems should go beyond passive responsiveness to

external signals and be able to actively orchestrate material dynamics and properties in a timely manner before it comes out of the out-of-equilibrium reaction state and start to get controlled by internal dynamics. While such concepts are common in living organisms, their synthetic design remains challenging. In this work, we aim for a more general strategy: rather than developing systems that perform a targeted function, we focus on fundamentally unraveling the structural and energetic bases that underlie autonomous processes at the molecular level. Keeping this in mind, Chapter 2 discusses the design of a surfactant-based supramolecular platform that responds via covalent interfacial modifications. We also incorporate important features seen in biological systems to this platform - kinetic control, the ability to interact with complementary assemblies, the ability to produce an output under out-of-equilibrium conditions, and finally the conversion of microscopic interactions to macroscopically observable phenomena. In Chapter 3, we use non-covalent interactions in lipid-based supramolecular platforms to understand underlying energetics involved in receptor-mediated nanoparticle interactions that are specific in nature. The effects of nanoparticle size, overall effects of receptor-ligand concentration/density are discussed in detail. Chapter 4 is inspired by the chemotactic properties exhibited by living organisms, and we have sought to explore how oligomeric supramolecular assemblies interact on a surface. We have investigated the effect of systemic energy changes when an assembly interacts with a complementary surface and provided insight into the rational design of synthetic supramolecular platforms to achieve controllable chemotaxis. Chapter 5 provides a summary of findings, along with future research directions.

1.7 REFERENCES

1. Gnesotto, F.S.; Mura, F.; Gladrow, J.; Broedersz, C. P. Broken Detailed Balance and Non-Equilibrium Dynamics in Living Systems: A Review. *Rep. Prog. Phys.* **2018**, *81*, 1-32.
2. Charitou, T.; Bryan, K.; Lynn, D. J. Using Biological Networks to Integrate, Visualize and Analyze Genomics Data. *Gen. Sel. Evol*. **2016**, *48*, 27-38.
3. Shen, H.; Miller, J. F.; Fan, X.; Kolwyck, D.; Ahmed, R.; Harty, J. T. Compartmentalization of Bacterial Antigens: Differential Effects on Priming of CD8 T-cells and Protective Immunity. *Cell*, **1992,** *92*, 535-545.
4. Dykstra, M.; Cherukuri, A.; Sohn, H.; Tzeng, S.-J.; Pierce, S. Location is Everything: Lipid Rafts and Immune Cell Signaling. *Ann. Rev. Immunol.* **2003,** *21*, 457-481.
5. Terenzio, M.; Schiavo, G.; Fainzilber, M. Compartmentalized Signaling in Neurons: From Cell biology to Neuroscience. *Neuron*, **2017,** *96*, 667-679.
6. Clark, R.; Judd, J.; Lasek-Nesselquist, E.; Montgomery, S.A.; Hoffmann, J. G.; Derbyshire, K. M.; Gray, T. A. Direct Cell-cell Contact Activates SigN to Express the ESX-4 Secretion System in *Mycobacterium smegmatis*. *PNAS.* **2018,** *115*, 6595-6603.
7. Springer, T. A. Adhesion Receptors of the Immune System. *Nature*, **1990**, *346*, 425-434.
8. Furuya, M.; Kikuta, J.; Fujimori, S.; Seno, S.; Maeda, H.; Shirazaki, M.; Uenaka, M.; Mizuno, Y.; Iwamoto, Y.; Morimoto, A.; Hashmoto, K.; Ito, T.; Isogai, Y.; Kashii, M.; Kaito, T.; Ohba, S.; Chung, U.; Lichtler, A.; Kikuchi, K.; Matsuda, H.; Yoshikawa, H.; Ishii, M. Direct Cell-Cell Contact between Mature Osteoblasts and Osteoclasts Dynamically Controls their Functions in vivo. *Nat. Commun*., **2018**, *9,* 300-311.
9. Sanchez-Madrid, F.; del Pozo, M.A. Leukocyte Polarization in Cell Migration and Immune Interactions. *EMBO. J.* **1999**, *18*, 501-511 (1999).

10. Brandman, O.; Ferrell, J. E.; Li, R.; Meyer, T. Interlinked Fast and Slow Positive Feedback Loops Drive Reliable Cell Decisions. *Science*, **2005,** *310,* 496-498.

11. Avrahm, R.; Yarden, Y. Feedback Regulation of EGFR Signaling: Decision Making by Early and Delayed Loops. *Nat. Rev. Mol. Cell Biol.* **2011,** *12,* 104-117.

12. Merindol, R.; Walther, A. Materials Learning from Life: Concepts for Active, Adaptive and Autonomous Molecular Systems. *Chem. Soc. Rev.* **2017,** *46,* 5588-5619.

13. Colberg, P. H.; Reigh, S. Y.; Robertson, B.; Kapral, R. Chemistry in Motion: Tiny Synthetic Motors. *Acc. Chem. Res.* **2014,** *47,* 3504-3511.

14. Whitesides, G. M.; Grzybowski, B. A. Self-Assembly at All Scales. *Science*, **2002**, *295*, 2418-2421.

15. Lehn, J. M. Towards Self-Organization and Complex Matter. *Science*, **2002**, *295*, 2400-2403.

16. Jones, M. R.; Mirkin, C. A. Self-Assembly Gets New Direction. *Nature*, **2012**, *491*, 42-43.

17. Siegel, R. Stimuli Sensitive Polymers and Self-regulated Drug Delivery Systems: A Very Partial Review. *J. Control. Release.* **2014,** *190,* 337-351.

18. Moreira, A. F.; Dias, D. R. Correia, I. J. Stimuli-Responsive Mesoporous Silica Nanoparticles for Cancer Therapy: A Review. *Micropor. Mesopor. Mat.* **2016,** *236,* 141-157.

19. Torchilin, V. Multifunctional, Stimuli-Sensitive Nanoparticulate Systems for Drug Delivery. *Nat. Rev. Drug Discov.* **2014,** *13***,** 813–827.

20. Pasparakis, G.; Vamvakaki, M. Multiresponsive Polymers: Nano-sized Assemblies, Stimuli-Sensitive Gels and Smart Surfaces. *Polym. Chem.* **2011,** *2,* 1234-1248.

21. Witt, D.; Klajn, R.; Barski, P.; Grzybowski, B. A. Applications, Properties and Synthesis of ω-Functionalized n-Alkanethiols and Disulfides – The Building Blocks of Self-Assembled Monolayers. *Curr. Org. Chem.*, **2004**, *8,* 1763-1797.

22. Love, J. C.; Estroff, L. A.; Kriebel, J. K.; Nuzzo, R. G.; Whitesides, G. M. Self-assembled Monolayers of Thiolates on Metals as a Form of Nanotechnology. *Chem. Rev.*, **2005**, *105*, 1103-1170.

23. Tu, Y.; Peng, F.; Adawy,A.; Men, Y.; Abdelmohsen, L. K. E. A.; Wilson, D. A. Mimicking the Cell: Bio-Inspired Functions of Supramolecular Assemblies. *Chem. Rev.* **2016,** *2,* 2023-2078.

24. Grzybowski, B. A.; Fitzner, K. Paczesny, J.; Granick, S. From Dynamic Self-Assembly to Networked Chemical Systems. *Chem. Soc. Rev.,* **2017**, *46*, 5647

25. Cheng, C.; McGoniga, P. R.; Stoddary, J. F; Astumian, R. D. Design and Synthesis of Non-Equilibrium Systems. Design and Synthesis of Non-Equilibrium Systems. *ACS Nano.* **2015,** *9,* 8672-8688.

26. Orbán, M.; Dekepper, P.; Epstein, I. R.; Kustin, K. New Family of Homogenous Chemical Oscillators: Chlorite-Iodate-Substrate. *Nature* **1981**, *292*, 816-818.

27. Rábai, G.; Beck, M. T.; Kustin, K.; Epstein, I. R. Sustained and Damped pH Oscillation in the Periodate-Thiosulfate Reaction in a Continuous-Flow Stirred Tank Reactor. *J. Phys. Chem.*, **1989**, *93*, 2853-2858.

28. Orbán, M.; Dekepper, P.; Epstein, I. R. Minimal Bromate Oscillator Bromate-Bromide-Catalyst. *J. Am. Chem. Soc.*, **1982**, *104*, 2657-2658.

29. Aviram, A. Molecules for Memory, Logic, and Amplification. *J. Am. Chem. Soc.* **1988,** *110,* 5687-5692.

30. De Silva, A. P.; Uchiyama, S. Molecular Logic and Computing. Nat. Nanotech. **2007,** *2,* 399-410.

31. Andreasson, J.; Pischel, U. Molecules with a Sense of Logic: A progress Report. *Chem. Soc. Rev.*, **2015**, *44*, 1053-1069.

32. Katz, E.; Privman, V. Enzyme-Based Logic Systems for Information Processing. *Chem. Soc. Rev.*, **2010**, *39*, 1835-1857.

33. Katz, E. Biocomputing-Tools, Aims, Perspectives. *Curr. Opin. Biotechnol.*, **2015**, *34*, 202 - 208.

34. Wu, C. C.; Wan, S.; Hou, W. J.; Zhang, L. Q.; Xu, J. H.; Cui, C.; Wang, Y. Y.; Hu, J.; Tan, W. H. A Survey of Advancements in Nucleic Acid-Based Logic Gates and Computing for Applications in Biotechnology and Biomedicine. *Chem. Commun.*, **2015**, *51*, 3723-3734.

35. Orback, R.; Willner, B.; Willner, I. Catalytic Nucleic Acids (DNAzymes) as Functional Units for Logic Gates and Computing Circuits: From Basic Principles to Practical Applications. *Chem. Commun.*, **2015**, 51, 4144 -4160.

36. Zabock, A.; Ley, K. Hold on to your Endothelium: Postarrest Steps of the Leucocyte Adhesion Cascade. *Immunity,* **2006**, 25, 185-187.

37. Pu, F.; Ren, J.; Qu, X. Recent Advances in the Construction of Nanozyme-Based Logic Gates. *Biophys. Rep.* **2020**, 6, 245-255.

38. Cao, Z.; Wang, G. Multi-Stimuli-Responsive Polymer Materials: Particles, Films, and Bulk Gels. *Chem. Rec.*, **2016**, *16*, 1398-1435.

39. Yadav, S.; Kumar, A. K.; Kumar, P. Nanoscale Self-Assembly for Therapeutic Delivery. *Front. Bioeng. Biotechnol,* **2020,** *8,* 1-24.

40. Steed, J.W.; Atwood, J.L. Supramolecular Chemistry; Wiley: Chichester, UK, 2000.

41. Lehn, J.-M. Supramolecular Chemistry – Concepts and Perspectives; VCH: Weinheim, Germany, 1995; Chapter 9.

42. Blum, A. P.; Kammeyer, J. K.; Rush, A. M.; Callmann, C. E.; Hahn, M. E.; Gianneschi, N. C. Stimuli-Responsive Nanomaterial for Biomedical Applications. *J. Am. Chem. Soc.* **2015**, *137*, 2140.

43. Ebnesajjad, S. Polymerization Surfactants. In Fluoroplastics, Second Edition, Vol. 1 William Andrew Publishing, 2015, pp 76-94.

44. Aizenberg, J.; Weaver, J. C.; Thanawala, M. S.; Sundar, V. C.; Morse, D. E.; Skeleton of Euplectella sp.: Structural Hierarchy from the Nanoscale to the Macroscale. *Science*, **2005**, *309,* 275-278.

45. Gao, J.; Zhuang, J.; Wang, F.; Raghupathi, K. R.; Thayumanavan, S. Protein AND Enzyme Gated Supramolecular Disassembly. *J. Am. Chem. Soc.,* **2014***, 136,* 2220-2223.

46. Brown, P.; Butts, C. P.; Eastoe, J. Stimuli-Responsive Surfactants. *Soft Matter* **2013**, *9*, 2365−2374.

47. Tehranibagha, A.; Holmberg, K. Cleavable Surfactants. *Curr. Opin. Colloid Interface Sci*. **2007**, *12*, 81−91.

48. Wang, Y.; Xu, H.; Zhang, X. Tuning the Amphiphilicity of Building Blocks: Controlled Self-Assembly and Disassembly for Functional Supramolecular Materials. *Adv. Mater.* **2009**, *21*, 2849− 2864.

49. Tang, J.; Quinlan, P. J.; Tam, K. C. Stimuli-Responsive Pickering Emulsions: Recent Advances and Potential Applications. *Soft Matter*, **2015**, *11*, 3512−3529.

50. Zhuang, J.; Zhao, B.; Meng, X.; Schiffman, J. D.; Perry, S. L.; Vachet, R. W.; Thayumanavan, S. A Programmable Chemical Switch Based on Triggerable Michael Acceptors. *Chem. Sci.* **2020**, *11*, 2103− 2111.

CHAPTER 2

PROGRAMMABLE EMULSIONS VIA NUCLEOPHILE-INDUCED COVALENT SURFACTANT MODIFICATIONS

Adapted from

Fernandez, A.; Zentner, C. A.; Shivrayan, M.; Samson, E.; Savagatrup, S.; Zhuang, J.; Swager, T. M. Thayumanavan, S. Programmable Emulsions via Nucleophile-Induced Covalent Surfactant Modifications. *Chem. Mater.* **2020**, *32*, 4663-4671.

2.1 INTRODUCTION

Responsive supramolecular assemblies have attained much attention due to their ability to be used in a range of applications such as drug delivery carriers, diagnostic purposes. Platforms for sensing/detection, tissue engineering, packaging, coatings, and textiles.[1] Among the most promising methods to create responsive assemblies is the use of tailored amphiphilic constituents to control the self-assembly process in the presence of various stimuli. For example, simple changes to pH, temperature, or ionic strength can impact the overall strength of surfactants without changes to their structure.[2-5] A lot more control can be obtained in self-assembly platforms by utilizing well-known chemical transformations, where dramatic changes in surfactant structure can be used to dictate their propensity to self-assemble. Specifically, with respect to surfactant-based platforms, switchable or cleavable surfactants can be developed to formulate responsive assemblies with both reversible and irreversible control.[6–9] Such responsive amphiphiles, and the molecular assemblies they form, are useful in many applications including oil recovery, drug delivery, biodegradation, and sensing. Various small molecule platforms, polymers, and Pickering particles, and have been designed to fulfill these applications.[6-16] More sophisticated approaches have also utilized external stimuli, such as with light, CO_2, enzymes, heat-induced retro-Diels−Alder, and dynamic covalent chemistry, to trigger changes to surfactant structure.[10-23]

Although chemical reactions have been utilized for structural changes in surfactant molecules, tunable kinetic control over these reactions and the effect of such control over nano-assembly transformations have been less studied. In one study, the inverse has been demonstrated, where self-assembly is used to impart kinetic control of the hydrolysis of cleavable ester surfactants of varying alkyl chain lengths.[24] In general, however, responsive surfactant-based assemblies are in either the initial state or the final state before and after reaction providing an “on/off” signal.

Conversely, by controlling the rate and extent of reaction, an assembly system under kinetic control can provide varying responses to subtle changes in the environment, adding system versatility beyond an on/off signal. In this work, we were interested in designing sophisticated single and double emulsion systems with kinetic control of surfactant cleavage in response to small molecule or molecular assembly triggers. For this purpose, new surfactant molecules that can be programmed to undergo covalent modification by nucleophiles were developed. Specifically, triggerable Michael acceptor (TMAc) functionalities were used as components of head groups in the surfactant molecules that assemble at and stabilize the interface of emulsions. Within our group, the kinetic control of TMAc small molecule analogues has been demonstrated.[25] Expanding on this TMAc small molecule platform, TMAc surfactants were developed with varying surfactant head groups, and formulated as a programmable emulsion-based platform. The hypothesis is as follows: nucleophile-induced modification of the TMAc surfactant will alter its ability to stabilize the emulsion interface, leading to macroscopic changes in the emulsion systems. Although previous studies by our group and others have demonstrated surfactant and emulsion responses to nucleophiles, this work provides investigations into kinetic control of the emulsions through surfactant reactivity. To establish this premise, specific small molecule nucleophiles and nano-assemblies with nucleophile functionality were utilized to demonstrate their effect on stability and morphology of single and double emulsions, respectively. Furthermore, the tunable reactivity of the surfactants on the microscale can be observed through macroscopic outputs of the emulsion systems, demonstrating the use of reaction kinetics to affect the extent of emulsion response. Additionally, these assemblies can be rendered responsive to an unrelated cue by coupling these processes to a nano- assembly that exhibits responsive molecular release features. Collectively,

this work demonstrates highly controlled and programmable emulsion systems via nucleophile-induced covalent modifications.

2.2 EXPERIMENTAL

2.2.1 MATERIALS

All reagents were obtained from commercial sources and used as received without further purification. Sodium hydroxide (NaOH) was purchased from Macron. Tetrahydrofuran (THF) was purchased from Acros Organics. Thiourea was purchased from Alfa Aesar. Zonyl FS-300 (40 wt % solution, Zonyl), cetyltrimethylammonium bromide (CTAB), sodium dodecyl sulfate (SDS), 2-(2- methoxyethoxy)ethanol, p-toluenesulfonyl chloride, concentrated HCl, hexamethylenediamine (HMDA), dodecyl acrylate, 1,4- diazabicyclo[2.2.2]octane, phosphorous tribromide, triethylamine, pyridine, xylene di-isocyanate, 1,1,1-tris(hydroxymethyl)ethane, 4- cyano-4-(phenylcarbonothioylthio)pentanoic acid N-succinimidyl ester, octyl methacrylate, azodiisobutyronitrile (AIBN), 1,4-dioxane, trifluoroacetic acid (TFA), and acetyl chloride were purchased from Sigma-Aldrich. FC-770 was purchased from Synquest. Formaldehyde, methylene chloride, sodium sulfate, hexanes, ethyl acetate, diethyl ether, 4-dimethylaminopyridine, Invitrogen Attofluor Cell chamber, and 3500 MWCO dialysis tubing were purchased from ThermoFisher Scientific. t-Boc-NH-PEG-amine (MW 5000) was purchased from Laysan Bio. Poly(dimethylsiloxane) (PDMS) Sylgard 184 elastomer kit was purchased from Dow Corning. Milli-Q water from a Barnstead Nanopure Water System (ThermoFisher Scientific) was used for the preparation of the emulsions.

2.2.2 INSTRUMENTAL ANALYSIS

^{1}H and ^{13}C NMR spectra for 2-(2- methoxyethoxy)ethanethiol (EG_2-SH) were recorded on a Bruker Avance DRX 600 spectrometer. The chemical shift data are reported in units of δ (ppm) relative to the residual solvent. ^{1}H and ^{13}C NMR spectra of surfactants, polymers, and kinetic studies were recorded on a Bruker DPX-400 MHz or 500 MHz NMR spectrometer and all spectra calibrated against trimethylsilyl (TMS) standard. Mass spectrometric data were acquired using electron spray ionization (ESI) on a Q-ToF-micro quadruple mass spectrometer (Micro mass). Molecular weights of the polymers were measured using gel permeation chromatography (GPC, Waters) with PMMA as standard fitted with a refractive index detector and THF as eluent with a flow rate of 1 mL/min. Tip sonication for particle preparation was performed with a Q125 Sonica probe sonicator. Dynamic light scattering (DLS) measurements were performed on a Malvern Nanozetasizer-ZS operating at 633 nm. Fluorescence measurements were performed using a PerkinElmer LS 55 spectrometer. All optical images reported were taken on an AmScope B120C-E1 equipped with an AmScope MU1003 camera or collected using NIS-Elements AR software on a Nikon TiE inverted microscope fitted with an Andor Zyla sCMOS camera. Samples were treated with UV irradiation (Black Ray UV lamp, 365 nm, 115 V to 60 Hz) or an LED Engin LZ1-00UV00 365 nm LED with a fixed current 700 mA driver (Digikey). Monodisperse double emulsions were prepared using a Dolomite Microfluidic device equipped with two Mitos P-Pumps (Basic), an external Remote Chamber (30 mL), and Telos High Throughput Droplet System.

2.2.3 SYNTHETIC PROTOCOLS

a. Synthesis of reactive surfactants

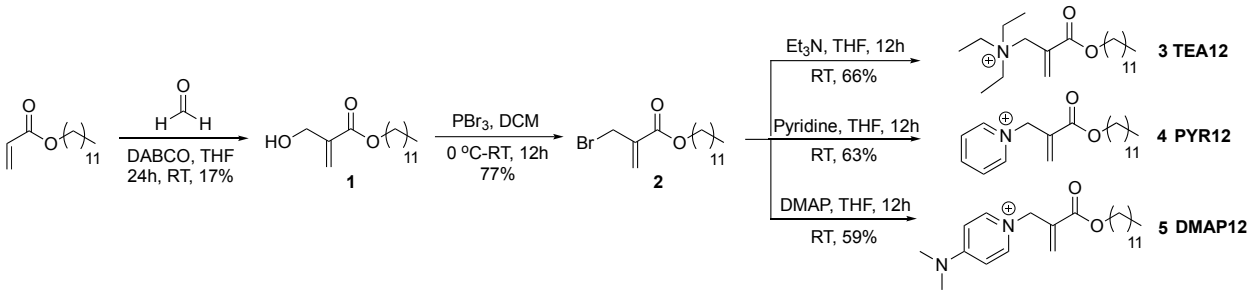

SCHEME 2.1**:** Synthesis of precursors and surfactants (**1** –**5**).

Synthesis of 1: A modified synthetic procedure was followed for the synthesis of **1** and **2**, from a published work on similar esters.[26] 40 g (0.166 mol) of n-dodecyl acrylate was added to a round bottom flask and dissolved in 120 mL tetrahydrofuran under inert atmosphere. To this, 9.3 g (0.083 mol) 1,4-diazabicyclo [2.2.2] octane (DABCO) was added dropwise, and the reaction mixture stirred for 10 minutes. 2.5 g (0.083 mol) formaldehyde was then added dropwise to the reaction mixture and stirred overnight. It was then concentrated under reduced pressure, partitioned with methylene chloride and water, then extracted with methylene chloride. The combined extracts were dried over anhydrous Na_2SO_4, and the crude product purified by silica gel chromatography using hexane and ethyl acetate as eluents to afford **1** in 17% yield. ^{1}H NMR ($CDCl_3$, 400 MHz, TMS): δ (ppm) = 6.22 (s, 1H), 5.81 (s, 1H), 4.28-4.30 (d, 2H), 4.12-4.15 (t, 2H), 2.78 (broad s, 1H), 1.61-1.68 (m, 2H), 1.23-1.30 (m, 18H), 0.83-0.86 (t, 3H). ^{13}C NMR (125 MHz, $CDCl_3$): δ (ppm) = 166.7, 139.8, 125.7, 65.3, 62.6, 32.2, 29.9, 29.9, 29.8, 29.8, 29.6, 29.5, 28.8, 26.2, 23.0, 14.4. $[M+Na]^+$ from ESI spectroscopy: 293.20879.

Synthesis of 2: 7.5 g (0.027 mol) of **1** was added to a round bottom flask and dissolved in 50 mL methylene chloride under inert atmosphere. To this, phosphorous tribromide (PBr_3) (7.48g, 0.027 mol) was added dropwise at 0 ^oC and the reaction mixture stirred overnight. It was then concentrated under reduced pressure, partitioned with methylene chloride and water, then extracted with methylene chloride. The combined extracts were dried over anhydrous Na_2SO_4 and the crude product was purified by silica gel chromatography using hexane and ethyl acetate as eluents to afford **2** in 77% yield. ^1H NMR ($CDCl_3$, 400 MHz, TMS): δ (ppm) = 6.31 (s, 1H), 5.93 (s, 1H), 4.15-4.21 (m, 4H), 3.71-3.77 (m, 1H), 1.64-1.70 (m, 2H), 1.25-1.32 (m, 18H), 0.85-0.88 (t, 3H). ^{13}C NMR (125 MHz, $CDCl_3$): δ (ppm) = 169.6, 164.9, 137.6, 129.0, 65.9, 65.5, 48.7, 31.9, 30.7, 29.7, 29.6, 29.5, 29.5, 29.4, 29.3, 28.5, 26.0, 22.7, 14.2. $[M+Na]^+$ from ESI spectroscopy: 355.12525.

Synthesis of 3 (TEA12): 1.5 g (0.0045 mol) of **2** was dissolved in 5 mL tetrahydrofuran in a round bottom flask. To this, 0.5 g (0.0049 mol) triethylamine was added dropwise, and the solution stirred overnight. The reaction mixture was concentrated under reduced pressure and precipitated in diethyl ether 6 times to afford **3** in 66 % yield. ^1H NMR (D_2O, 400 MHz, TMS): δ (ppm) = 6.87 (s, 1H), 6.56 (s, 1H), 4.22-4.25 (m, 4H), 3.30-3.36 (m, 6H), 1.72-1.75 (m, 2H), 1.30-1.39 (m, 27H), 0.88-0.92 (t, 3H). ^{13}C NMR (125 MHz, D_2O): δ (ppm) = 166.5, 140.3, 128.9, 66.2, 55.6, 53.3, 31.9, 29.8, 29.7, 29.6, 29.4, 29.3, 28.2, 25.8, 22.6, 13.9, 7.4. $[M]^+$ from ESI spectroscopy: 354.33692.

Synthesis of 4 (PYR12): 1 g (0.003 mol) of **2** was dissolved in 4 mL tetrahydrofuran in a round bottom flask. To this, 0.26 g (0.0033 mol) pyridine was added dropwise and stirred overnight. The

reaction mixture was concentrated under reduced pressure and precipitated in diethyl ether 6 times to afford **4** in 63 % yield. ^{1}H NMR (D_2O, 400 MHz, TMS): δ (ppm) = 9.06-9.07 (d, 2H), 8.64-8.68 (t, 1H), 8.16-8.19 (t, 2H), 6.64 (s, 1H), 6.57 (s, 1H), 5.60 (s, 1H), 4.07-4.10 (t, 2H), 1.57-1.59 (m, 2H), 1.17-1.21 (m, 19H), 0.75-0.79 (t, 3H). ^{13}C NMR (125 MHz, D_2O): δ (ppm) = 165.2, 147.0, 146.6, 145.4, 144.9, 135.1, 133.1, 128.6, 128.4, 67.0, 65.7, 61.4, 58.9, 46.6, 31.9, 31.7, 29.7, 29.6, 29.4, 29.3, 29.1, 28.3, 25.8, 22.5, 13.8. $[M]^+$ from ESI spectroscopy: 375.30068.

Synthesis of 5 (DMAP12): 0.5 g (0.0015 mol) of **2** was added to a round bottom flask and dissolved in 3 mL tetrahydrofuran. To this, 0.2 g (0.0016 mol) 4-dimethylaminopyridine was added dropwise and the reaction mixture stirred overnight. It was then concentrated under reduced pressure and precipitated in diethyl ether 6 times to afford **5** in 59 % yield. ^{1}H NMR (D_2O, 400 MHz, TMS): δ (ppm) = 8.16-8.17 (d, 2H), 6.95-6.97 (d, 2H), 6.48 (s, 1H), 6.37 (s, 1H), 5.05 (s, 1H), 4.06-4.10 (t, 2H), 3.21 (s, 1H), 1.60 (s, 2H), 1.19-1.22 (m, 18H), 0.78-0.81 (t, 3H). ^{13}C NMR (125 MHz, D_2O): δ (ppm) = 165.5, 156.4, 141.9, 134.2, 133.1, 107.6, 65.4, 57.5, 39.8, 31.9, 29.7, 29.7, 29.6, 29.3, 28.3, 25.8, 22.5, 13.8. $[M]^+$ from ESI spectroscopy: 332.25832.

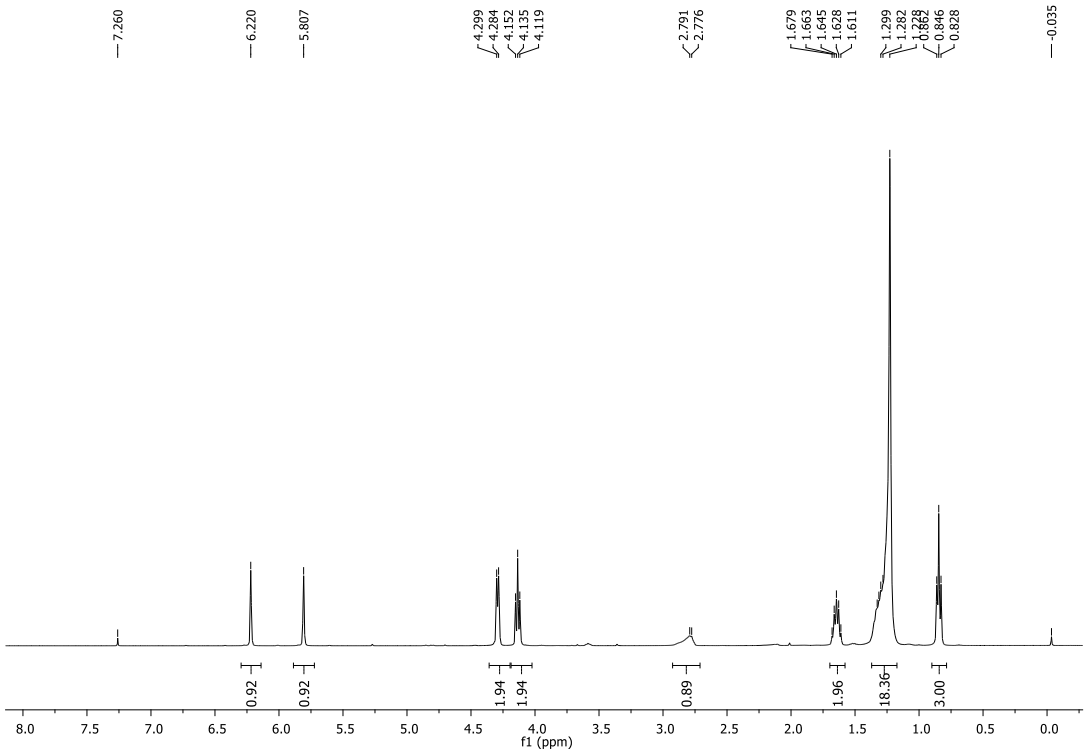

FIGURE 2.1: ^{1}H-NMR spectrum of precursor 1.

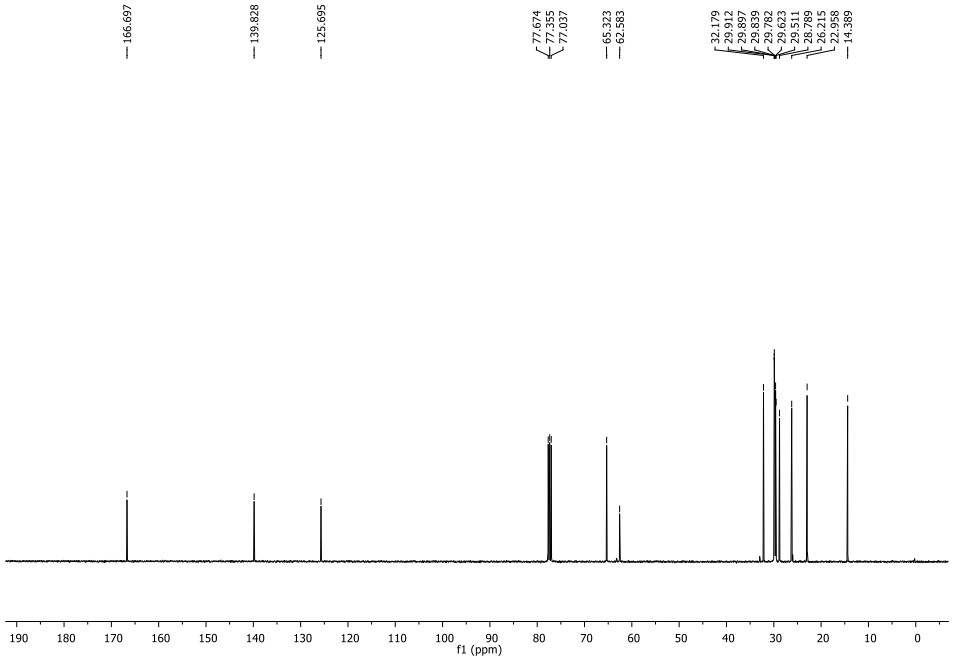

FIGURE 2.2: ^{13}C-NMR spectrum of precursor 1.

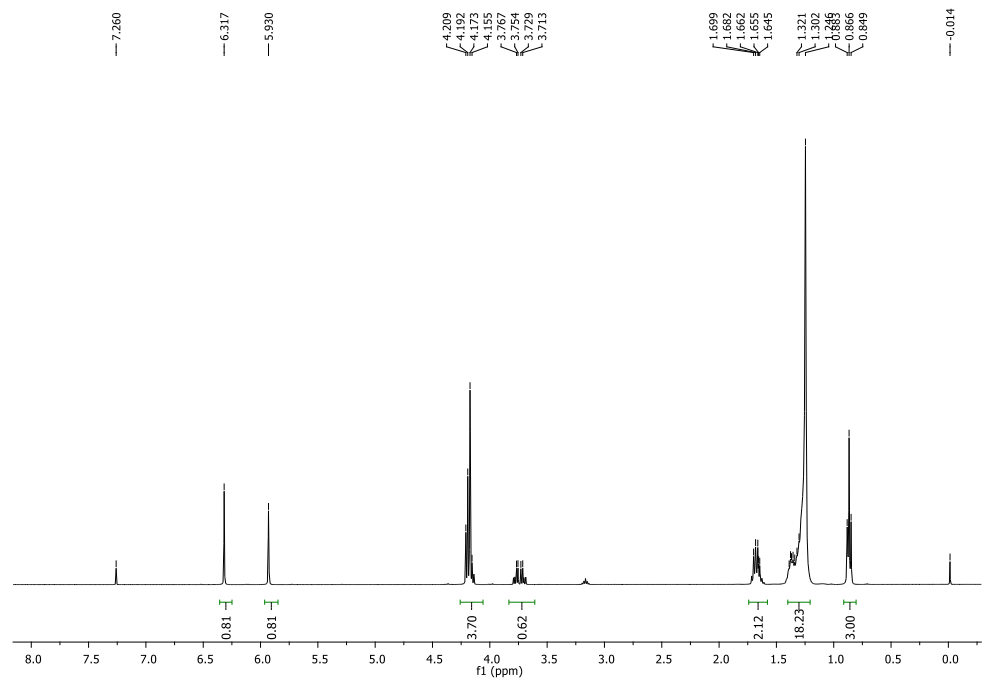

FIGURE 2.3: ^{1}H-NMR spectrum of precursor 2.

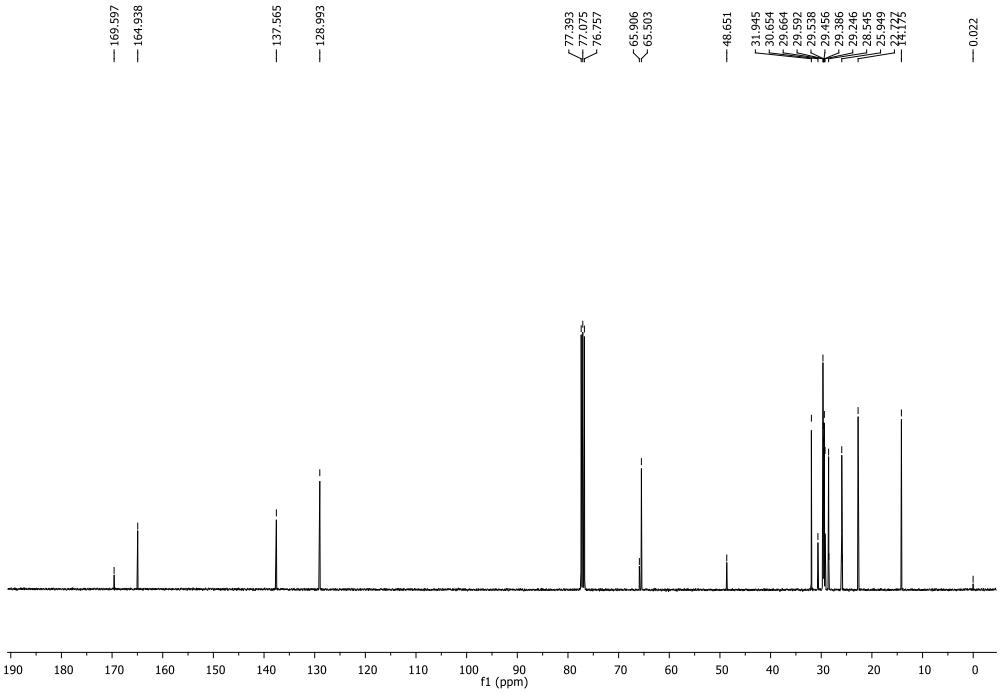

FIGURE 2.4: ^{13}C-NMR spectrum of precursor 2.

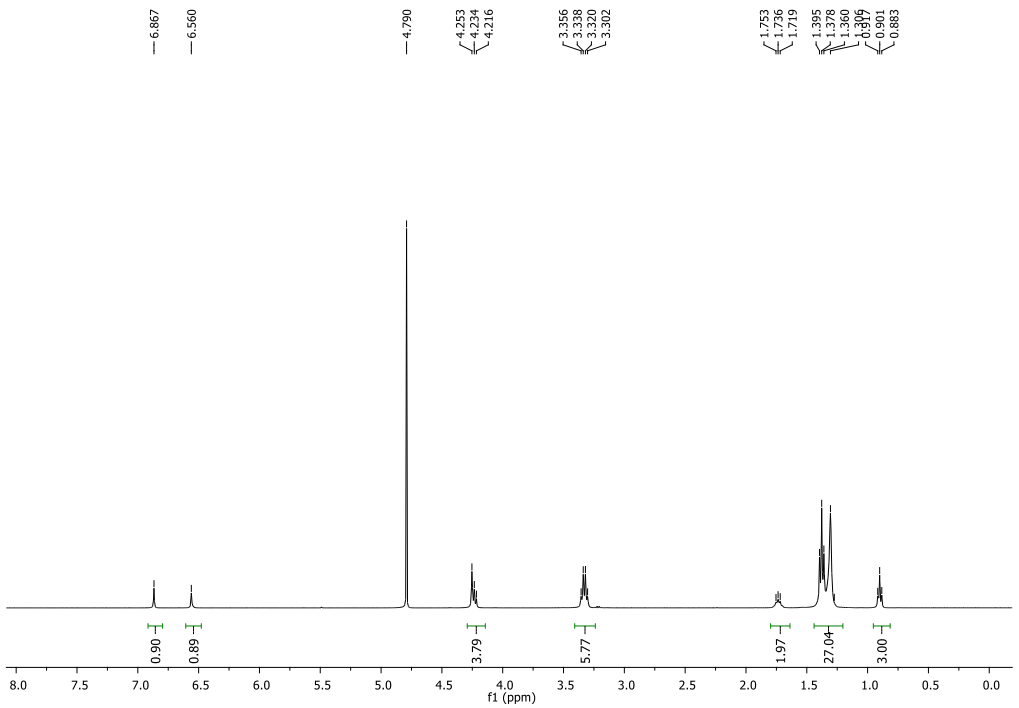

FIGURE 2.5: ^{1}H-NMR spectrum of surfactant 3 (TEA12).

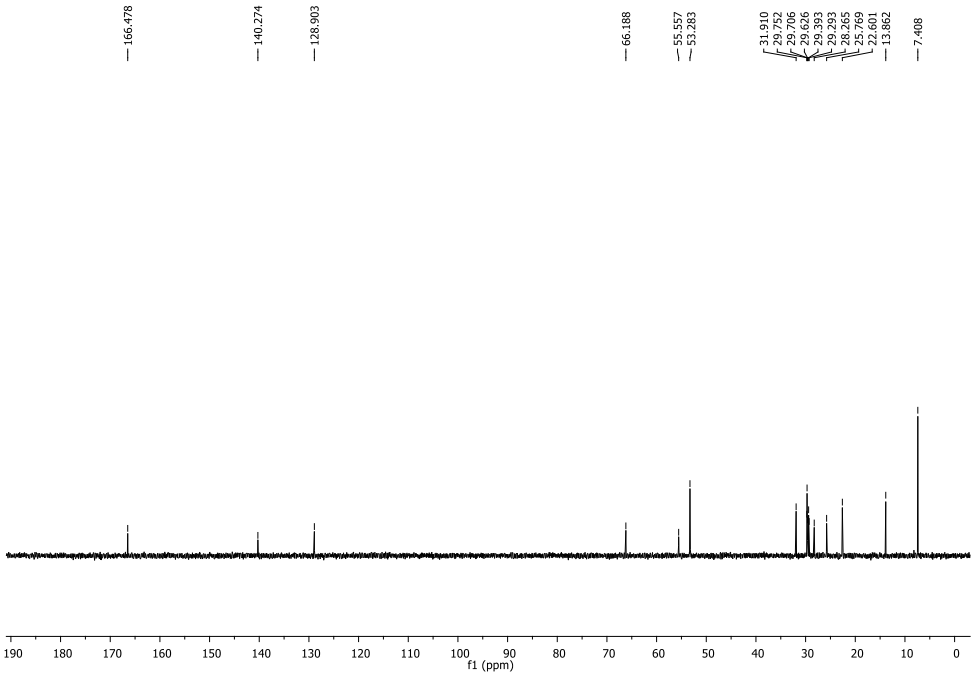

FIGURE 2.6: ^{13}C-NMR spectrum of surfactant 3 (TEA12)

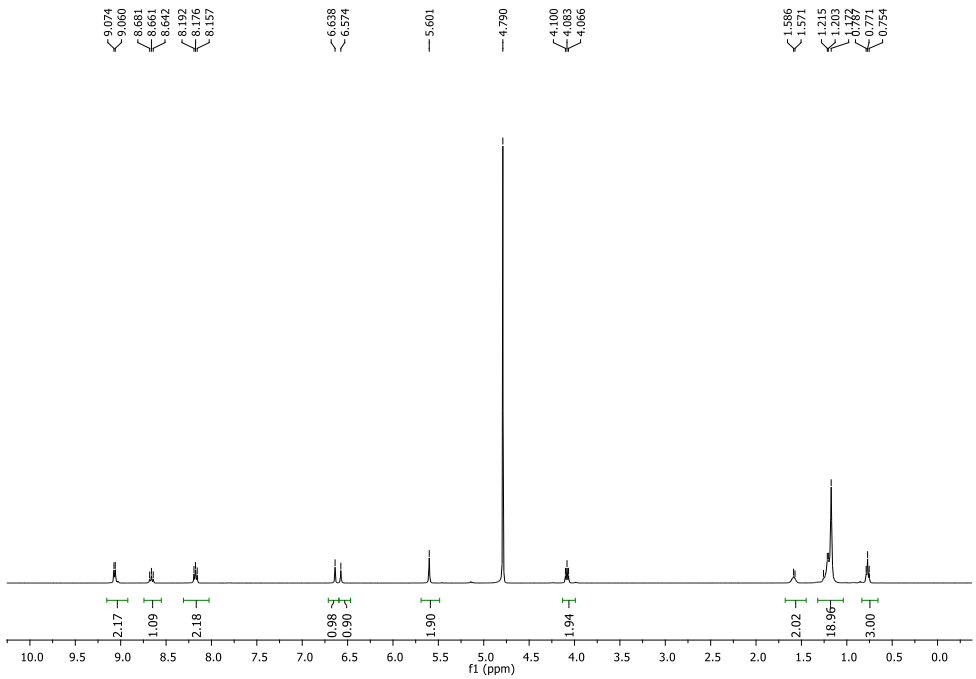

FIGURE 2.7: ^{1}H-NMR spectrum of surfactant 4 (PYR12)

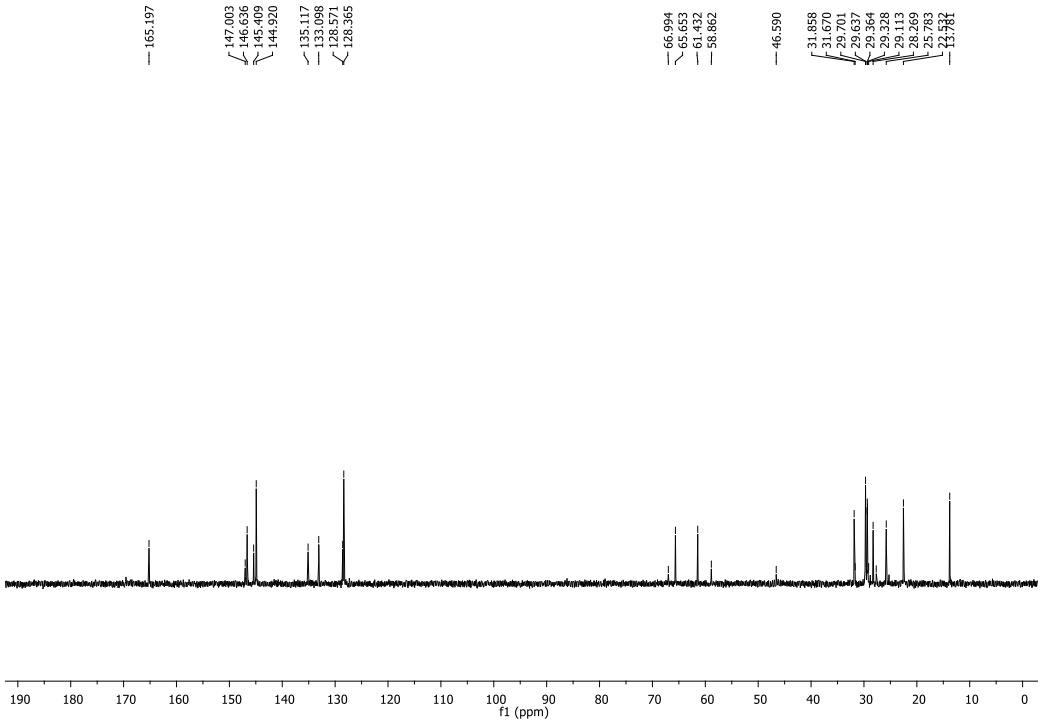

FIGURE 2.8: ^{13}C-NMR spectrum of surfactant 4 (PYR12).

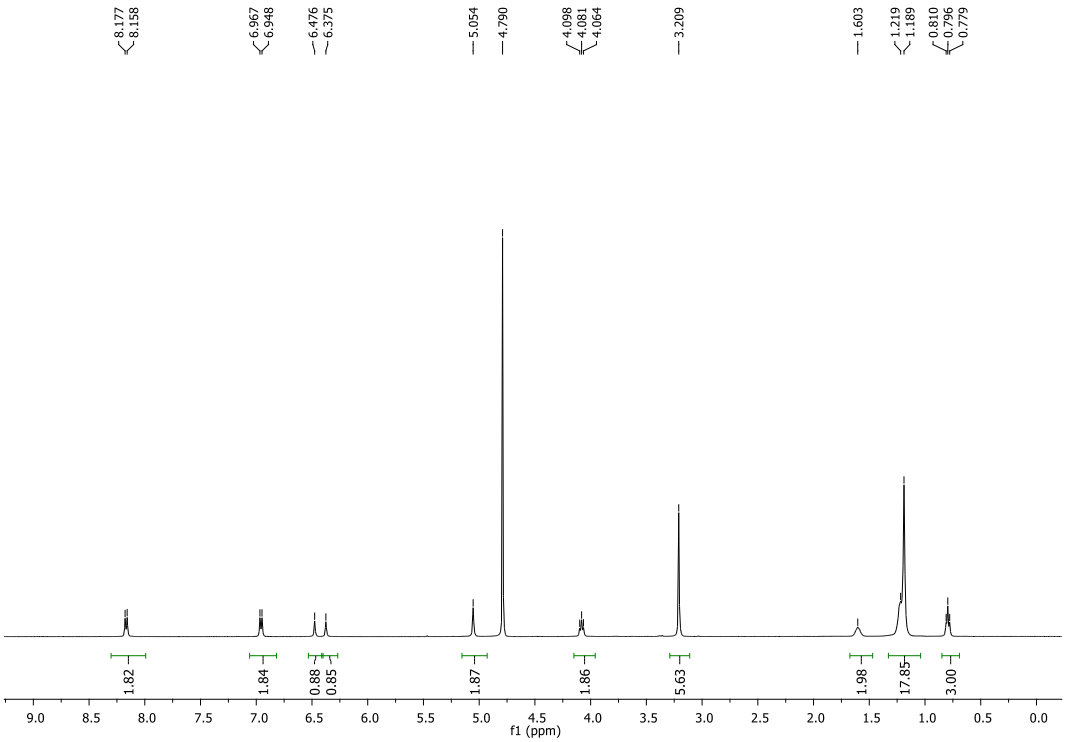

FIGURE 2.9: ^{1}H-NMR spectrum of surfactant 5 (DMAP12).

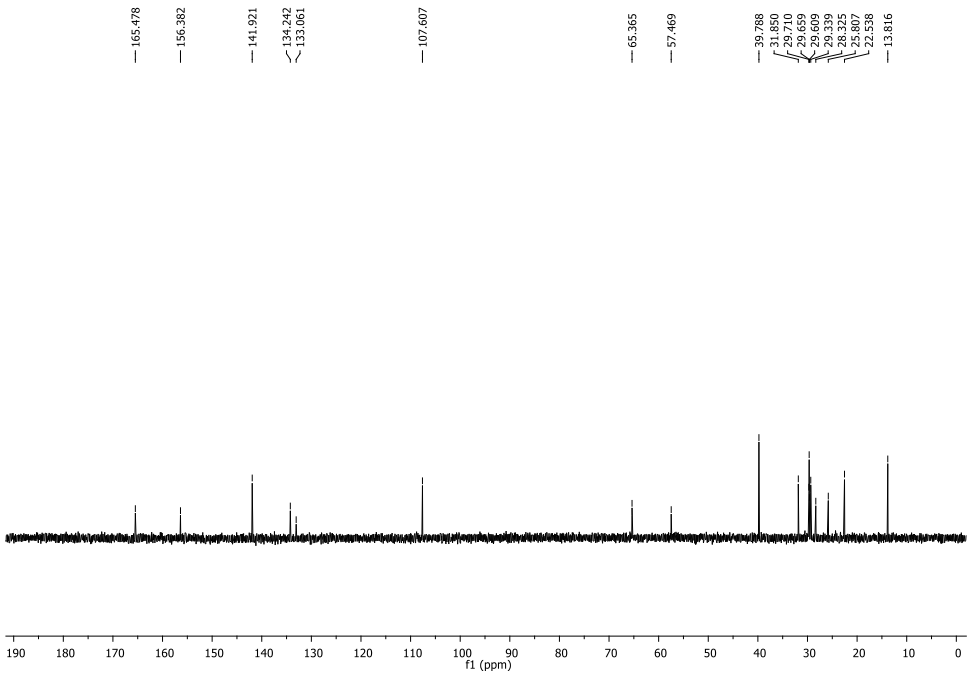

FIGURE 2.10: ^{13}C-NMR spectrum of surfactant 5 (DMAP12).

b. Synthesis of Amine-P2 and Acetamide-P2

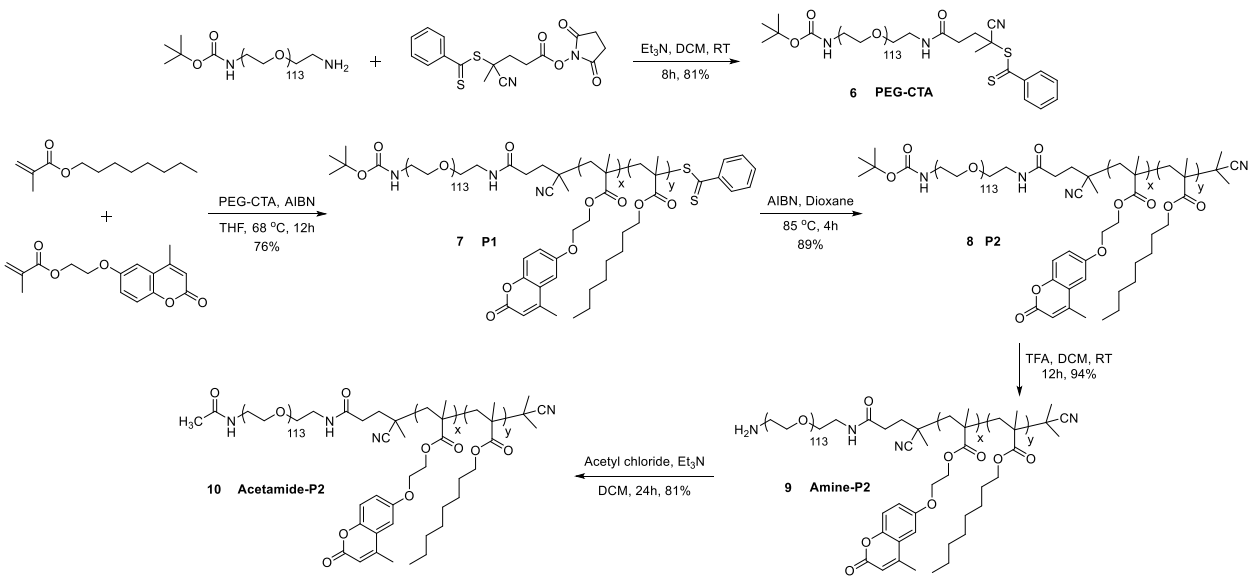

SCHEME 2.2: Synthesis of amphiphilic polymers **Amine-P2** (**9**) and **Acetamide-P2** (**10**).

Synthesis of 6 (PEG-CTA): 500 mg (0.001 mol) of t-BOC-NH-PEG-Amine, MW 5000 was added to a round bottom flask and dissolved in 10 mL anhydrous tetrahydrofuran under inert atmosphere. To this, triethylamine (101.19 mg, 0.01 mol) was added dropwise and the solution stirred for 15 minutes. Further, 4-Cyano-4-(phenylcarbonothioylthio)pentanoic acid N-succinimidyl ester (376.45 mg, 0.01 mol) was dissolved in 3 mL methylene chloride and added dropwise to the solution and stirred for 8 h. The reaction mixture was concentrated under reduced pressure and dialyzed using 3500 MWCO dialysis tubing against methylene chloride and methanol at a 1:1 volume ratio for 24 h. After dialysis, the solution was concentrated under reduced pressure to afford **6** in 81 % yield. ^{1}H NMR ($CDCl_3$, 400 MHz, TMS): δ (ppm) = 7.88-7.92 (m, 2H), 7.53-7.57 (m, 1H), 7.36-7.40 (m, 2H), 6.54 (s, 1H), 5.05 (s, 1H), 3.79-3.80 (m, 5H), 3.51-3.63 (m, 478 H), 3.44-3.46 (m, 7H), 3.29-3.20 (m, 3H), 2.84 (s, 1H), 2.52-2.63 (m, 3H), 2.42-2.45 (m, 1H), 1.93 (s, 3H), 1.43 (s, 9H). ^{13}C NMR (125 MHz, $CDCl_3$): δ (ppm) = 170.4, 156.0, 144.6, 133.0, 128.6,

126.7, 118.7, 107.4, 79.2, 70.6, 70.3, 69.9, 59.1, 46.1, 40.4, 39.5, 34.2, 31.6, 29.7, 28.4, 25.6, 24.2. GPC (THF): Mn = 8,813 g mol^{-1}, PDI = 1.02.

Synthesis of 7 (P1): To a Schlenk-flask, octyl methacrylate (753.54 mg, 3.797 mmol), coumarin methacrylate (27.4 mg, 0.095 mmol), recrystallized azodiisobutyronitrile (AIBN) (0.32 mg, 0.0019 mmol), and PEG-CTA **6** (50 mg, 0.0095 mmol) were dissolved in 1.6 mL anhydrous tetrahydrofuran. The reaction mixture was subjected to three freeze-pump-thaw cycles. The sealed flask was immersed in a pre-heated oil bath at 78 °C and stirred for 12 h. The polymerization was quenched by cooling the flask in chilled water. The reaction mixture was concentrated under reduced pressure and dialyzed using 3500 MWCO dialysis tubing against methylene chloride and methanol at a 1:1 volume ratio for 48 h. After dialysis, the polymer solution was concentrated under reduced pressure to afford **7** in 76 % yield. ^{1}H NMR ($CDCl_3$, 400 MHz, TMS): δ (ppm) = 7.84-7.86 (m, 2H), 7.52-7.54 (m, 11H), 6.93-6.96 (m, 8H), 6.80-6.82 (m, 7H), 6.15 (s, 8H), 4.22-4.32 (d, 50H), 3.91 (broad s, 691H), 3.64 (s, 478 H), 2.41 (s, 31H), 1.79-1.89 (m, 656H), 1.61-1.64 (m, 837H), 1.29-1.44 (m, 3579H), 1.02 (s, 402H), 0.88-0.89 (m, 1640H). ^{13}C NMR (125 MHz, $CDCl_3$): δ (ppm) = 178.2, 177.8, 177.5, 176.8, 161.4, 161.0, 155.3, 152.4, 125.7, 114.0, 112.8, 112.2, 101.1, 70.6, 65.0, 54.2, 45.1, 44.8, 31.9, 29.7, 29.3, 29.2, 28.4, 28.3, 28.1, 26.1, 22.7, 18.7, 18.4, 16.5, 14.1. GPC (THF): Mn = 47848 g mol^{-1}, PDI = 1.21. DSC: T_m = 42.41°C, T_c = -34.35 °C. TGA: Onset of degradation temperature (5% weight loss) = 265.06 °C, Peak degradation temperature = 384.09 °C.

Synthesis of 8 (P2): 500 mg (0.01 mmol) of **7** and AIBN (16.42 mg, 0.1 mmol) were added to a round bottom flask and dissolved in 10 mL 1,4-dioxane under inert atmosphere. This reaction

mixture was refluxed at 85 ^{o}C for 4 h. Further, it was concentrated under reduced pressure and dialyzed using 3500 MWCO dialysis tubing against methylene chloride and methanol at a 1:1 volume ratio for 48 h. After dialysis, the solution was concentrated under reduced pressure to afford **8** in 89 % yield. ^{1}H NMR ($CDCl_3$, 400 MHz, TMS): δ (ppm) = 7.52-7.54 (m, 10H), 6.91-7 (m, 8H), 6.80-6.82 (m, 7H), 6.15 (s, 8H), 4.22-4.32 (d, 63H), 3.91 (broad s, 701H), 3.64 (s, 478 H), 2.41 (s, 38H), 1.89-2.03 (m, 355H), 1.79 (s, 405H), 1.60-1.64 (m, 967H), 1.29-1.43 (m, 4135H), 1.01 (s, 487H), 0.88-0.89 (m, 1799H). ^{13}C NMR (125 MHz, $CDCl_3$): δ (ppm) = 177.8, 177.5, 176.7, 161.4, 161.0, 155.3, 152.4, 125.7, 113.9, 112.3, 101.2, 70.6, 65.0, 54.2, 45.8, 45.1, 44.8, 31.9, 29.7, 29.3, 29.2, 29.2, 28.3, 28.2, 26.1, 22.7, 18.7, 18.4, 16.5, 14.1. GPC (THF): Mn = 54,246 g mol^{-1}, PDI = 1.17.

Synthesis of 9 (AMINE-P2): 80 mg (0.01 mmol) of **8** was dissolved in 4 mL methylene chloride under inert atmosphere in a round bottom flask. To the reaction mixture, trifluoroacetic acid (1.82 mg, 0.1 mmol) was added dropwise and stirred overnight. It was then concentrated under reduced pressure and dialyzed using 3500 MWCO dialysis tubing against methylene chloride and methanol at a 1:1 volume ratio for 24 h. After dialysis, the solution was concentrated under reduced pressure to afford **9** in 94 % yield. ^{1}H NMR ($CDCl_3$, 400 MHz, TMS): δ (ppm) = 7.78-7.83 (m, 1H), 7.52-7.61 (m, 10H), 6.91-7 (m, 7H), 6.75-6.82 (m, 6H), 6.15 (s, 5H), 4.22-4.32 (d, 63H), 3.91 (broad s, 705H), 3.64 (s, 478 H), 2.41 (s, 38H), 1.89-2.03 (m, 365H), 1.79 (s, 367H), 1.70 (s, 261H), 1.60 (s, 927H), 1.24-1.29 (m, 4172H), 1.01 (s, 506H), 0.88-0.89 (m, 1755H). ^{13}C NMR (125 MHz, $CDCl_3$): δ (ppm) = 177.8, 177.5, 176.8, 161.3, 161.0, 155.3, 152.4, 113.9, 112.3, 101.0, 70.6, 65.0, 54.2, 45.8, 45.1, 44.8, 31.9, 29.7, 29.3, 29.2, 29.2, 28.3, 28.2, 26.1, 22.7, 18.7, 18.4, 16.5, 14.1. GPC (THF): Mn = 53,798 g mol^{-1}, PDI = 1.34.

Synthesis of 10 (Acetamine-P2): 100 mg (0.01 mmol) of **9** was dissolved in a round bottom flask and dissolved in 5 mL methylene chloride under inert atmosphere. To the reaction mixture, acetyl chloride (1.57 mg, 0.1 mmol) was added dropwise and stirred overnight. Afterwards, it was concentrated under reduced pressure and dialyzed using 3500 MWCO dialysis tubing against methylene chloride and methanol at a 1:1 volume ratio for 48 h. After dialysis, the solution was concentrated under reduced pressure to afford **10** in 81 % yield. ^{1}H NMR ($CDCl_3$, 400 MHz, TMS): δ (ppm) = 7.52-7.55 (m, 11H), 6.94-7 (m, 9H), 6.76-6.83 (m, 8H), 6.15 (s, 6H), 4.22-4.32 (d, 47H), 3.92 (broad s, 705H), 3.64 (s, 478 H), 2.41 (s, 31H), 1.89-2.08 (m, 282H), 1.90 (s, 397H), 1.60 (s, 1194H), 1.30 (m, 4142H), 1.02 (s, 432H), 0.88-0.90 (m, 1891H). ^{13}C NMR (125 MHz, $CDCl_3$): δ (ppm) = 177.8, 177.5, 176.8, 160.9, 154.9, 152.4, 137.8, 118.7, 115.7, 113.8, 101.3, 70.6, 65.0, 54.7, 54.5, 54.2, 45.2, 44.8, 40.2, 31.9, 29.7, 29.3, 29.2, 28.3, 28.2, 26.1, 22.7, 18.3, 16.5, 14.1. GPC (THF): Mn = 52,607 g mol^{-1}, PDI = 1.28.

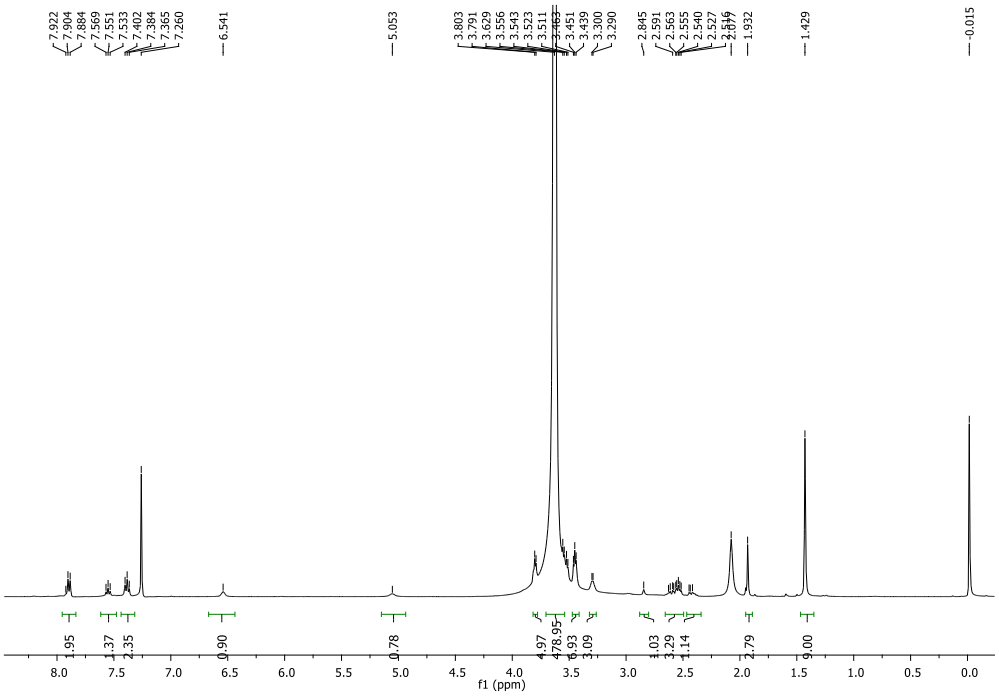

FIGURE 2.11: ^{1}H-NMR spectrum of **6.**

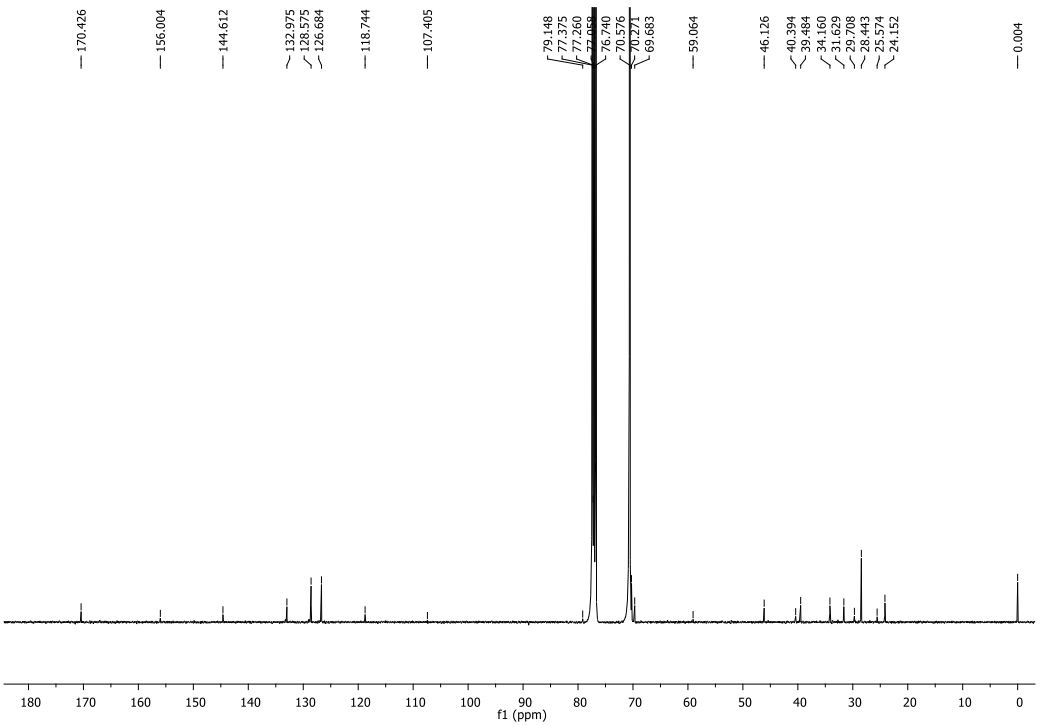

FIGURE 2.12: ^{13}C-NMR spectrum of **6.**

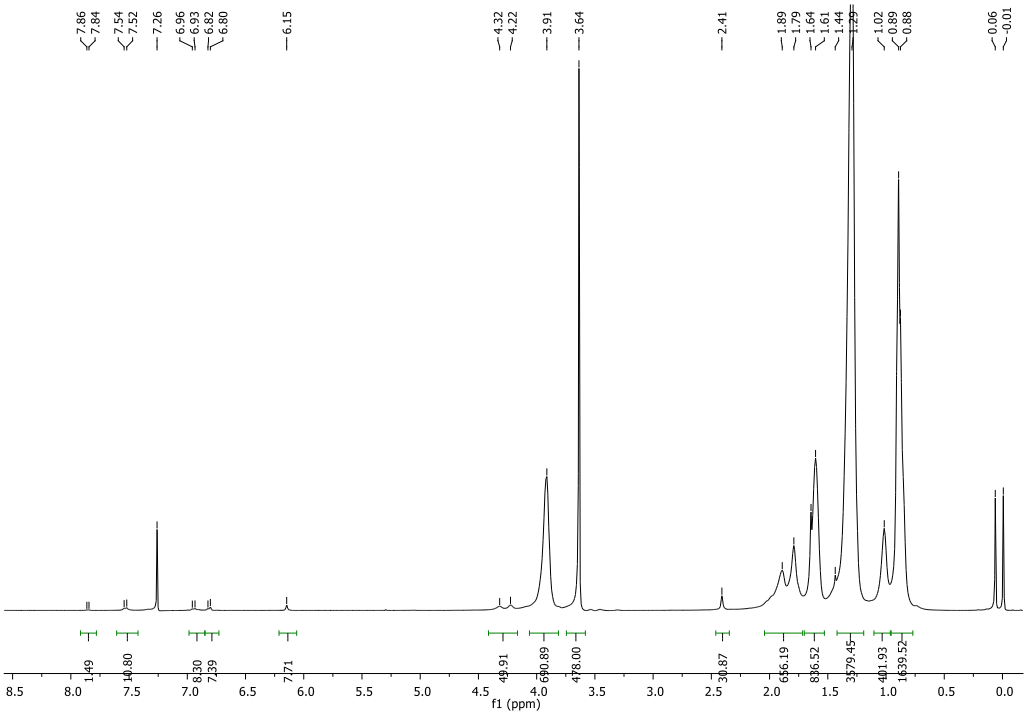

FIGURE 2.13: ^{1}H-NMR spectrum of **7 (P1).**

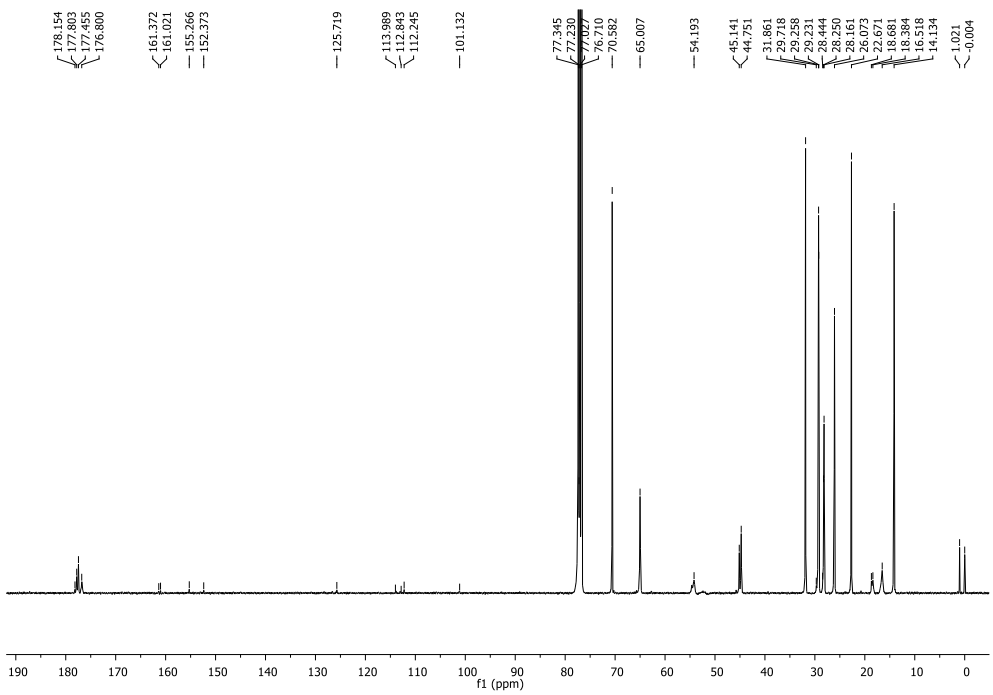

FIGURE 2.14: ^{13}C-NMR spectrum of **7 (P1).**

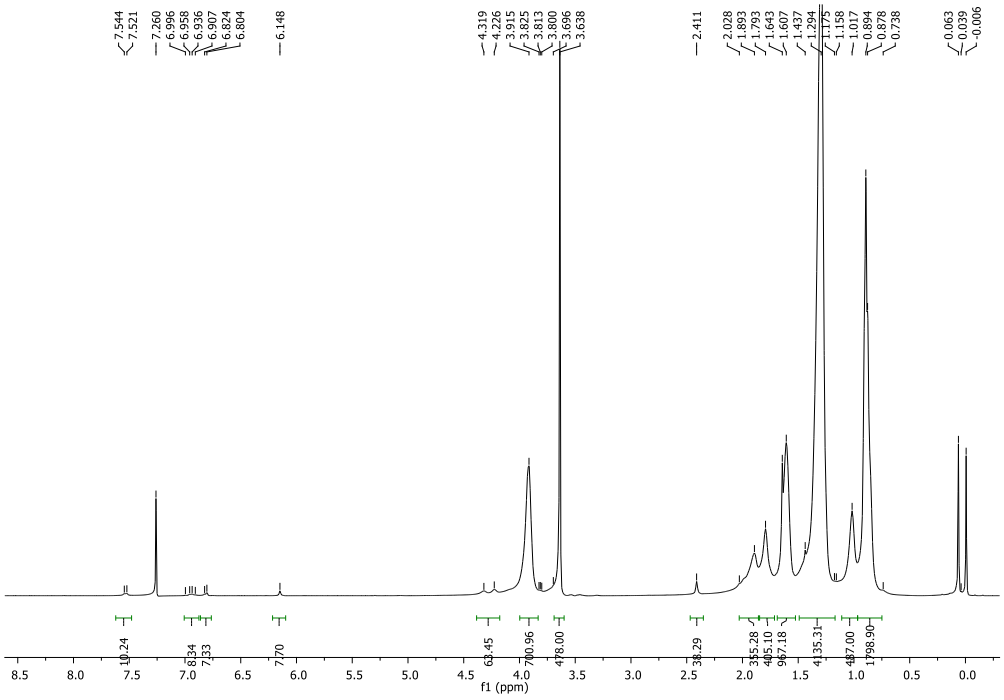

FIGURE 2.15: ^{1}H-NMR spectrum of **8 (P2).**

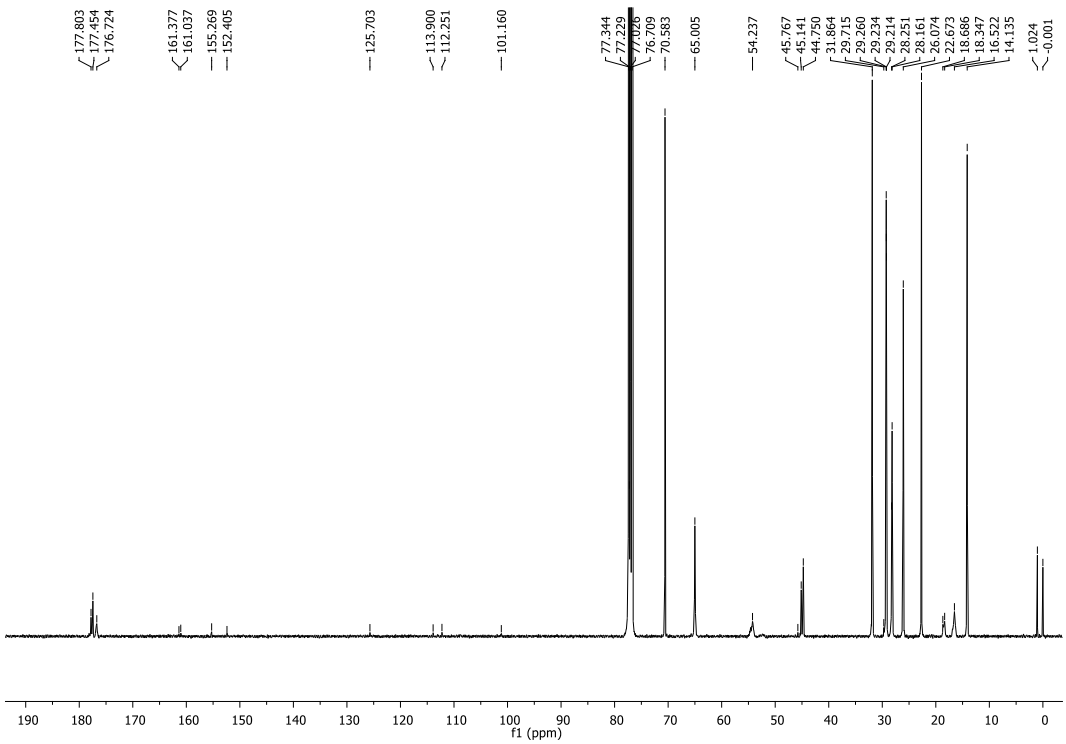

FIGURE 2.16: ^{13}C-NMR spectrum of **8 (P2).**

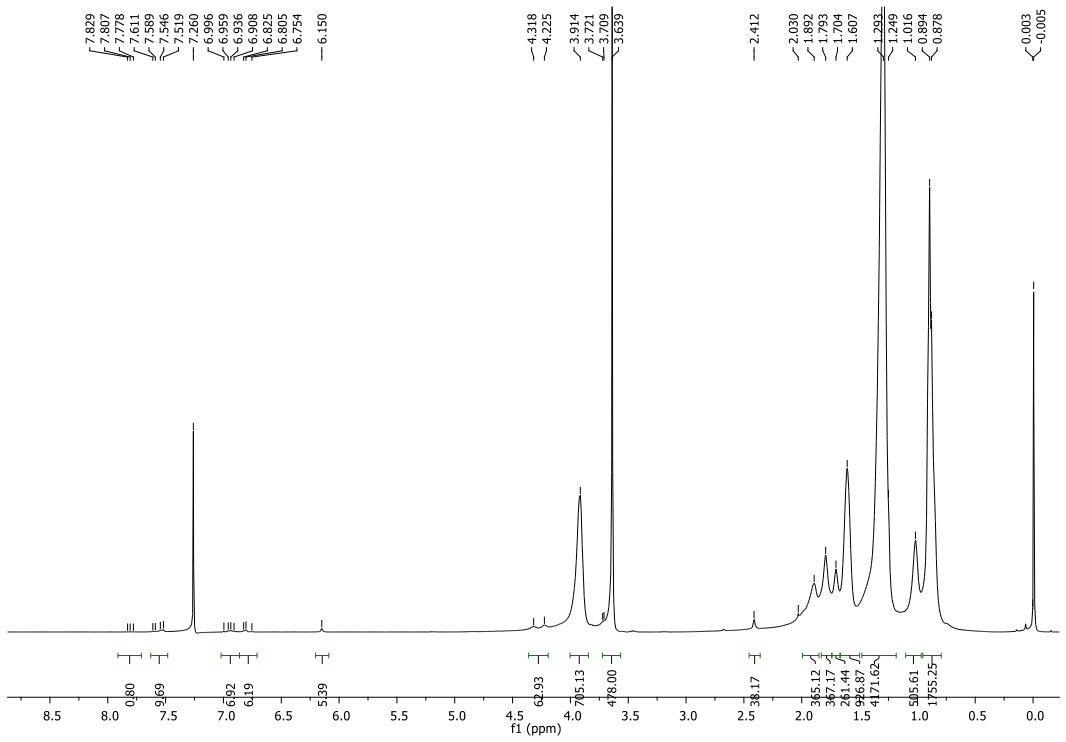

FIGURE 2.17: ^{1}H-NMR spectrum of **9 (Amine-P2).**

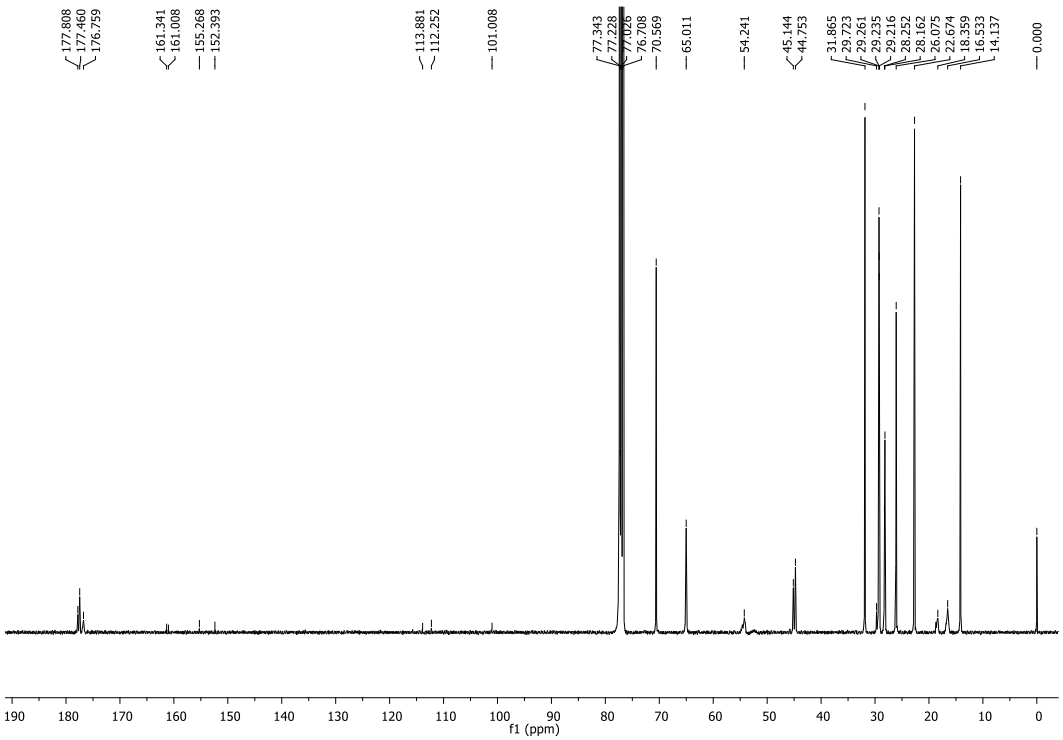

FIGURE 2.18: ^{13}C-NMR spectrum of **9** (**Amine-P2).**

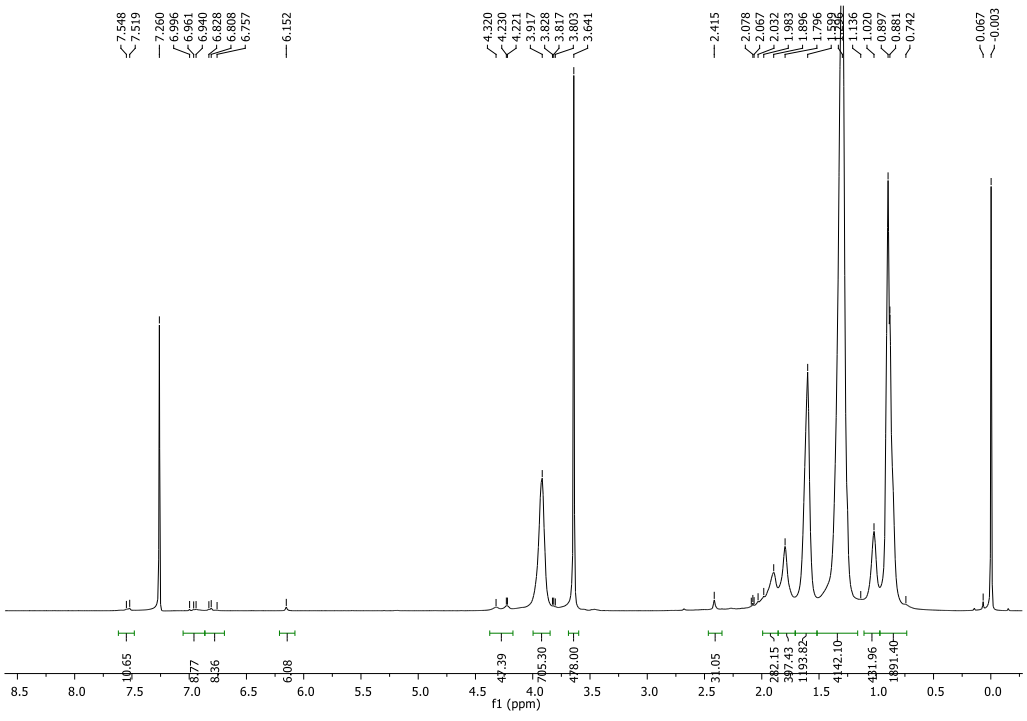

FIGURE 2.19: ^{1}H-NMR spectrum of **10 (Acetamide-P2).**

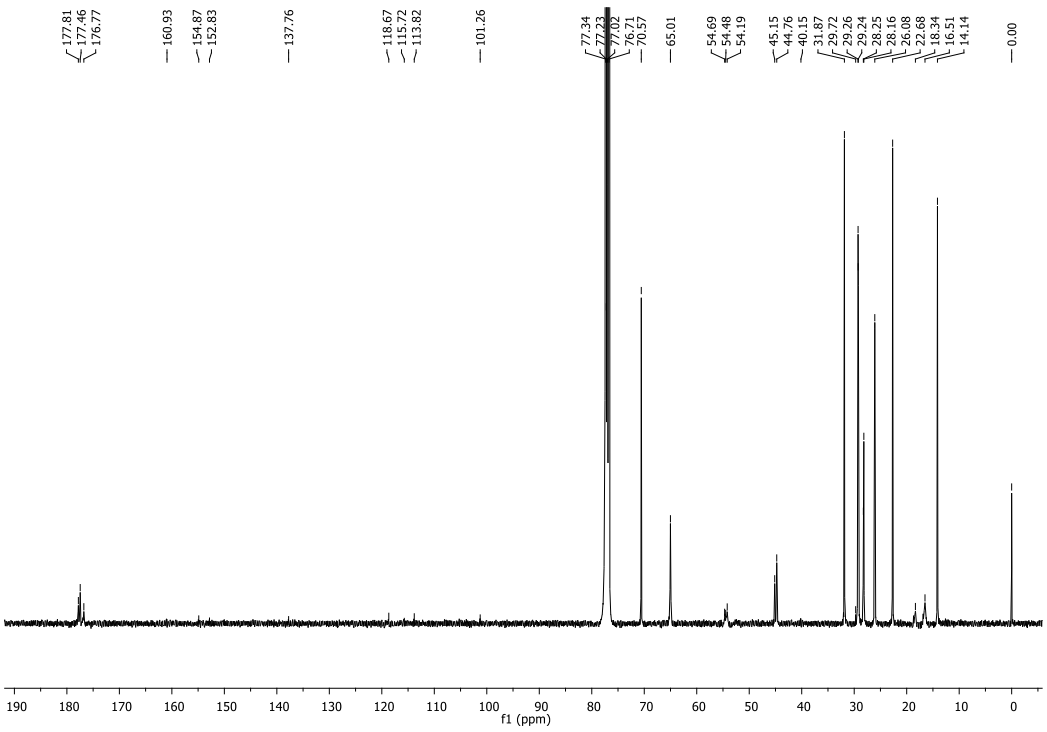

FIGURE 2.20: ^{13}C-NMR spectrum of **10 (Acetamide-P2).**

c. Synthesis of 2-(2-methoxyethoxy)ethanethiol (EG_2-SH)

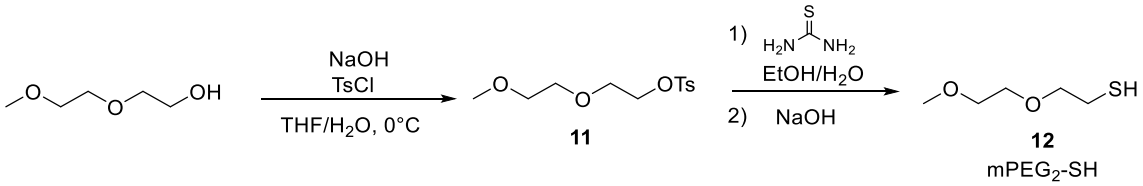

SCHEME 2.3: Synthesis of thiol trigger EG_2-SH

Synthesis of 11: The synthesis of 11 and 12 was performed according to a modified literature procedure.[27] Solutions of 2-(2-methoxyethoxy)ethanol (4.81 g, 40.0 mmol, 10 mL tetrahydrofuran) and sodium hydroxide (2.31 g, 57.8 mmol, 1.4 equiv., 12 mL water) were added to an argon purged flask and cooled in an ice bath. A solution of p-toluenesulfonyl chloride (7.29 g, 38.2 mmol, 1 equiv., 10 mL tetrahydrofuran) was added dropwise over the course of 10 min, while keeping the reaction mixture near 3 ºC. The reaction was stirred in an ice bath for 4 h. The

reaction mixture was then extracted with diethyl ether (20 mL) and the aqueous phase then extracted further with diethyl ether (3 x 10 mL). The combined organic phase was washed with water until the water wash reached neutral pH. The organic phase was then dried with sodium sulfate, reduced under pressure (without heating), and yielded **11** as a clear oil (8.07 g, 274.33 g/mol, 29.4 mmol, 74%). The intermediate used in the next step without further purification.

Synthesis of 12 (2-(2-methoxyethoxy)ethanethiol)): 11 (6.00 g, 21.9 mmol), thiourea (1.69 g, 22.2 mmol, 1 equiv.), 12 mL anhydrous ethanol, and 1 mL water were added to a flask and purged with argon. The reaction mixture was stirred under reflux for 3 h. A solution of sodium hydroxide (1.28 g, 32.0 mmol, 1.5 equiv. 5 mL water) was then added and the reaction mixture was refluxed for an additional 4 h. The reacti on mixture was concentrated under pressure to 2 mL, diluted with 10 mL of water, and neutralized with 1 M HCl. The aqueous phase was extracted with methylene chloride (3 x 50 mL), dried over sodium sulfate, and reduced under pressure. The crude was purified with column chromatography (25% ethyl acetate, 75% hexanes, $R_f = 0.35$) and reduced under pressure, giving the title compound as a clear oil (0.86 g, 136.21 g/mol, 6.3 mmol, 29%). The ^{1}H and ^{13}C-NMR spectra are in line with literature reports.^{1}H-NMR (600 MHz, $CDCl_3$): δ (ppm) = 1.57 (t, 1H), 2.70 (q, 2H), 3.38 (s, 3H), 3.54 (m, 2H), 3.62 (m, 4H). ^{13}C-NMR (150 MHz, $CDCl_3$): δ (ppm) = 24.3, 59.2, 70.3, 72.0, 73.1.

2.2.4 METHODS

a. Formulation of Amine-P2 nucleophilic assemblies:

Amine-P2 and acetamide-P2 assemblies were prepared by dissolving 0.4 mg of the respective P2 polymers in 200 μL of methylene chloride. One mL of water was added to the

solution and sonicated for 1 min using a probe sonicator and stirred overnight to obtain the amine-P2 and acetamide- P2 self-assemblies of ~150 nm.

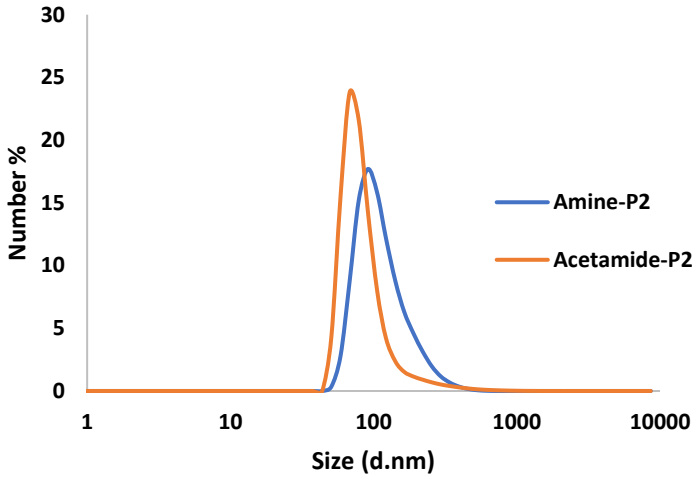

Figure 2.21: DLS plots of Amine-P2 and Acetamide-P2 assemblies

b. Polymer CAC studies:

Critical Aggregation Concentration (CAC) values of amine-P2 and acetamide-P2 were also determined using the encapsulation of Nile red. To 4 mg of either amine-P2 or acetamide-P2, 400 µL acetone was added and sonicated for 5 min. Following this, 2 mL of deionized water was added dropwise to prepare polymer solutions of 2 mg/mL. A solution of 100 µL of 1 mg/mL Nile red in acetone was then added to the aqueous solutions, stirred overnight, and the solutions filtered across a nylon syringe filter with a pore size of 0.45 µm to remove unencapsulated dye. Fluorescence measurements of the polymer assemblies with encapsulated dye were then performed at various concentrations to calculate their respective CAC.

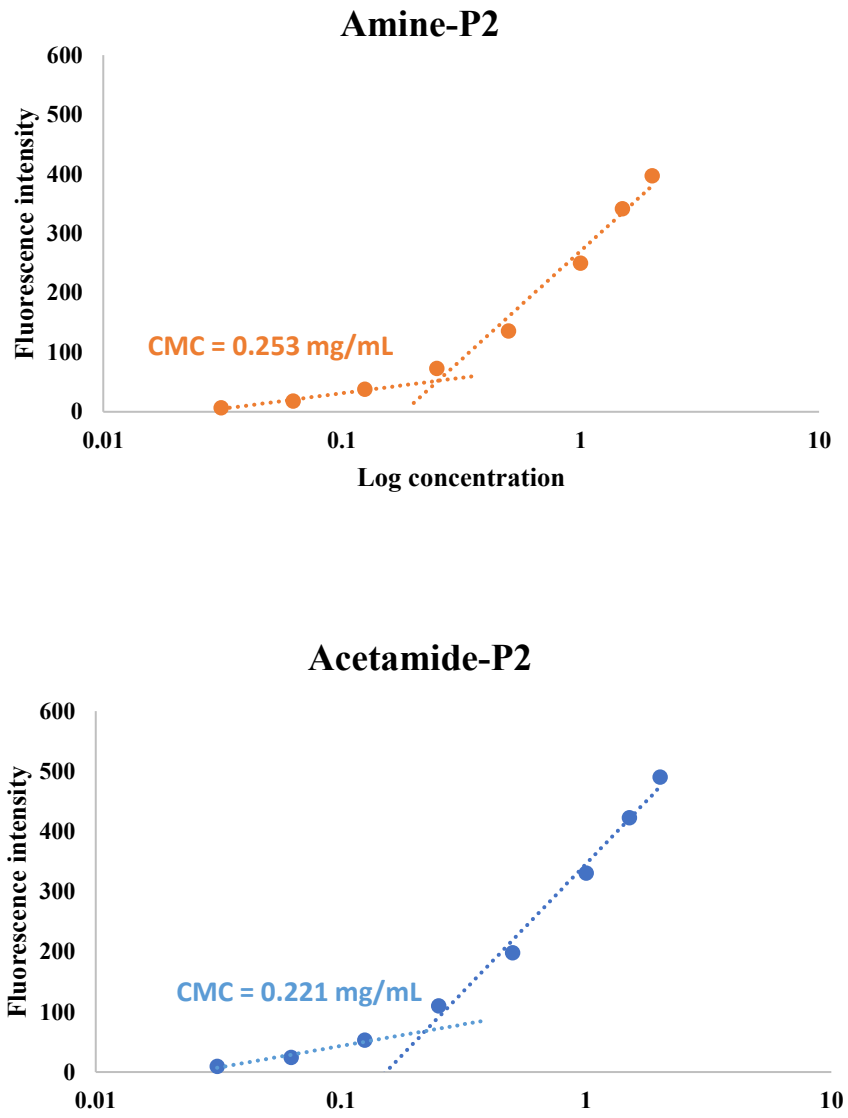

FIGURE 2.22: CAC plots of Amine-P2 and Acetamide-P2 assemblies

c. Formulation of nucleophile releasing polymersomes:

HMDA encapsulated in PEG-Azo-PLA polymerosomes (PAP-HMDA) was prepared following the literature procedure[28] by adding 100 µL of 2 mg/mL HMDA to a 1 mg/mL solution of PAP polymer (Mn = 18 000 g/mol) in water (20 wt % HMDA to PAP) and stirred overnight.

The solution was dialyzed against water for 24 h using a 3k MWCO membrane. The PAP-HMDA solution was then concentrated to 4 mg/mL using 3k MWCO spin filters. DLS results indicate that the size of PAP vesicles before and after the addition of HMDA is ~200 nm.

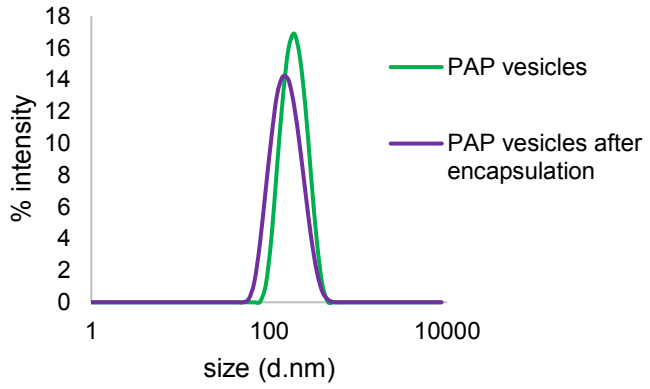

FIGURE 2.23: DLS plot of PAP vesicles before and after encapsulation

d. Qualitative determination of interfacial tension:

We first attempted pendant drop studies on hexane dispersed in surfactant solutions to determine interfacial tensions. However, the hexane drops were not stable during the measurement and unreliable, quantitative measurements of interfacial tension were not possible. We, therefore, used a qualitative study to determine what concentrations of each surfactant were necessary to achieve the same interfacial tension at the HC/W interface, using morphology estimations. The desired surfactant concentrations were determined to get uniform interfacial tension at the HC/W interface using TEA12, PYR12, or DMAP12. To this end, polydisperse double emulsions were fabricated via the outlined polydisperse procedure at a constant Zonyl concentration (0.2 wt%) with varying concentrations of reactive HC-surfactants to achieve the perfect Janus morphology. At 0.2 wt% Zonyl, the following concentrations of surfactants were used to achieve perfect Janus morphology: 5 mM TEA12, 4 mM PYR12, and 4 mM DMAP12 (Figure S32). At these

concentrations, the surfactants achieve the same HC/Water interfacial tensions. For all double emulsion studies, 5 mM TEA12, 4 mM PYR12, or 4 mM DMAP12 with 0.2 wt% Zonyl were used for the continuous phase. For all single emulsion studies, 5 mM TEA12, 4 mM PYR12, or 4 mM DMAP12 were used for the continuous phase.

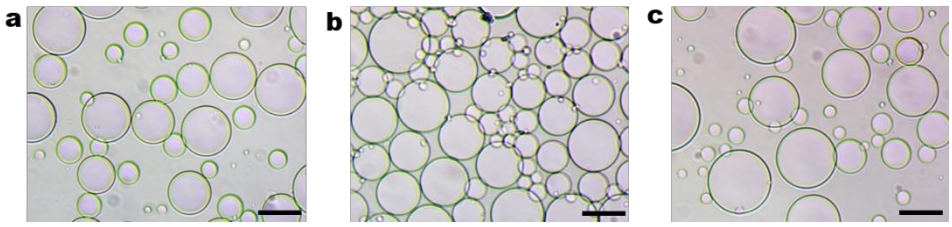

FIGURE 2.24: Perfect Janus morphology for each reactive HC-surfactant with 0.2 wt% Zonyl and a) 5 mM TEA12, b) 4 mM PYR12, or c) 4 mM DMAP12. Scale bar = 50 μm.

e. CMC studies of surfactants:

CMC studies were also performed by first preparing 4 mL of either TEA12, DMAP12, or PYR12 in deionized water at a concentration of 2 mg/mL. Following this, 100 μL of 1 mg/mL Nile red in acetone was added to the aqueous solutions and stirred overnight. The solutions were then filtered across a nylon syringe filter with a pore size of 0.45 μm to remove the unencapsulated dye. Fluorescence measurements of the surfactant solutions with encapsulated dye were then performed at various concentrations to calculate the respective surfactant CMC values.

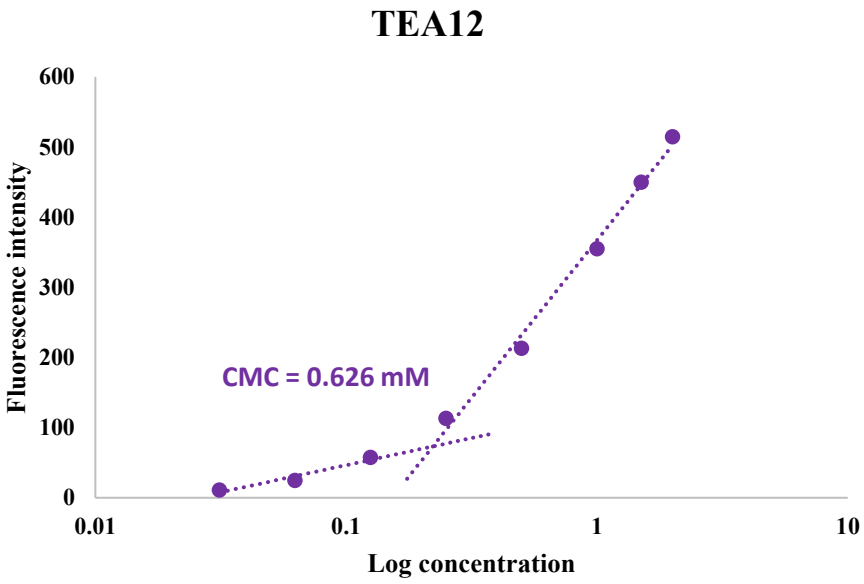

FIGURE 2.25: CMC plot of TEA12

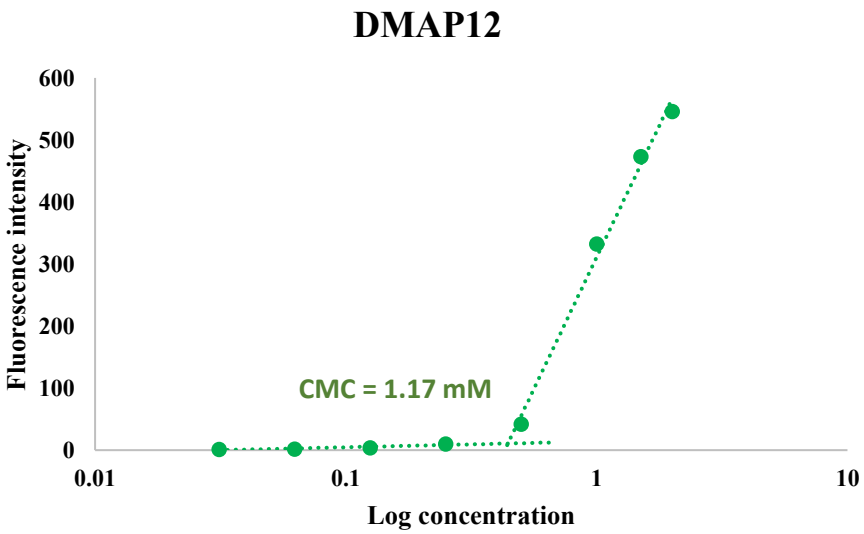

FIGURE 2.26: CMC plot of DMAP12

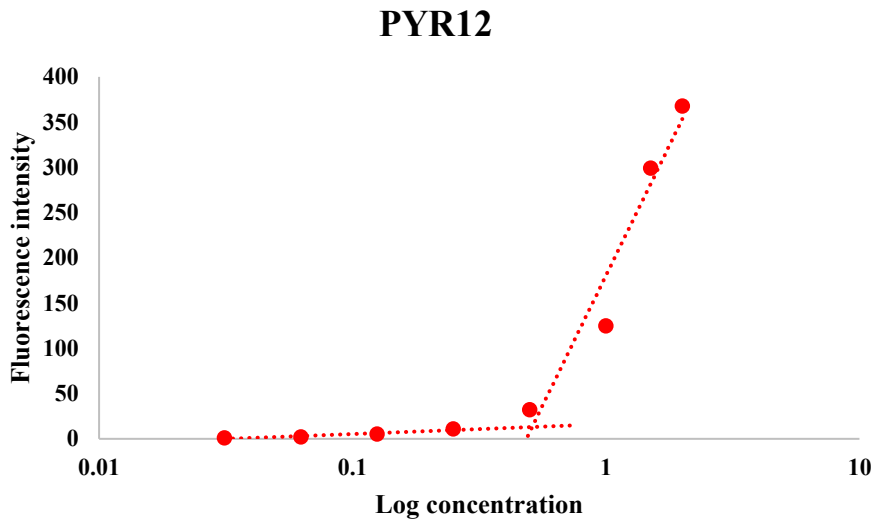

FIGURE 2.27: CMC plots of PYR12

f. Preparation of single emulsions:

Single emulsions were prepared by hand-shaking hexane- and surfactant-containing aqueous solution (neutral pH) at a 1:4 volume ratio for 10 s.

g. Preparation of double emulsions:

Polydisperse double emulsions were fabricated according to a published literature procedure.[17] Hexane and FC-770 in a 1:1 volume ratio were heated above their upper critical temperature (Tc) to form a homogeneous mixture. A mixture of 25 µL of the heated hexane/FC-770 was added to 500 µL of the surfactant-containing aqueous continuous phase (neutral pH) and vortexed for 5 s for emulsification. Double emulsions were imaged upon cooling and full phase separation of the hexane/FC-770 mixture. Monodisperse double emulsions were fabricated on a Dolomite Microfluidic device with a 50 µm chip. The emulsion system consisted of an aqueous solution of 1 wt % SDS as the continuous phase (neutral pH) and a 1:1 volume ratio of hexanes and FC-770 (heated above their Tc) as the droplet phase. Pressures were controlled at 200 mbar for the

continuous phase and 100 mbar for the dispersed phase during droplet formation through the chip. After double emulsion formation, the continuous phase was exchanged for the desired surfactant system. Monodispersity was retained with solvent exchange.

h. Testing Setups and General Procedures:

PDMS microfluidic device fabrication procedure was modified from a published protocol.[29] Briefly, the microchannels were constructed by casting a mixture of 10:1 base/crosslinker onto a reverse mold of SU-8 photoresist on a silicon wafer. After complete curing at room temperature for 48 h, two holes were punched for the inlet and outlet, and the layer was plasma bonded (Harrick Plasma, ambient air) to a thin PDMS layer (1.5 mm thick) with a circular hole (4 mm diameter) to create a holding well for emulsions. The two bonded layers were then transferred and bonded to another layer of flat PDMS bonded to the glass slide for additional support (Figure 2.28). PDMS microfluidic device channels and the droplet well were first treated with 0.1 M NaOH to increase the hydrophilicity of the walls. Continuous phase and droplets were then added to the well. After the initial morphology was recorded, pump 2 (continuous phase) flow rate was set to a standard 100 μL/min and pump 1 (analyte, 12.5−50 mM) flow rate was adjusted to achieve 0.25−1.1 equiv of the analyte to triggerable-surfactant concentration. The analyte and continuous phase meet at the T-junction and start reacting. Continuous flow through the droplet well was sustained for 3 min to completely exchange the original continuous phase in the well with the mixed analyte/continuous phase from the T-junction. After 3 min, both pumps were stopped, and clips placed on the inlet and outlet tubing to isolate the droplet well and to allow further reaction between the analyte and triggerable surfactants without additional flow.

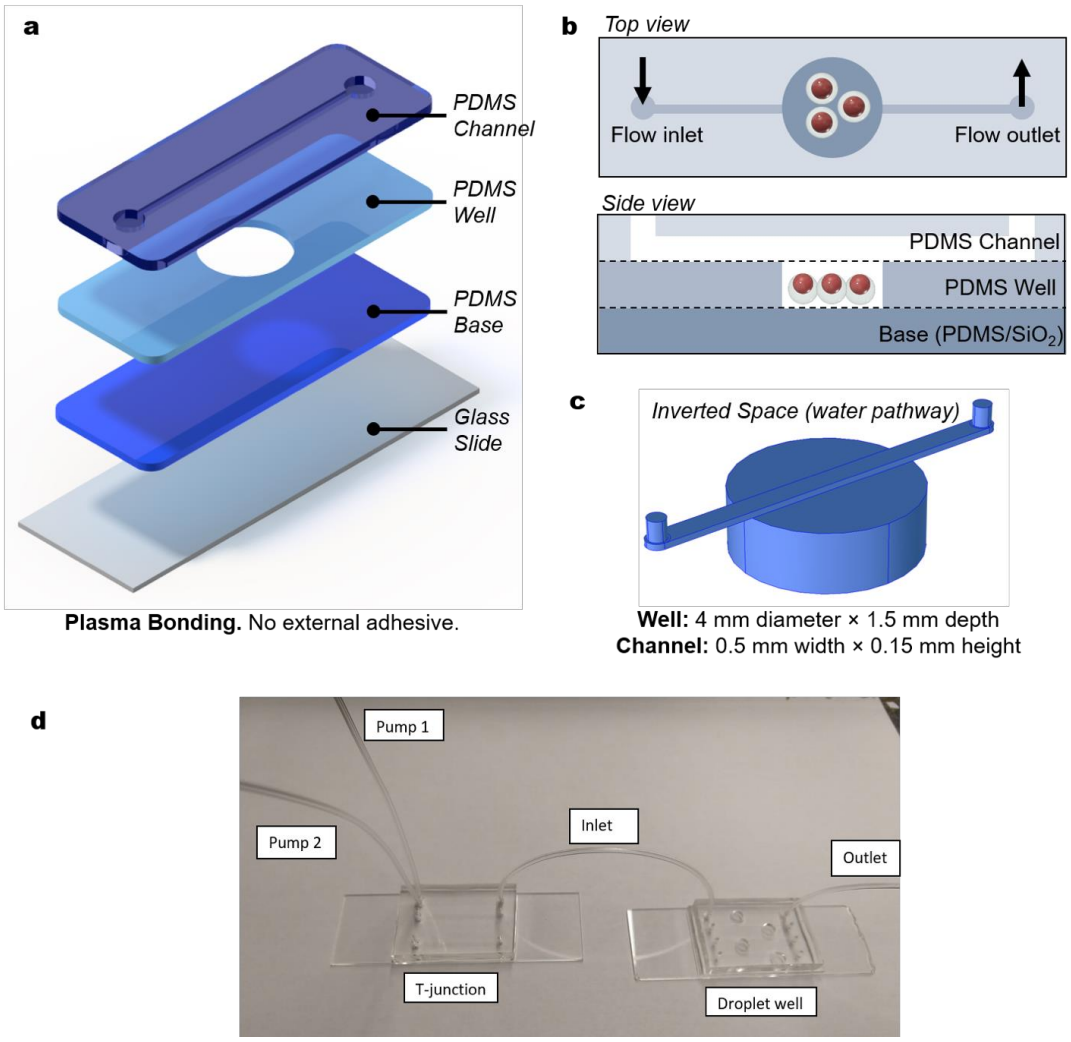

FIGURE 2.28: PDMS microfluidic device setup. a) Layering of PDMS components and glass slide base; b) Schematic of top and side view of droplet well; c) Representation of water pathway in droplet well. For emulsions denser than water, droplet well orientated as shown above. For emulsions less dense than water, setup was inverted; d) Full microfluidic device with T-junction and tubing.

A glass chamber device was fabricated for single emulsion studies without flow. Two pieces of double-sided tape were placed on a glass slide 1 cm apart (height of 70 µm). A coverslip was placed over the tape to form a thin chamber. In general, 20 µL of single emulsion droplets were injected into the chamber for all studies. Then, 10 µL of the analyte solution was added to one end of the chamber to allow slow diffusion into the emulsion system. For studies without flow, double

emulsions were tested in an Invitrogen Attofluor Cell Chamber (ThermoFisher). In general, 10−20 μL of double emulsions were placed in 400 μL of the continuous phase. After the initial morphology was recorded, the analyte solution was added and allowed to sit to track morphology changes over time. For all studies presented in this report, the emulsion studies and reactivity were started at neutral pH before the addition of nucleophiles.

i. Polyurethane studies:

For PU studies, xylene diisocyanate (XDI) in hexane (50 mg/mL) was mixed with aqueous 1,1,1-tris(hydroxymethyl)ethane solution (8 mg/mL) at a 1:4 volume ratio, also containing TEA12 at 5 mM concentration. After hand shaking for 10 s, 1.1 equiv. (5.5 mM) piperidine with respect to TEA12 was introduced to facilitate triggered release (Figure 2.33).

2.3 RESULTS AND DISCUSSION

a. Surfactants and emulsion system design:

The structures of the triggerable surfactants, used in this study, are shown in Figure 2.29a, b. These structures are based on a quaternary ammonium moiety installed at the α-methyl carbon of an alkyl-methacrylate molecule. From a surfactant perspective, the quaternary ammonium moiety serves as the hydrophilic head group and the long alkyl chain as the hydrophobic tail. The inherent Michael acceptor properties of the acrylate moiety are further aided by the quaternary ammonium moiety as the leaving group. The triggering feature of these surfactants is highlighted by the fact that they are susceptible to a formal SN2′ reaction, where incoming nucleophiles would release the quaternary ammonium moiety (Figure 2.29a). Such a reaction would deprive the surfactant of the charged hydrophilic head group causing it to alter its interfacial stabilization characteristics. The nature of the leaving group has a profound influence on the kinetics of the Michael addition

reaction. This feature is taken advantage of for tuning the kinetics of emulsion-triggering with nucleophiles. The generally anticipated reactivity profile is expected to follow the following order (from fastest to slowest): tetraalkylammonium-12 (TEA12), pyridinium-12 (PYR12), and 4-dimethylaminopyridinium-12 (DMAP12).

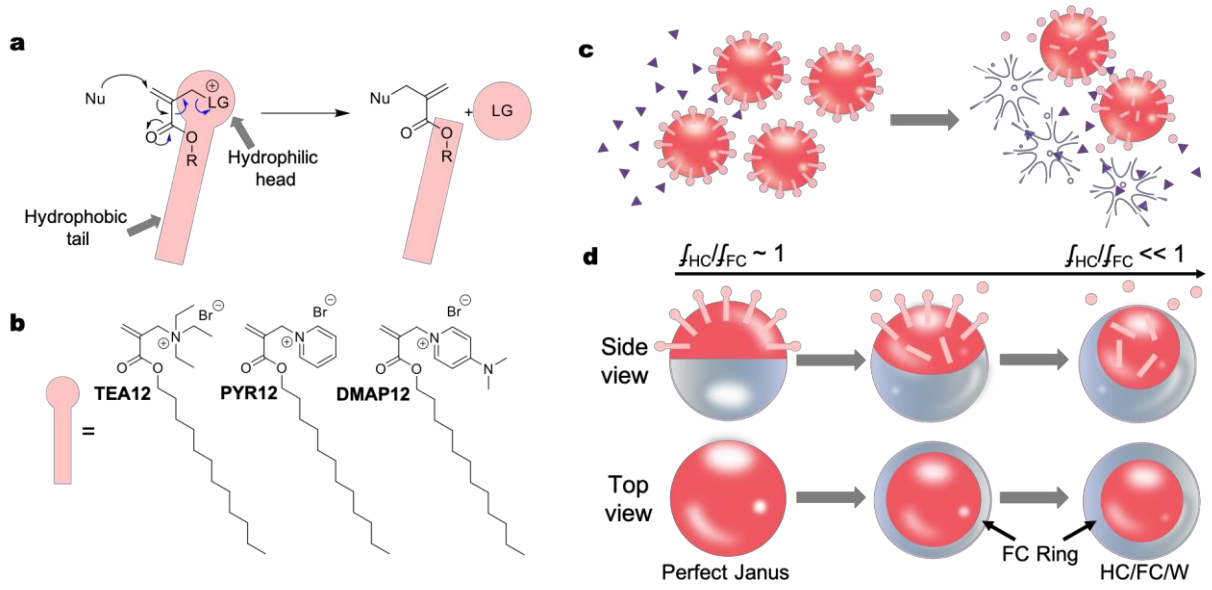

FIGURE 2.29: Design of reactive surfactants and emulsions. a) Design of reactive amphiphilic HC-surfactants undergoing nucleophile-triggered cleavage; b) Chemical structures of HC-surfactants in this work; c) Bursting of single emulsions as the result of nucleophile (purple triangles) induced cleavage of charged hydrophilic head groups, thus reducing surfactant strength and destabilizing the HC/W interface; d) Change in morphology of HC (red) and FC (blue) double emulsions from perfect Janus to HC-in-FC-in-water (HC/FC/W) in response to the decrease in mass fraction of reactive HC-surfactant ($\int_{HC}$) to the FC-surfactant ($\int_{FC}$) with the addition of a nucleophile and resulting HC-surfactant cleavage. Changes in morphology are tracked optically by observing the increase in size of the FC-ring. Nucleophile, surfactants, and emulsion sizes not to scale.

In systems comprising hydrocarbon-in-water single emulsions (HC/W), the nucleophile-triggered reactions destabilize the HC/W interface to cause emulsions to break and phase separate from the aqueous solution; during this process, the emulsions appear to “burst” to the naked eye

(Figure 2.29c). In double emulsions, comprising immiscible HC and fluorocarbon phases (FC) with an FC co-surfactant, the destruction of the HC-surfactant would give rise to a clear morphological change. The morphology of dynamic double emulsions is controlled by the balance of interfacial tensions (γ) at the HC/W and FC/W interfaces, and a Janus state will transform into an encapsulated morphology in response to changes in the relative strength or concentration of surfactants stabilizing one of the interfaces.[17] In a co- surfactant system, Janus morphology (γHC/W = γFC/W) is achieved with equal amounts of the immiscible liquids and a specific mass fraction of surfactant FC-surfactant (∫HC/ ∫FC). As the HC-surfactant concentration decreases with nucleophilic addition and the benign FC-surfactant concentration stays constant, the ∫HC/∫FC decreases leading to a HC-in-FC-in-W (HC/FC/W) morphology.

The concentration of each HC-surfactant was initially determined to achieve equivalent γHC/W, thereby eliminating differences in the initial emulsion stability in the observed reactivity. Determination of exact interfacial tensions using pendant drop studies were not possible due to the instability of the hexane drops in surfactant solutions over the measurement time frame, making equilibrium interfacial tensions inaccessible. Although not an absolute interfacial tension measurement, the geometry at the junction between the three phases of double emulsions can be used to determine relative interfacial tension at the HC/W and FC/W boundaries.[17] At a given morphology, the relative ratio of interfacial tensions at HC/W and FC/W interfaces will be consistent across different emulsion and surfactant systems. Therefore, estimations of equal γHC/W were qualitatively determined through matching morphologies for each double emulsion system. The γFC/W is held constant across samples, and the γHC/W is adjusted to be equal for each of the three HC-surfactants. To this end, polydisperse double emulsions of hexane/FC-770 in water with a uniform configuration were readily obtained by phase separation emulsification.[52] A

constant 0.2 wt % FC-surfactant Zonyl FS-300 (Zonyl) was maintained and the concentrations of the HC-surfactants were adjusted to produce the perfect Janus morphology, where $\gamma_{HC/W} = \gamma_{FC/W}$. Specifically, 5 mM TEA12, 4 mM PYR12, or 4 mM DMAP12 provided the fractions of HC-surfactant to Zonyl($\int_{HC}/\int_{FC}$) necessary to yield perfect Janus emulsions (Figure 2.24). These $\int_{HC}/\int_{FC}$ were utilized in all the double emulsion studies. These concentrations were found to be above the critical micelle concentration for each surfactant, which were calculated to be 0.6, 1.2, and 1.5 mM for TEA12, PYR12, and DMAP12, respectively (Figure 2.25-2.27).

b. Small Molecule Nucleophile Studies:

As a first step, the strategy and kinetic control were validated with a small molecule trigger: 2-(2-methoxyethoxy)ethanethiol (EG_2-SH). Using a poly(dimethylsiloxane) (PDMS) microfluidic array device, the emulsions were exposed to precise equivalents of the analyte trigger by controlling the flow rates (analyte in pump 1 and surfactant in pump 2, Figures 2.28 and 2.30a). The reactivity of the surfactants is reflected in the time required for single emulsion bursting and the extent of bursting, which depends on the rate of decrease in $\int_{HC}$. Introduction of 1.1equiv. (5.5 mM) EG2-SH relative to the TMAc surfactant triggered bursting in TEA12-stabilized single emulsions within 45 s. After 5 min, 90% of the single emulsions had burst and macroscopic phase separation of hexane/water was observed (Figure 30b). PYR12 and DMAP12 displayed slower rates with the onset of bursting occurring only after 3 min with the addition of 1.1 equiv (4.4 mM) EG_2-SH. In addition, at the end of 15 min, a significant amount of PYR12 and DMAP12 single emulsions was still intact compared to TEA12, which had completely burst and phase-separated over the same time frame. Control experiments performed with cetyltrimethylammonium bromide

(CTAB, 1 mM)-stabilized hexane emulsions revealed no response to the addition of 1.1 equiv (1.1 mM) EG_2-SH (Figure 2.34).

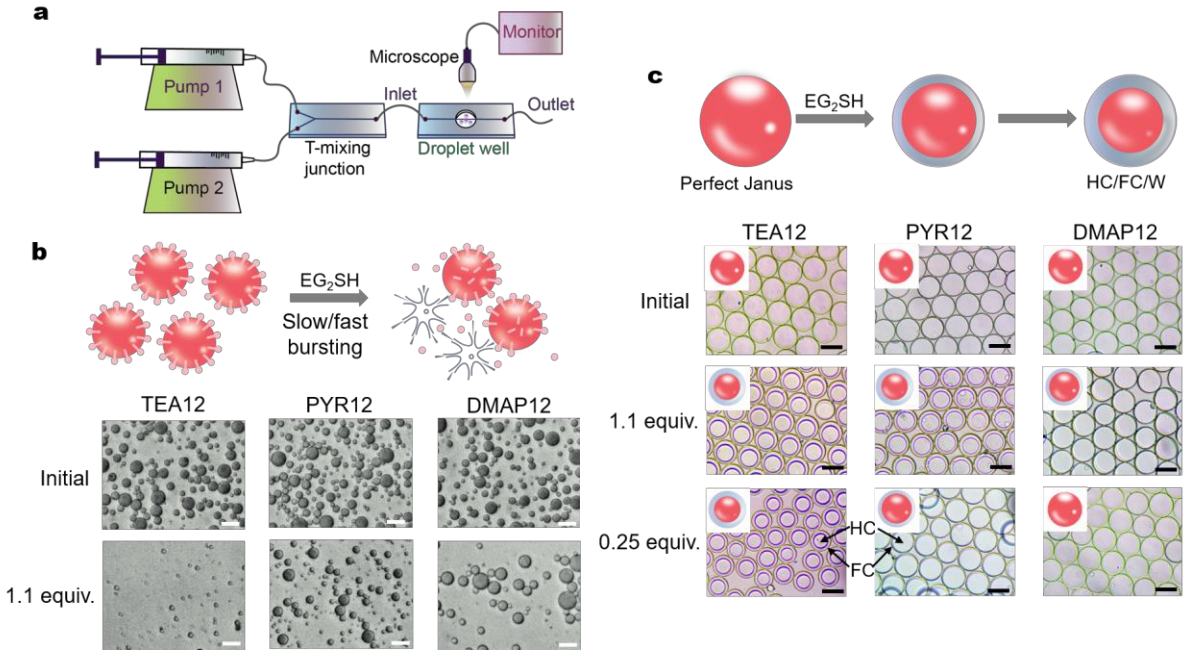

FIGURE 2.30: Small molecule trigger studies. a) PDMS microfluidic device for controlled analyte addition; b) Schematic and optical microscopy images of single emulsions stabilized by TEA12, PYR12, and DMAP12 before and after 1.1 equiv. EG_2-SH addition: TEA12 droplets after 8 minutes, PYR12 and DMAP12 droplets after 15 minutes; c) Top-view schematic and optical microscopy images of double emulsion morphology before and after 1.1 equiv. or 0.25 equiv. EG_2-SH addition (1 min after addition). Scale bar = 50 μm.

The much greater reactivity of TEA12 is consistent with kinetic studies performed by Zhuang et al. with TMAc-based small molecule reactions with thiols.[25] The slower reactivity of the pyridinium-based TMAc molecules is understood based on the resonance stabilization of the positive charge, which results in a weaker leaving group in the formal SN2′ reaction. In their study, PYR12 reacted slower with thiol compared with DMAP12 contrary to expectations of reactivity based on structure alone. They reasoned that the DMAP base leaving group boosts the nucleophilic reactivity of the thiol and thereby contributed to accelerated reactivity. The reactivity trend of TEA

> DMAP > PYR was reflected in kinetic studies performed on the triggerable HC-surfactants (Figures 2.23-2.29). Studies in D_2O were prohibitive because of the insolubility of the product; therefore, experiments were performed in acetone-*d6*. We observed reaction completion within 15 min for TEA12 and 24 h for DMAP12 with 1.1 equiv EG_2-SH; however, conversion of PYR12 was only observed after >2 days. The agreement of the kinetic results demonstrates that the added hydrophobic tail does not inherently change the reactivity. Kinetic studies confirmed the superior reactivity of TEA12 demonstrated in the single emulsion system. However, PYR12 and DMAP12 did not have differentiated reactivity in bursting studies, contrary to kinetic expectations. The reactivity of PYR12 vs DMAP12 leaving groups is greatly dependent on contributions from bases.[25] Our emulsion systems likely display a different reactivity because of the biphasic solvent contributions, wherein the basic leaving groups partition partially into the oil phase, diminishing their contribution to overall reactivity; we, therefore, expect trends more similar to those based on structure alone. We also note that all emulsion studies are conducted starting at neutral conditions. As Zhuang et al. observed, basic conditions can accelerate the reactivity of the formal SN2′ reaction.[25] In addition, pH conditions can have an impact on nucleophile strength (extent of protonation) and surfactant stability (increased hydrolysis at basic conditions). As a result of the complexity of pH influence on reactivity, pH sensitivity was not investigated in this study.

As a complement to bursting the single emulsions with the nucleophile-induced reaction at the emulsion interface, we explored the potential morphological changes in double emulsions in response to this process. The rate and extent of change in morphology resulting from a decrease in∫ HC/∫FC after nucleophile addition can also be used as a metric to characterize the reactivity in the double emulsion system because of complex double emulsion morphology sensitivity to subtle changes in the surfactant environment. Further, any changes in morphology provide an optical

readout because of HC/FC double emulsion micro lens properties, which, if desired, can be exploited for sensitive detection of nucleophile triggers.[30] In the present studies, the changes were measured by tracking the increase in FC-ring size under an optical microscope, which provided valuable information on the macroscopic response to nucleophile triggers. Janus droplets stabilized by TEA12/Zonyl and PYR12/Zonyl rapidly formed encapsulated HC/FC/W double emulsions with the addition of 1.1 equiv (5.5 and 4.4 mM, respectively) EG2-SH within 1 min of flow through the PDMS device (Figures 30c and 38). DMAP12/Zonyl system, however, displayed the anticipated slower reactivity as evidenced by the smaller morphology change after 1 min exposure to 1.1 equiv (4.4 mM) EG2-SH. The slower reactivity of DMAP12, compared to PYR12, is understood as the electron-donating dimethylamino moiety offers greater resonance stabilization of the positive charge in the TMAc molecule. Surprisingly, though, there was no discernible difference between TEA12 and PYR12, and thus, we resorted to lowering the concentrations. Indeed, clear reactivity differences between TEA12 and PYR12 were revealed at 0.25 equiv (1.25 mM and 1 mM, respectively) EG2- SH addition after 1 min of flow; full morphology changes were observed with TEA12/Zonyl-stabilized double emulsions, whereas PYR12/Zonyl-stabilized emulsions were largely unaffected owing to the lower rate of reaction (Figure 30c). The double emulsion system allowed for clear differentiation in reactivity between the three HC-surfactants, particularly in differing macroscopic responses for PYR12 and DMAP12. In control experiments, no morphology changes were observed after the addition of 1.1 equiv (1.1 mM) EG2-SH to CTAB/ Zonyl-stabilized double emulsions (Figure 40).

Overall, the reactivity in double emulsions followed the trend TEA12 > PYR12 > DMAP12, faithfully reflecting the anticipated reactivity based on the structures of the HC-surfactants. As discussed, the observed difference between kinetic experiments in acetone-d6 and

the rate of morphology changes is attributed to reduced contributions from the base because of the multisolvent system. In both single and double emulsion systems, a simple small molecule thiol successfully triggered bursting and morphology changes through the reduction in ĴHC, with rates in accord with the surfactant reactivity trends. While quantitative kinetic reactivity is not measurable with the macroscopic observations, the emulsion responses can reflect microscopic reactivity.

To further show the control over the reaction, additional nucleophiles were studied: hexamethylenediamine (HMDA), ethanol, and acetic acid (See "Control studies"). Conversely, weaker nucleophiles such as ethanol and acetic acid are not expected to react with the HC-surfactants quickly, as was demonstrated by a lack of response in both the single and double emulsion systems (Figures 2.37 and 2.42). Overall, our results demonstrate the control over single and double emulsion system stability with simple triggers and by tuning the reactivity of the surfactants. Furthermore, we investigated the potential for a controlled release of reagents to lead to on-demand polymerization to synthesize polyurethane. In our system, diisocyanate encapsulated in TEA12 stabilized single emulsions was protected from reacting with triol in the continuous phase by the TEA12 surfactant layer. Upon triggering with piperidine, a nucleophile, the triggered release into the triol-containing continuous phase initiated an on-demand polymerization in a one-pot system (Figure 2.33).

c. Molecular Assembly Nucleophile Studies:

Having validated the approach with small molecule triggers, we explored the possibility of a three-dimensional (3D)-assembly triggering a response in the emulsions systems, thus broadening nucleophile trigger types for potential applications. Studies with a small-molecule

amine, HMDA, showed a similar reactivity profile to EG2-SH, demonstrating the capability of utilizing amines as a trigger. Subsequently, we synthesized an amphiphilic block copolymer that is functionalized with a primary amine moiety at the hydrophilic terminus (amine-P2, Figure 2.31).

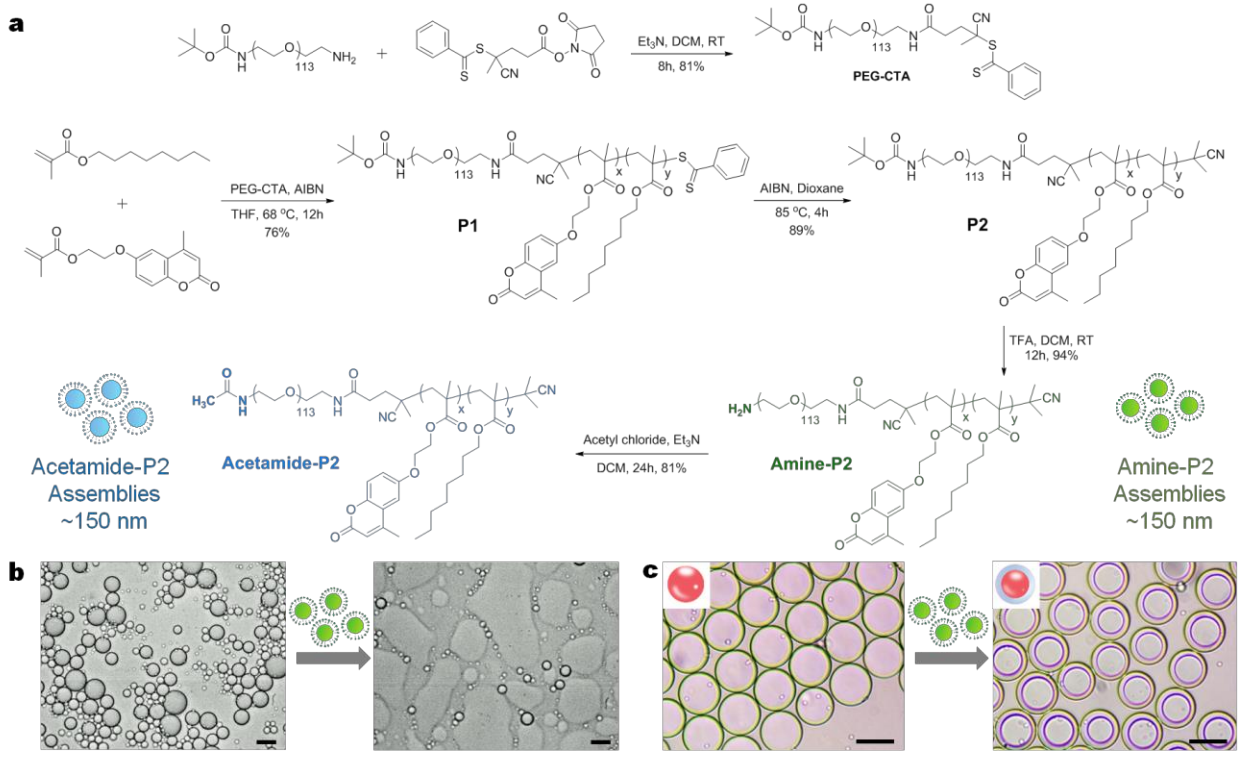

FIGURE 2.31: Amine functionalized assembly studies. a) Synthesis, self-assembly, and assembly size of amine and acetamide end-functionalized amphiphilic polymer (Amine-P2 and Acetamide-P2, respectively); b) Optical microscopy images of single emulsion bursting with addition of Amine-P2 after 3 min; c) Top-view optical microscopy images of the morphology changes observed with the addition of Amine-P2 to Janus double emulsions after 3 min. Amine-P2 assemblies are not visible in microscopy images. Scale bar = 50 μm.

As a result of amine-P2′s amphiphilic nature, the polymers self-assemble in water to form nanoassemblies with an amine-functionalized surface. The resulting assembly of amine-P2 was found to occur at concentrations of 0.25 mg/mL or greater and formed assemblies of ~150 nm,

which is consequently too small to be observed optically in emulsion reactivity studies (Figures 2.21 and 2.43). To study these processes, we adjusted our testing setup to allow for direct diffusion-controlled contact of the trigger without flow/ continuous agitation. The testbed includes a glass enclosure with an opening on the side to introduce the analyte into single emulsion samples, which are less dense than water. An open-air microscope chamber was used for double emulsions that are denser than water. The new diffusion-limited test protocol was also validated with EG2-SH and HMDA to TEA12-stabilized single emulsions and TEA12/Zonyl-stabilized double emulsions and observed instantaneous bursting and morphology changes, respectively (Figures 2.36 and 2.41). Experiments were then performed by introducing amine-P2 assemblies to TEA12-stabilized single emulsions. Within 2 min of introduction, the onset of bursting was observed with complete emulsion destruction in under 3 min (Figure 2.31b).

Similarly, the morphology of TEA12/Zonyl-stabilized double emulsions exhibited complete conversion to the encapsulated HC/FC/W morphology within 3 min due to the decrease in $\int_{HC}/\int_{FC}$ (Figure 2.31c). Since the nucleophile-laden "attacking" assembly is amphiphilic in nature, it is possible that simple interfacial contact could cause modifications in the emulsion interfacial stability without the need for a specific nucleophile-induced modification of the interfacial stability. To test for this possibility, the amine moieties in the amine-P2 functionalities were converted to the corresponding amide moieties to form acetamide-P2 assemblies. Acetamide-P2 self-assembles at concentrations of 0.22 mg/mL or greater with an average size of ~150 nm (Figures 2.21 and 2.43). When this assembly, which is identical to the amine-P2 assembly except for the nucleophilic functionality, was introduced to either the single or the double emulsion systems, no bursting or morphological changes were observed (Figures 2.43-2.44). Since these experiments were performed above the CAC of amine-P2 and acetamide-P2, it is likely that

induced changes in the emulsions are a result of assembly interaction with the surfactants at the emulsion interface and/or in the bulk solvent rather than the reaction of free polymer chains in solution. These results confirm that both the single and double emulsion macroscopic responses are triggered through assembly-induced modulation of the TMAc surfactants.

d. Light-triggered cascade studies:

We were next interested in evaluating the possibility of causing trans- formations in the emulsions by the actuated release of a small molecule from another assembly, thereby modulating emulsion response with an additional control beyond nucleophile addition. To this end, we utilized a recently reported polymerosome, generated through the self-assembly of an amphiphilic diblock copolymer comprising hydrophilic poly(ethylene glycol), an azobenzene linker, and a hydrophobic polylactide (PAP).[28] This assembly has been shown to exhibit on-demand release of guest molecules from the lumen of the assembly (Figure 2.32a). This process represents a far-from-equilibrium behavior of the polymerosome, as the molecular release is observed only in the presence of an active energy source. We were interested in investigating the possibility of bringing this module into our system, to generate a cascade effect. For our experiments, we loaded PAP assemblies with HMDA as the guest molecule (PAP-HMDA). Mixing the PAP-HMDA assembly with the TEA12-stabilized emulsions did not cause any bursting or morphological changes (Figure 2.46 and 2.48). However, when the same PAP-HMDA assembly was first exposed to light for ~25 minutes, bursting and morphology changes indeed occurred in the single and double emulsion systems, respectively (Figure 2.32c, Figure 2.48). PAP assemblies are ~200 nm in size, and therefore are not visible in the microscope images. To further validate the response seen, HMDA

at low equiv. was studied with TEA12 emulsions. At equiv. similar to those expected to that which is released, morphology changes and bursting was observed (Figure 2.45 and 2.47).

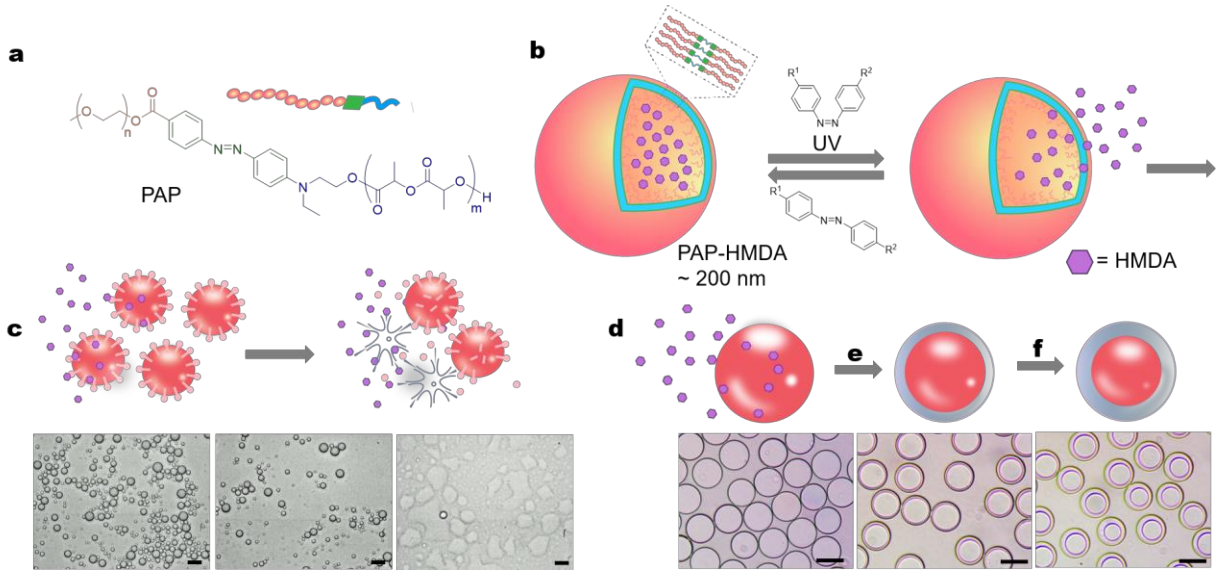

FIGURE 2.32: Controlled on-demand triggered release and response. a) Amphiphilic diblock copolymer (PAP) with hydrophilic (orange) and hydrophobic (blue) units linked with an azobenzene unit (green); b) PAP self-assembles into a vesicle (~200 nm in size) for UV-triggered release of HMDA (purple hexagon); c) Schematic and optical microscopy images of single emulsion bursting after pre-release of HMDA. Images from left to right – initial, 2 min and 3 min after addition; d) Top-view schematic and microscopy images of the morphology changes with in situ irradiation of PAP-HMDA with e) 5 min of irradiation and f) 10 total min of irradiation. PAP vesicles are not visible in microscopy images. PAP, HMDA, and emulsion size in schematic representations are not to scale. Scale bar = 50 μm

To better demonstrate the cascade process, PAP-HMDA was first introduced to the double emulsion system and then photo-isomerized in situ; the release behavior and cascade effect can be concurrently observed. We expect the double emulsions to exhibit morphology changes only upon

exposure to UV light and by removing the UV source, no additional changes in morphology should occur. This modulation of an on/off morphology change with UV light exposure cycles was faithfully demonstrated. Upon exposure to UV light for 5 min, the double emulsions underwent morphology changes and did not change further upon resting in ambient conditions for 5 additional minutes (Figure 2.32d, e). An additional 5 min of UV light exposure resulted in a further change in morphology, as demonstrated by an increase in the FC-ring size in the optical micrographs (Figure 2.32f). Under ambient conditions without any light exposure, no additional morphology changes were observed (Figure 2.49). Put together, these results show that an in situ actuatable assembly can be combined as a module to impart emulsion sensitivity to an entirely different stimulus (light). A lack of response in the emulsion systems upon the addition of PAP-HMDA before irradiation confirms the encapsulation of the nucleophile within the PAP-HMDA vesicles and the far-from-equilibrium release of the nucleophile in the presence of light (Figure 2.48).

Finally, we investigated the potential for a controlled release of reagents to lead to on-demand polymerization. In our system, di-isocyanate encapsulated in TEA12 stabilized single emulsions was protected from reacting with triol in the continuous phase by the TEA12 surfactant layer. The addition of nucleophile burst the single emulsions facilitating the reaction between isocyanate and triol to form polyurethane (PU) on demand.

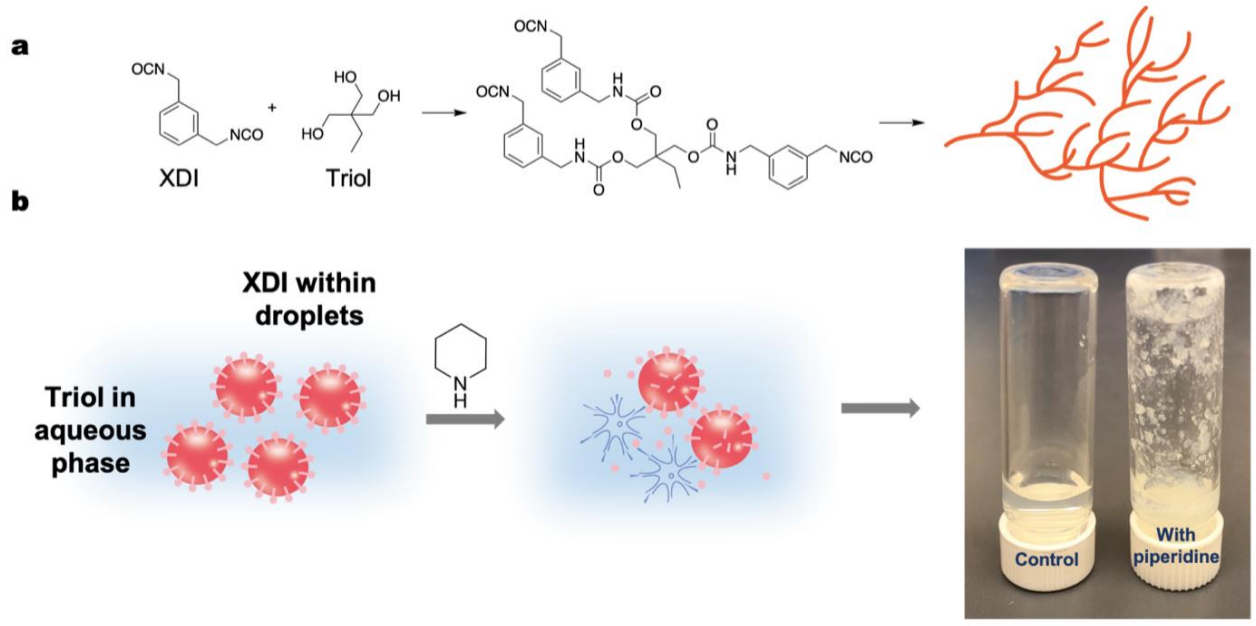

FIGURE 2.33: Trigger induced polyurethane formation. a) Polyurethane formation scheme; b) Nucleophile induced bursting of XDI in hexane single emulsions masked by a TEA12 layer to form a polyurethane foam with water soluble triol (images taken after 20 minutes).

2.4 CONTROL EXPERIMENTS

2.4.1. SMALL MOLECULE NUCLEOPHILE STUDIES

SINGLE EMULSION STUDIES

EG_2-SH controls in microfluidic setup:

Control experiments were performed using 1 mM CTAB stabilized emulsion droplets in the microfluidics device by introducing 1.1 equiv. (1.1 mM) EG_2-SH. As expected, no bursting was observed even after 20 minutes of analyte introduction to the CTAB single emulsions (Figure 2.34).

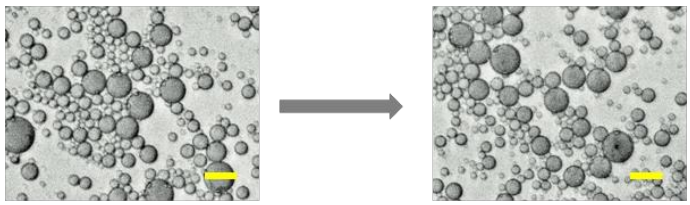

FIGURE 2.34: CTAB control studies, where no bursting was observed after introduction of 1.1 equiv. EG_2-SH (after 20 min). Scale bar = 50 μm.

HMDA in microfluidic array:

Studies were performed by flowing 1.1 equiv. (5.5 mM) HMDA into the microfluidics array containing 5 mM TEA12 single emulsion droplets. Bursting was observed within 3 minutes and continued over a total of 12 minutes (Figure 2.35).

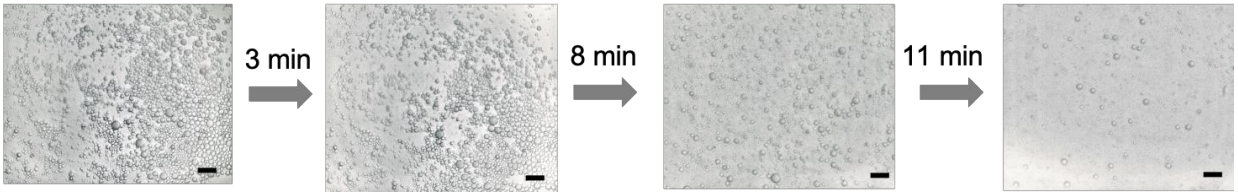

FIGURE 2.35: TEA12 single emulsion studies with 1.1 equiv. HMDA. Scale bar = 50 μm.

EG_2-SH and HMDA in no flow setup:

Single emulsions were prepared using the TEA12 surfactant and 20 μL of the droplets were injected into the glass chamber no flow setup using a micropipette. To compare the PDMS microfluidic testing device results and the glass chamber setup, 10 μL of 1.1 equiv. (5.5 mM) EG_2-SH or HMDA was loaded on one of the open ends of the chamber. Instant bursting was observed and completed within 3 min for EG_2-SH (Figure 2.36). However, with 1.1 equiv. (5.5 mM) HMDA, bursting was observed ~3 minutes after the addition of HMDA and continued over the next 10 minutes. These results are consistent with the microfluidic testing device.

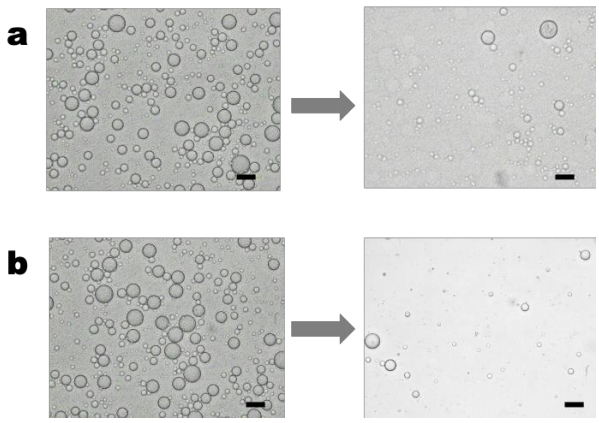

FIGURE 2.36: TEA12 droplets before and after the addition of a) 1.1 equiv. EG_2-SH and b) 1.1 equiv. HMDA. Scale bar = 50 μm.

Ethanol and acetic acid in no flow setup:

To further test the response of the surfactants to different nucleophiles, single emulsions were prepared using the TEA12, PYR12, and DMAP12 surfactants. 20 μL of the droplets were injected into the glass chamber no flow setup using a micropipette, followed by addition of 10 μL of 1.1 equiv. (5.5 for TEA12; 4.4mM for DMAP12 and PYR12) of ethanol or acetic acid to one of the open ends of the chamber. As anticipated, minimal bursting was observed when ethanol and acetic acid were introduced over 15 minutes (Figure 2.37).

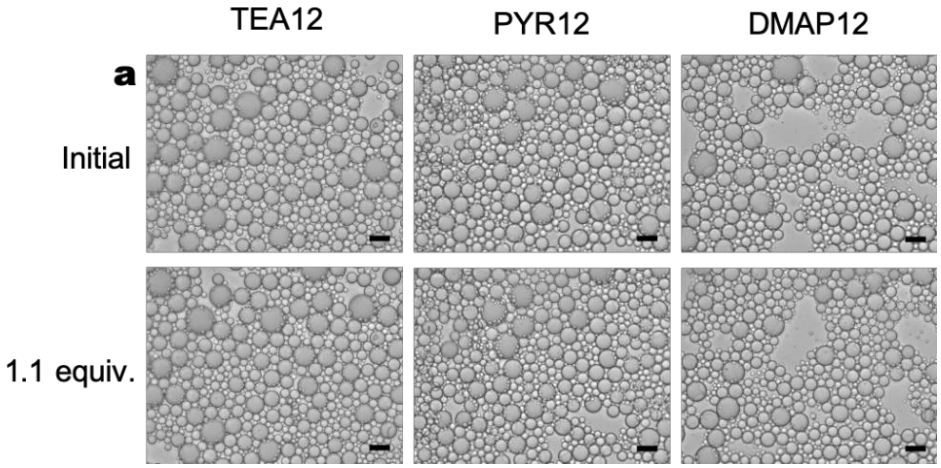

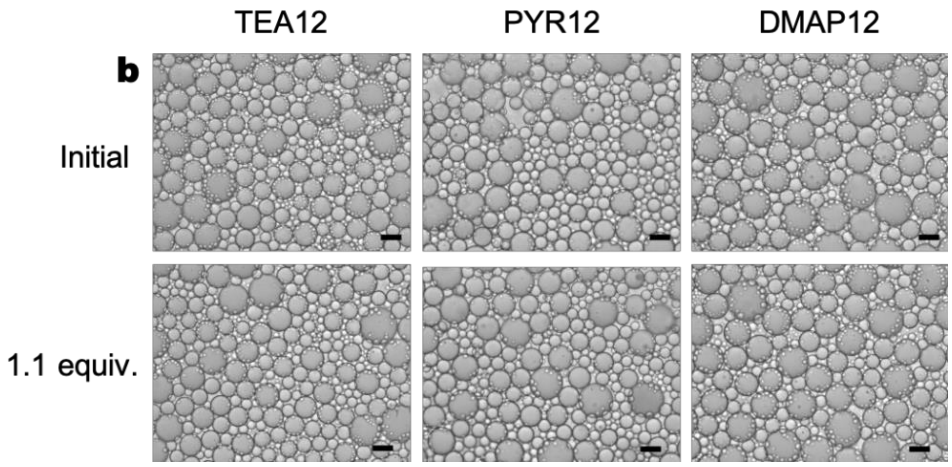

FIGURE 2.37: TEA12, PYR12 and DMAP12 droplets before and after the addition of, a) 1.1 equiv. ethanol and b) 1.1 equiv. acetic acid. Scale bar = 50 μm

DOUBLE EMULSION STUDIES

EG2-SH equivalence study in microfluidic array:

Using the PDMS microfluidic device and following the general procedure, 0.25-1.1 equiv. (1.25- 5.5 mM for TEA12 and 1-4.4 mM for DMAP12 and PYR12) of EG2-SH was introduced to double emulsions stabilized by 0.2 wt% Zonyl and either 5 mM TEA12, 4 mM PYR12, or 4 mM DMAP12. For the studies, the final morphology, wherein no more morphology changes occur with additional reaction time, and the time necessary to reach the final morphology were recorded. In Figure 2.38, the final morphology achieved for each equivalence of thiol added is shown, and the time required to reach that final morphology is additionally provided. At 1.1 equiv, both TEA12/Zonyl and PYR12/Zonyl droplets were quick to reach the final HC/FC/W morphology, while DMAP12/Zonyl emulsions took an additional 2 min. At 0.5 equiv. the difference in reactivity was further demonstrated with DMAP12/Zonyl, which showed the least change in morphology, only deviating a minimal amount from the perfect Janus morphology. The difference in reactivity between TEA12 and PYR12 was demonstrated at 0.25 equiv., where the final

morphology in PYR12 was achieved after 2 min, compared to TEA12 final morphology reached after 1 min.

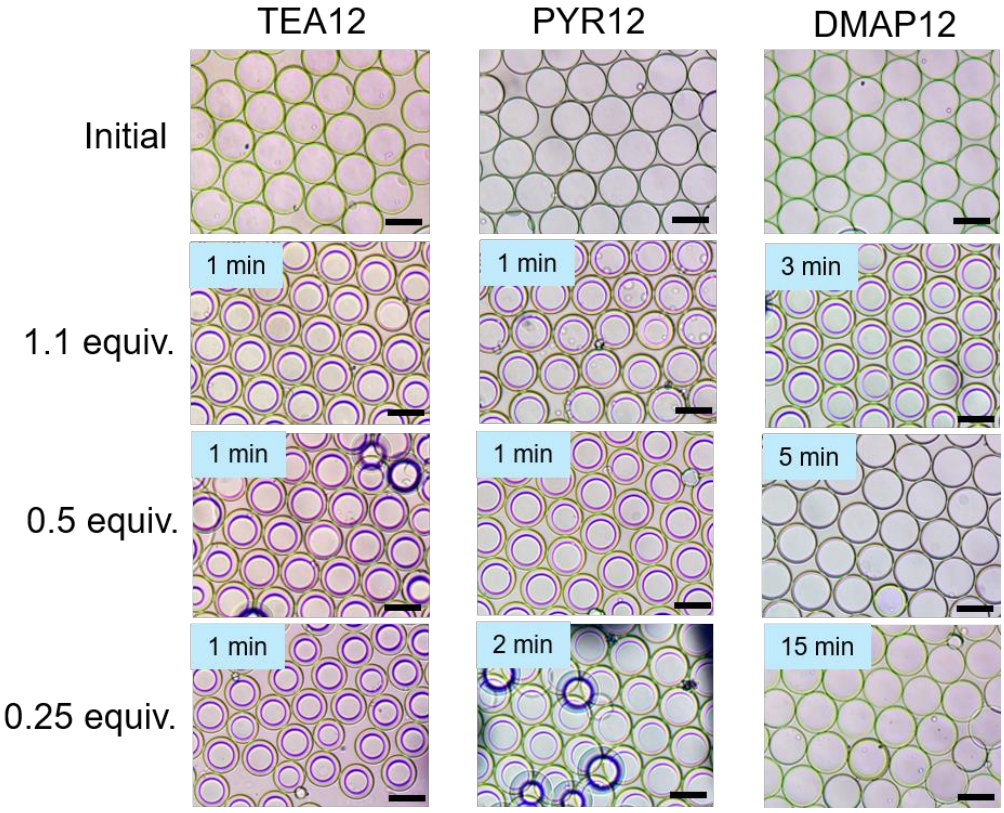

FIGURE 2.38: EG_2-SH equiv. study with Zonyl and HC-surfactants. Time to final morphology (blue box) is shown. Scale bar = 50 μm

HMDA study in microfluidic array:

Using the PDMS microfluidic device and following the general procedure, 1.1 equiv. (5.5 mM for TEA12 and 4.4 mM for DMAP12 and PYR12) of HMDA was introduced to double emulsions stabilized by 0.2 wt% Zonyl and either 5 mM TEA12, 4 mM PYR12, or 4 mM DMAP12. In Figure S39, the final morphology achieved is shown with the time required to reach that final morphology. With the addition of 1.1 equiv. HMDA, TEA12/Zonyl and PYR12/Zonyl showed complete conversion after 2 min, but appreciable bursting of the TEA12/Zonyl double

emulsions was also observed, with some bursting observed with PYR12/Zonyl. We reasoned the interface was highly destabilized due to rapid reduction of *f*HC, leading to bursting and morphology changes. Over 5 min, small morphology changes and no bursting were observed with DMAP12/Zonyl double emulsions. At lower equiv. of HMDA (0.25 and 0.5 equiv.), bursting was observed in the TEA12/Zonyl sample, no bursting was observed in the PYR12/Zonyl or DMAP12/Zonyl samples.

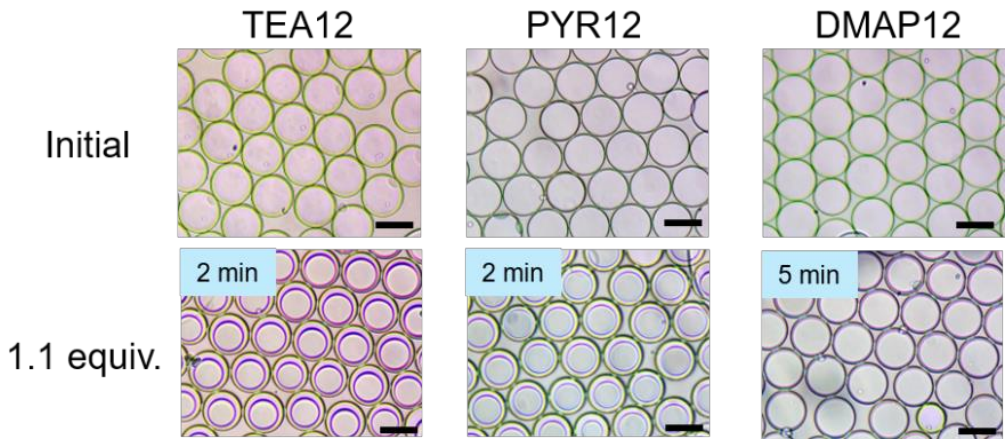

FIGURE 2.39: Double emulsion HMDA study. Time to final morphology (blue box) is shown after the addition of 1.1 equiv. HMDA. Scale bar = 50 μm

EG2-SH and HMDA controls in microfluidic array:

Using the PDMS microfluidic device and following the general procedure, 1.1 equiv. (1.1 mM) of EG2-SH and HMDA were introduced to double emulsions stabilized by 0.2 wt% Zonyl and 1 mM CTAB. CTAB does not contain a leaving group and is not expected to react with the nucleophiles. This was demonstrated by no observed changes in morphology or bursting from initial FC-in-HC-in-W (FC/HC/W) with the addition of EG2-SH or HMDA (Figure 2.40).

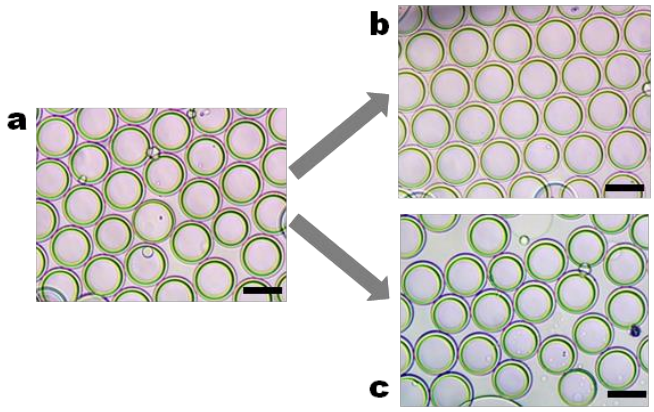

FIGURE 2.40: Control studies with CTAB/Zonyl with the addition of EG_2-SH and HMDA. a) Initial FC-in-HC-in-W (FC/HC/W) morphology; b) No change in morphology with the addition of 1.1 equiv EG_2-SH

EG2-SH and HMDA in no flow setup:

Studies were performed using the double emulsion no-flow setup and general procedure, with double emulsions stabilized by 0.2 wt% Zonyl and 5 mM TEA12. To compare the no flow results to the PDMS microfluidic testing device, 1.1 equiv. (5.5 mM) of EG2-SH and HMDA were added to the double emulsions. Within 1 min, the complete conversion from perfect Janus to HC/FC/W was observed for EG2- SH (Figure 2.41a to b) and HMDA and (Figure 2.41a to c).

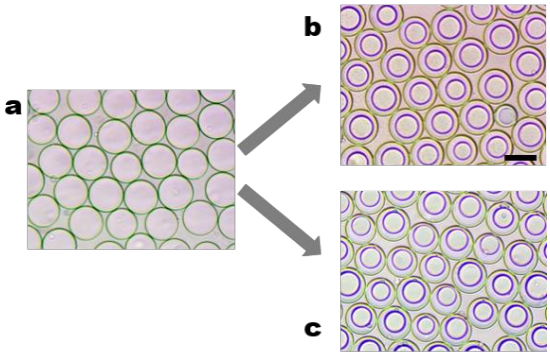

FIGURE 2.41: EG_2-SH and HDMA study in no flow setup. a) Initial perfect Janus morphology of TEA12/zonyl stabilized double emulsions; b) Morphology change observed within 1 min with the addition of 1.1 equiv. EG_2-SH; c) Morphology change observed within 1 min with the addition of 1.1 equiv. HMDA. Scale bar = 50 μm.

Ethanol and acetic acid in no flow setup:

Additional nucleophile studies were performed using the double emulsion no-flow setup and general procedure, with double emulsions stabilized by 0.2 wt% Zonyl and 5 mM TEA12, 4 mM PYR12, or 4 mM DMAP12. 1.1 equiv. (5.5 for TEA12; 4.4 for DMAP12 and PYR12) of ethanol or acetic acid were added to the system. Over 30 min, minimal to no morphology changes were observed.

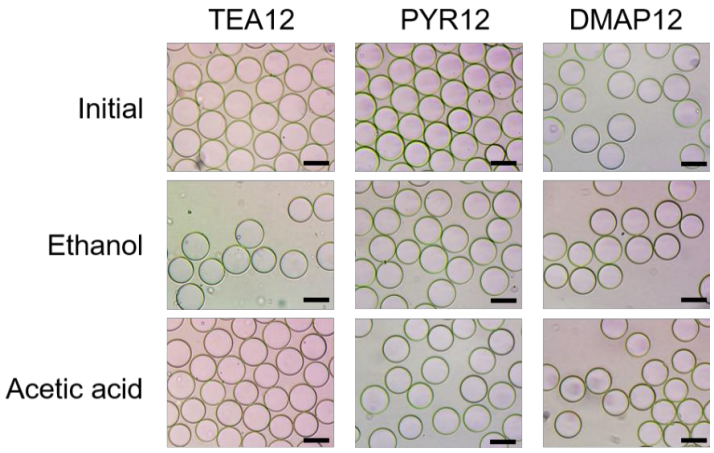

FIGURE 2.42: Ethanol and acetic acid nucleophile studies with Zonyl and HC-surfactant double emulsions. Initial morphology and morphology 30 min after addition of nucleophiles shown for each surfactant. Scale bar = 50 μm

2.4.2. POLYMERIC ASSEMBLY NUCLEOPHILE STUDIES USING AMINE-P2

SINGLE EMULSION STUDIES

Single emulsions – Amine-P2 controls in no flow setup:

Single emulsions were prepared using the TEA12 surfactant and injected into the glass chamber no flow setup using a micropipette. 10 μl of 0.9 mg/mL Acetamide-P2 was used as a control with the TEA12 droplets and no bursting was observed over 5 min (Figure 2.43a). Other

control experiments were set up using single emulsion droplets stabilized by 1 mM CTAB, where Amine-P2 and Acetamide-P2 were introduced at the same concentrations into the glass chamber. No bursting was observed after introduction of the analyte within 5 minutes of observation (Figure 2.43b-c).

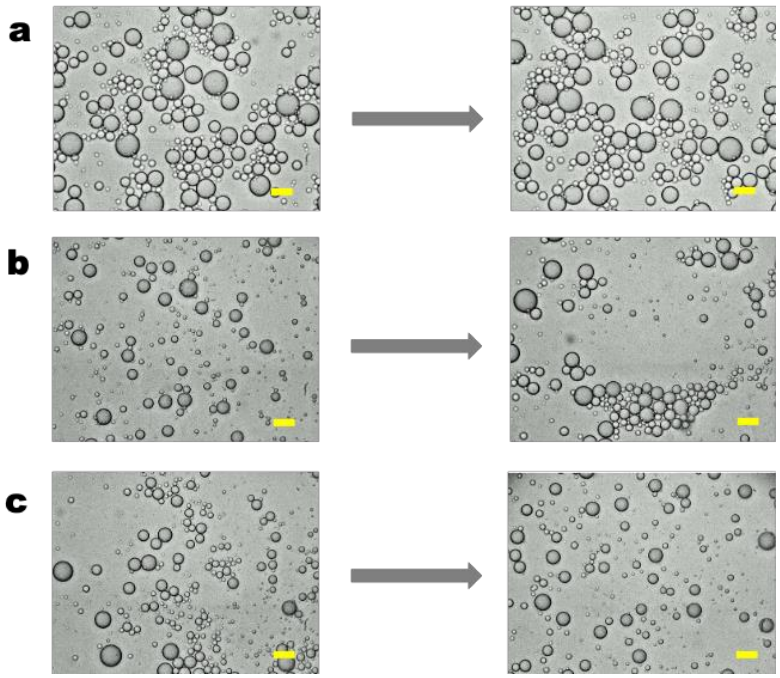

FIGURE 2.43: Control studies with 3D assemblies. a) TEA12 stabilized emulsions exposed to Acetamide-P2 particles after 5 min; b) CTAB stabilized emulsions exposed to Amine-P2 particles after 5 min; c) CTAB stabilized emulsions exposed to Acetamide-P2 particles after 5 min; d) DLS plots of Amine-P2 and Acetamide-P2 assemblies. Scale bar = 50 μm.

DOUBLE EMULSION STUDIES:

Double emulsions – Amine-P2 controls in no flow setup

Studies were performed using the double emulsion no-flow setup and general procedure, with double emulsions stabilized by 0.2 wt% Zonyl and 5 mM TEA12. Controls for the Amine-

P2 studies were performed by adding 20 µL of 4 mg/mL Acetamide-P2 particles to the double emulsions. No morphology changes were observed after 30 min (Figure 2.44a).

Further control studies were performed with 0.2 wt% Zonyl and 1 mM CTAB stabilized double emulsions. To the double emulsions, 20 µL of 4 mg/mL Amine- P2 in water was added. No changes in morphology from initial FC/HC/W morphology were observed with the addition of Amine-P2 over 60 min (Figure 2.44b).

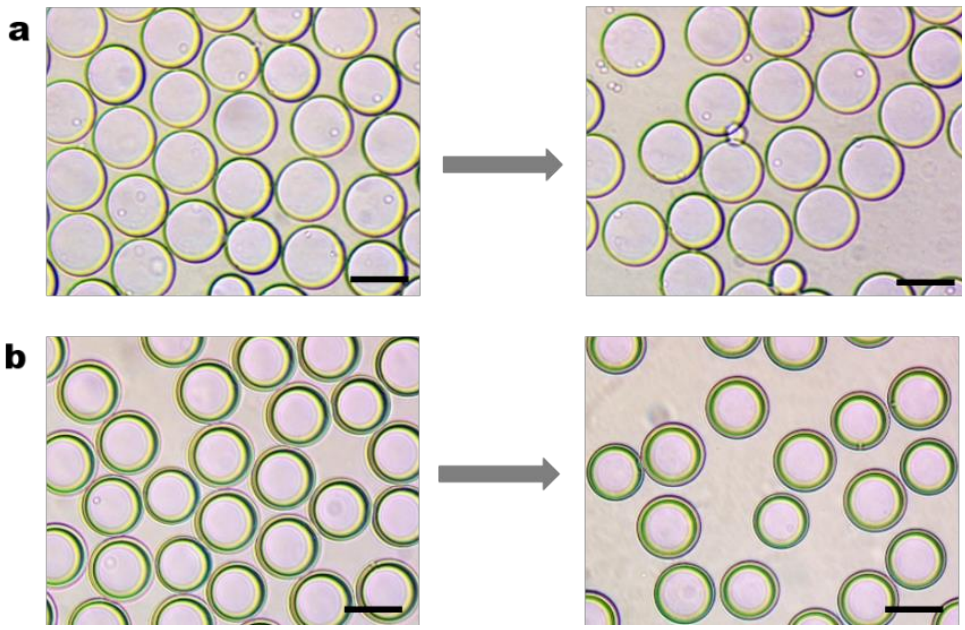

FIGURE 2.44: Control studies for Amine-P2 assembly. a) 0.2 wt% Zonyl and 5 mM TEA12 stabilized emulsions initial perfect Janus morphology with no morphology changes observed after 30 min with addition of Acetamide-P2 assembly to TEA12/Zonyl stabilized double emulsions; b) 0.2 wt% Zonyl and 1 mM CTAB stabilized emulsions displayed no change in morphology after 60 min with the addition of Amine-P2 assemblies. Scale bar = 50 µm

2.4.3. CASCADE NUCLEOPHILE STUDIES

SINGLE EMULSION STUDIES

HMDA equivalence study in no flow setup

Lower equivalents of HMDA with TEA12 were studied to determine if response to PAP-HMDA is equivalent to the amount of HDMA released from PAP-HMDA. It has been reported previously that ~20% of HMDA is released from the PAP vesicles after 25 minutes of irradiation and this amounts to ~0.05 equiv. HMDA being released over the period of irradiation with respect to the surfactant. Single emulsions were prepared using the TEA12 surfactant and 20 μL of the droplets were injected into the glass chamber no flow setup using a micropipette. 10 μL of 0.025, 0.05, and 0.1 equiv. (0.125, 0.25 and 0.5 mM) HMDA were added to an open end of the chamber to test the effect at sub-stoichiometric amounts of the nucleophile. In all three cases, bursting was observed within 3 minutes of addition of HMDA. However, the rate of bursting was slower at lower amounts of HMDA. With 0.025 equiv., about 90% of droplets were intact after 15 minutes. As expected, there were fewer number of intact droplets (~ 70- 80%) after the introduction of 0.05 and 0.1 equiv. HMDA after the same period (Figure 2.45).

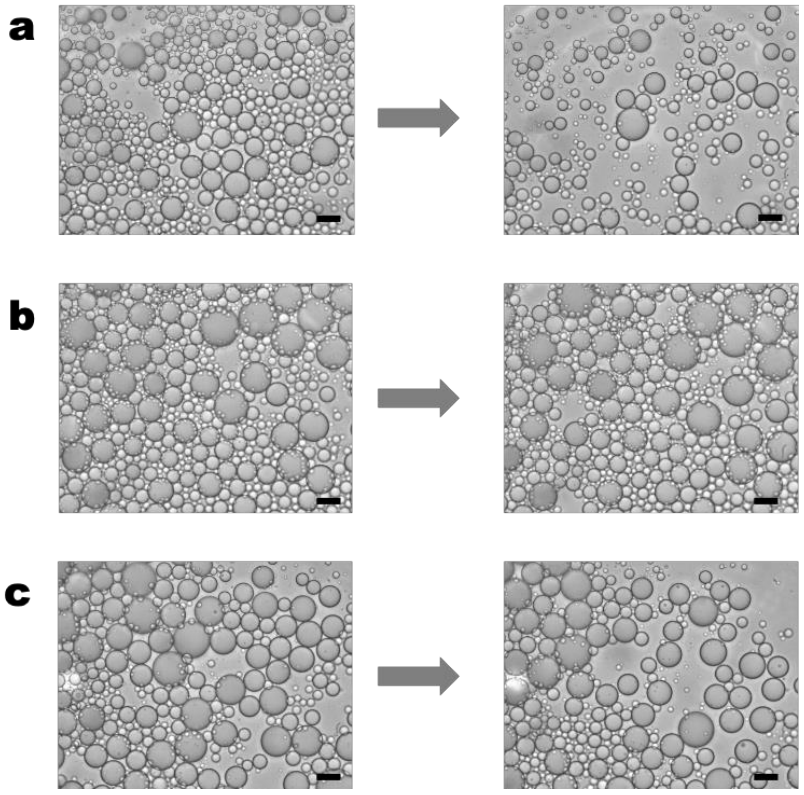

FIGURE 2.45: TEA12 HMDA study. Droplets before and after the addition of a) 0.1 equiv. b) 0.05 equiv. and c) 0.025 equiv. HMDA. Images were taken 7 minutes after the addition of the respective amounts of HMDA. Scale bar = 50 μm

PAP-HMDA studies and controls

HMDA encapsulated PAP polymerosomes were prepared using the protocol outlined in Methods. Single emulsions were prepared using the TEA12 surfactant and 20 μL of the droplets were injected into the glass chamber no flow setup using a micropipette. 10 μL of 4 mg/mL PAP-HMDA polymerosomes before and after UV treatment (365 nm) were introduced from one of the open ends of the chamber. Untreated PAP-HMDA triggered no response in the emulsion droplets, whereas UV-treated PAP-HMDA initiated bursting within 3 minutes of analyte introduction, as expected (Figure 2.46a and Figure 4c, respectively). Control experiments were performed using 1

mM CTAB emulsion droplets, where PAP- HMDA was introduced with and without UV treatment. In both cases, no changes were observed in the emulsion droplets after analyte addition (Figure 2.46b-c).

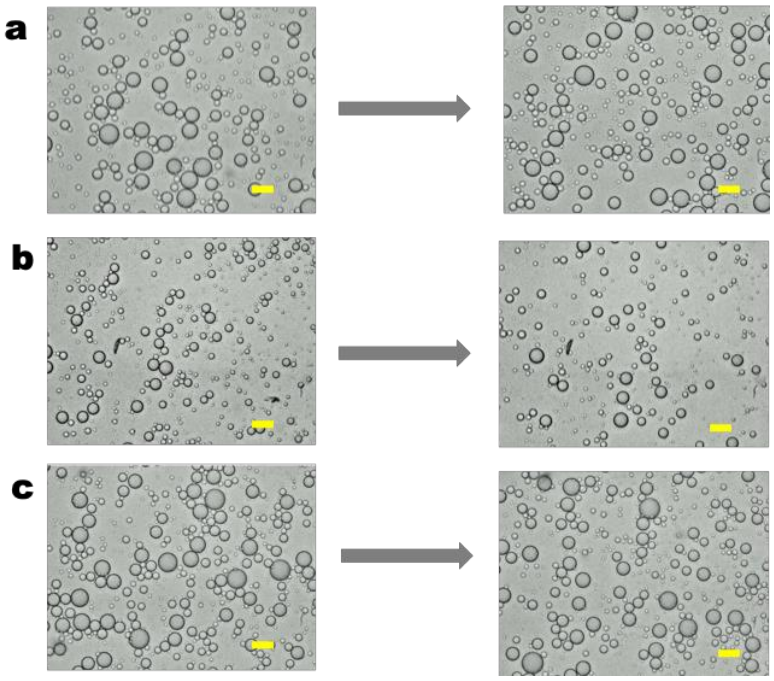

FIGURE 2.46: Control studies for PAP-HMDA addition. a) TEA12 droplets with UV untreated PAP-HMDA after 5 min; b) CTAB droplets with UV untreated PAP-HMDA after 5 min; c) CTAB droplets with UV treated PAP-HMDA after 5 min. d) DLS plots of PAP vesicles before and after encapsulation; e) Correlation coefficients of PAP vesicles before and after encapsulation. Scale bar = 50 μm

DOUBLE EMULSIONS

HMDA equivalence study in no flow setup

Studies were performed using the no-flow setup and general procedure with double emulsions stabilized by 0.2 wt% Zonyl and 5 mM TEA12. To the double emulsions, 0.025, 0.05, and 0.1 equiv. (0.125, 0.25, and 0.5 mM) HMDA were added. With the addition of 0.1 equiv. HMDA, full conversion from perfect Janus to HC/FC/W emulsions was observed within 2 min

and unlike the microfluidic array setup tests with 0.25-1.1 equiv., no bursting was observed (Fig. 2.47a to b). A clear morphology change was observed over 15 minutes with 0.05 equiv. HMDA (Figure 2.47a to c). A small morphology change was observed with addition of 0.025 equiv. HDMA over 15 min (Figure 2.47a to d).

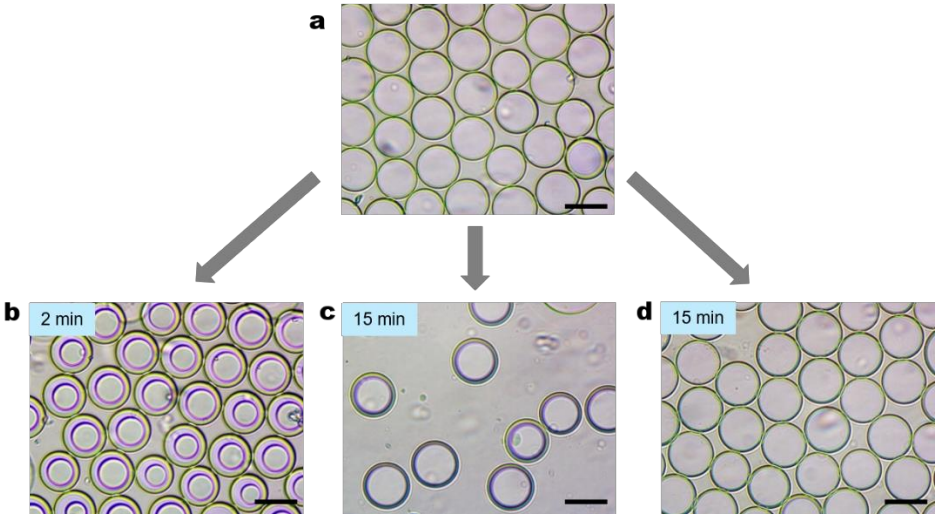

FIGURE 2.47: HMDA equivalence study in no flow setup. a) TEA12/Zonyl stabilized emulsions initial perfect Janus morphology; b) Morphology change after exposure to 0.1 equiv. HMDA over 2 min; c) morphology changes, but not full conversion to HC/FC/W, observed after exposure to 0.05 equiv. HMDA; d) Minimal morphology changes were observed after 15 min with the addition of 0.025 equiv. HMDA. Scale bar = 50 μm

PAP-HMDA studies and controls

Studies were performed using the no-flow setup and general procedure with double emulsions stabilized by 0.2 wt% Zonyl and 5 mM TEA12. For excitation of the PAP-HMDA, a 365 nm LED was used. 100 μL PAP-HMDA (4 mg/mL) was irradiated for 25 minutes to release

HMDA. The entire mixture was then transferred to the microscope chamber containing the double emulsion solution and the changes in morphology were recorded after 10 min (Figure 2.48a-b).

Control studies were then performed. First, the TEA12/Zonyl stabilized droplets were irradiated for 25 min in the absence of PAP-HMDA (Figure 48c). Second, 100 µL of the PAP-HMDA (4 mg/mL) were added without excitation (Figure S48d). No morphology changes were observed for either test. Further control studies were performed with 0.2 wt% Zonyl and 1 mM CTAB stabilized double emulsions. 200 µL of the HMDA-PAP solution (2 mg/mL) was irradiated for 25 min to release HMDA and the solution was then added to the double emulsions (Figure 2.48e). No changes in morphology from initial FC/HC/W were observed over 30 min.

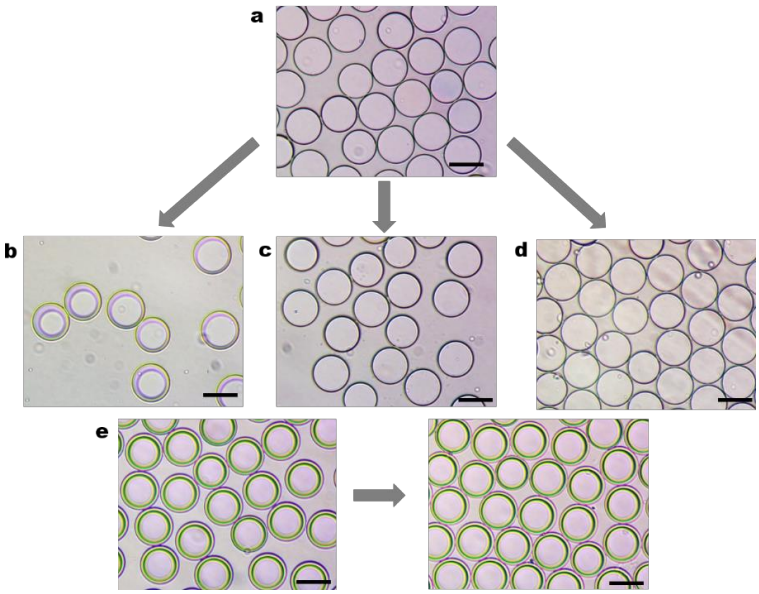

FIGURE 2.48: Control studies for PAP-HMDA addition. a) TEA12/Zonyl stabilized emulsions initial perfect Janus morphology; b) Morphology change after exposure to pre-released HMDA from PAP; c) No morphology changes were observed after droplets (in the absence of PAP-HMDA) were irradiated for 25 min; d) No morphology changes were observed after 30 min with the addition of HMDA-PAP without excitation; e) No morphology changes were observed after pre-released HMDA from PAP was added to CTAB/Zonyl stabilized emulsions after 30 min. Scale bar = 50 µm

Next, *in situ* irradiation of PAP-HMDA was performed. As described, 100 µL of PAP-HMDA solution (4 mg/mL) was added to TEA/Zonyl stabilized emulsions and exposed to 365 nm UV-light *in situ*. The entire solution was irradiated for 5 min and morphology recorded (Figure 2.49). The system was then allowed to sit in ambient conditions for 5 min, but no additional morphology changes were observed. The system was then exposed to UV-light for an additional 5 min (10 min total) and process repeated. Morphology changes were observed after additional UV exposure, but no further changes were observed under ambient conditions.

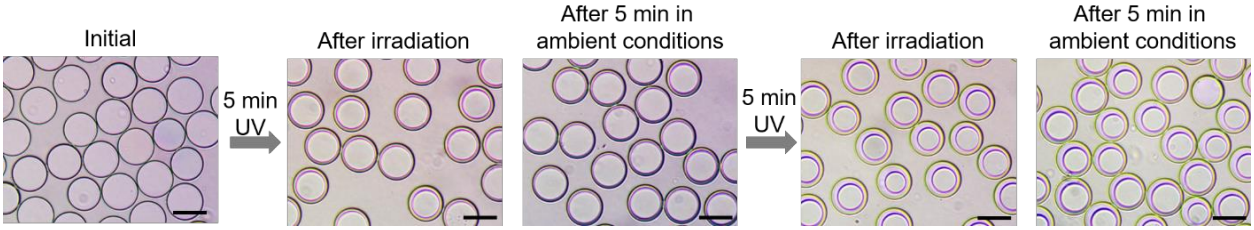

FIGURE 2.49: PAP-HMDA studies with *in situ* irradiation. Scale bar = 50 µm

2.4.4. KINETICS STUDIES

Study of EG_2-SH reaction with surfactants and product kinetic studies:

Kinetics studies were performed to test the rate of reaction of the TEA12, PYR12 and DMAP12 surfactants with EG2-SH as the nucleophile. The desired surfactant was dissolved in 500 µL acetone-*d6*, followed by the addition of 1.1, 0.5, or 0.1 equiv. EG2-SH (5.5, 2.5 or 0.5 mM for TEA12; 4.4, 2.0 or 0.4 mM for DMAP12 and PYR12). The mixture was then monitored immediately via 1H-NMR to study the kinetics of reaction (Figure 2.50-2.55). Analysis over 24 h shows that TEA12 displayed the fastest reaction kinetics followed by DMAP12. PYR12 was the slowest, with no product peak evolution even after 48 h. Appearance of $H_{b'}$, highlighted in each example, was compared to the disappearance of H_a to track reaction progress.

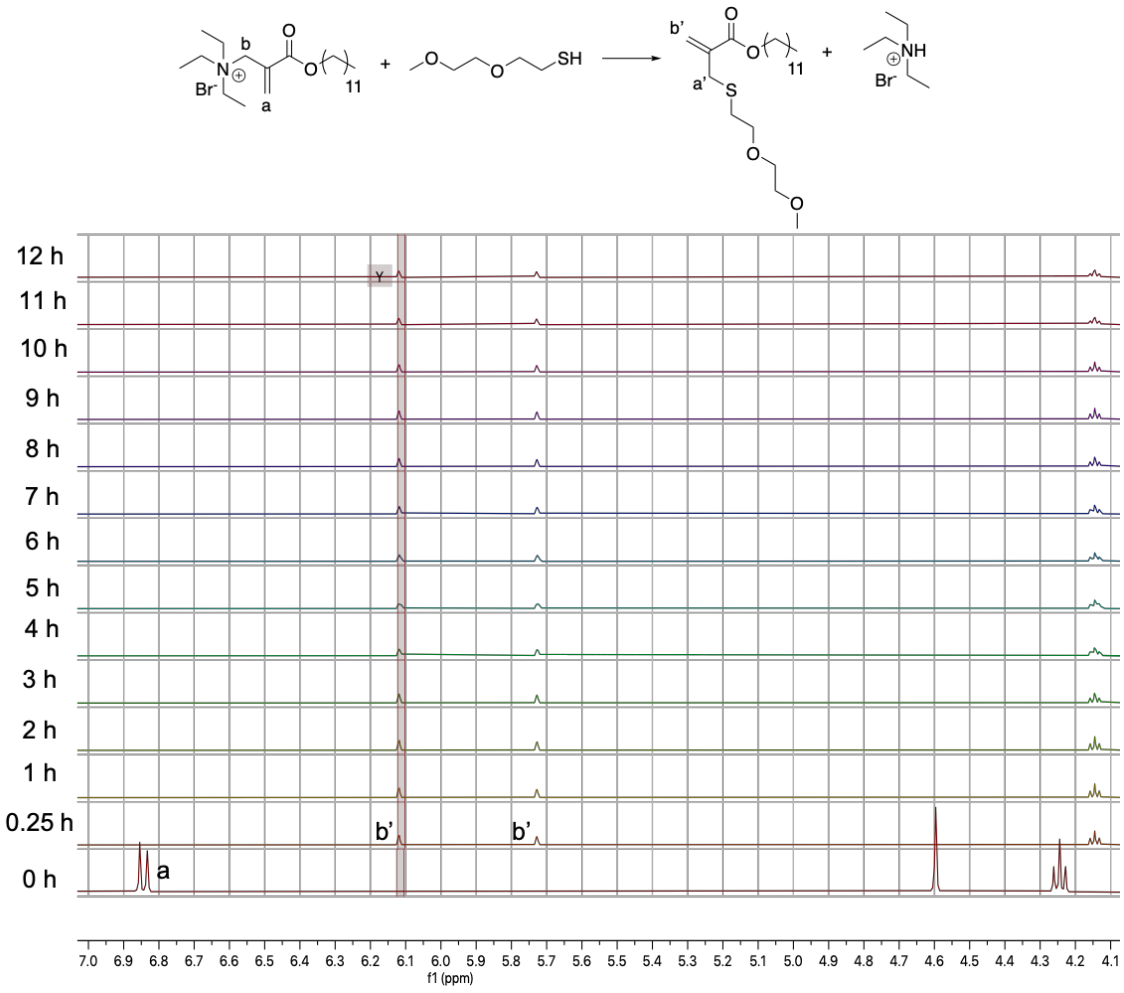

FIGURE 2.50: ^{1}H-NMR kinetics studies of TEA12 with 1.1 equiv. EG_2-SH.

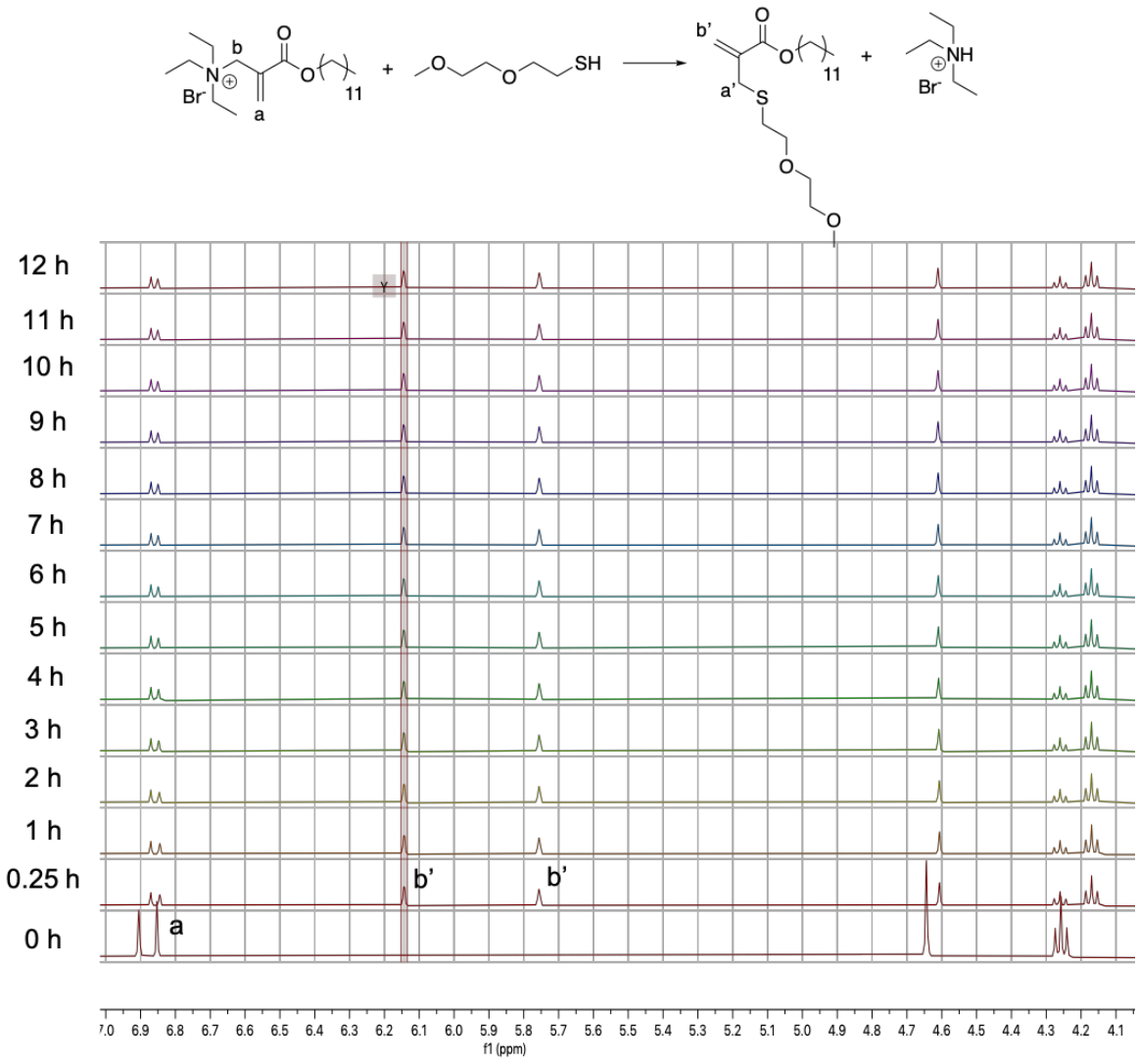

FIGURE 2.51: ^{1}H-NMR kinetics studies of TEA12 with 0.5 equiv. EG_2-SH.

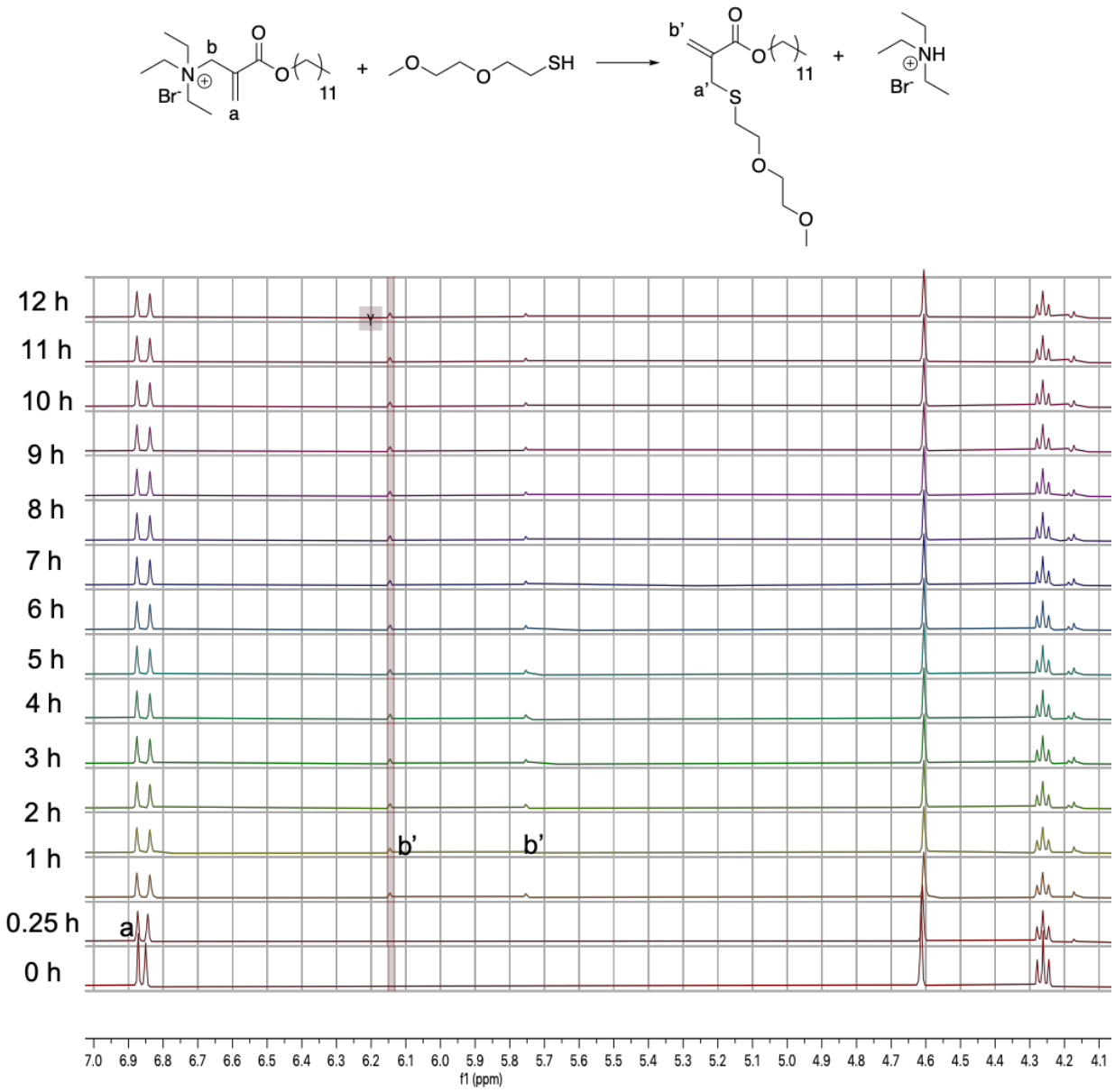

FIGURE 2.52: ^{1}H-NMR kinetics studies of TEA12 with 0.1 equiv. EG_2-SH.

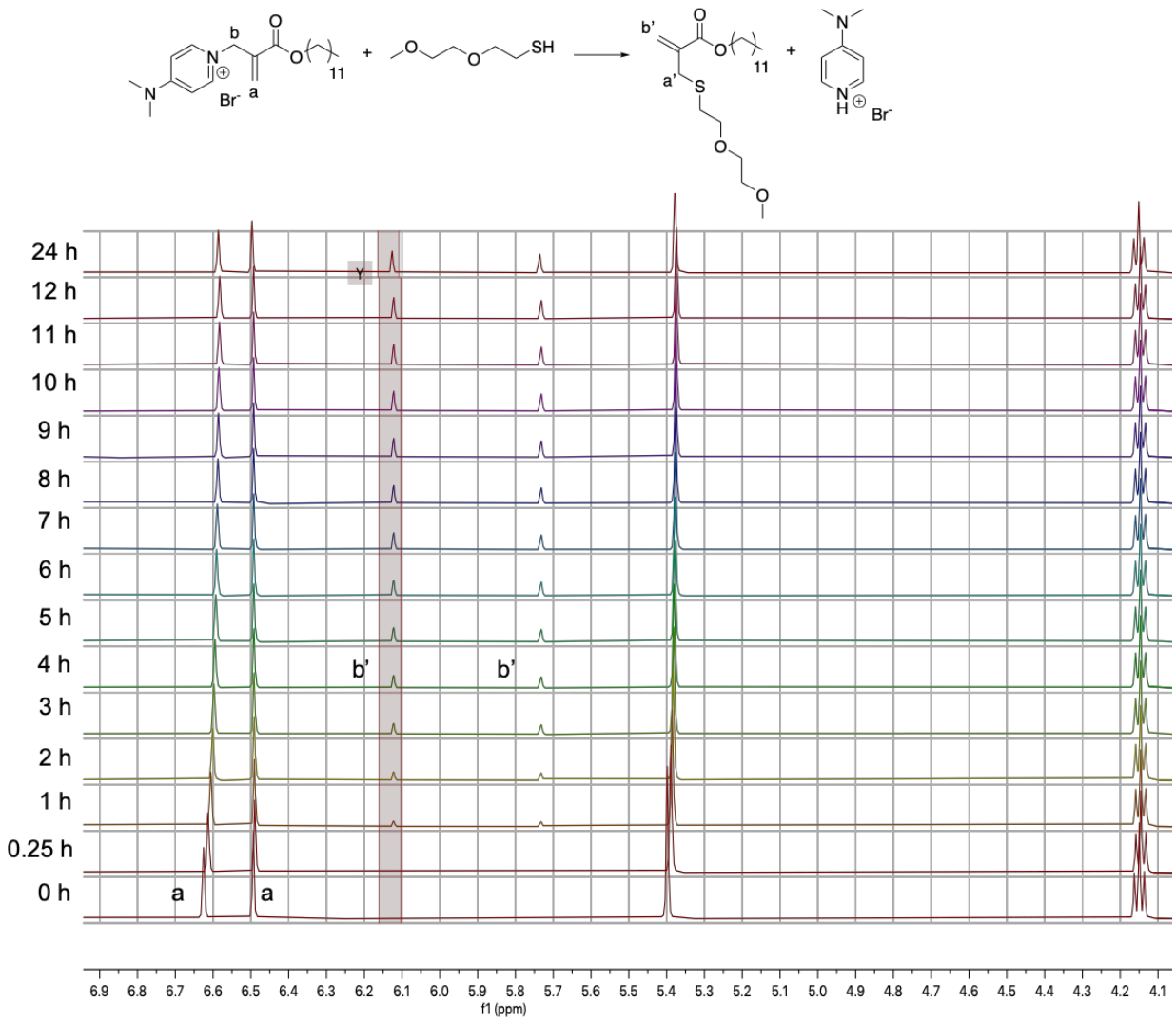

FIGURE 2.53: ^{1}H-NMR kinetics studies of DMAP12 with 1.1 equiv. EG_2-SH.

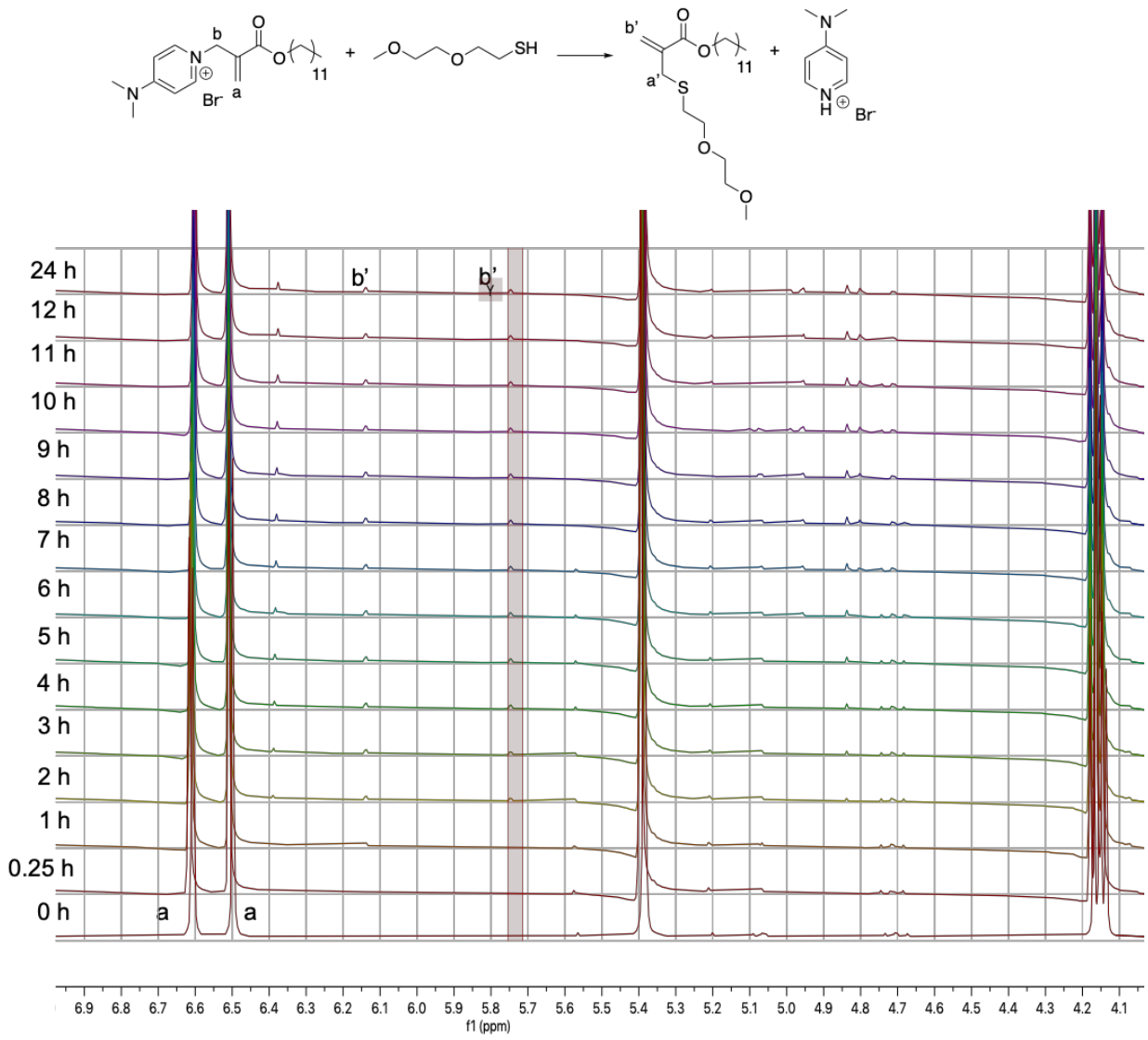

FIGURE 2.54: ^{1}H-NMR kinetics studies of DMAP12 with 0.5 equiv. EG_2-SH.

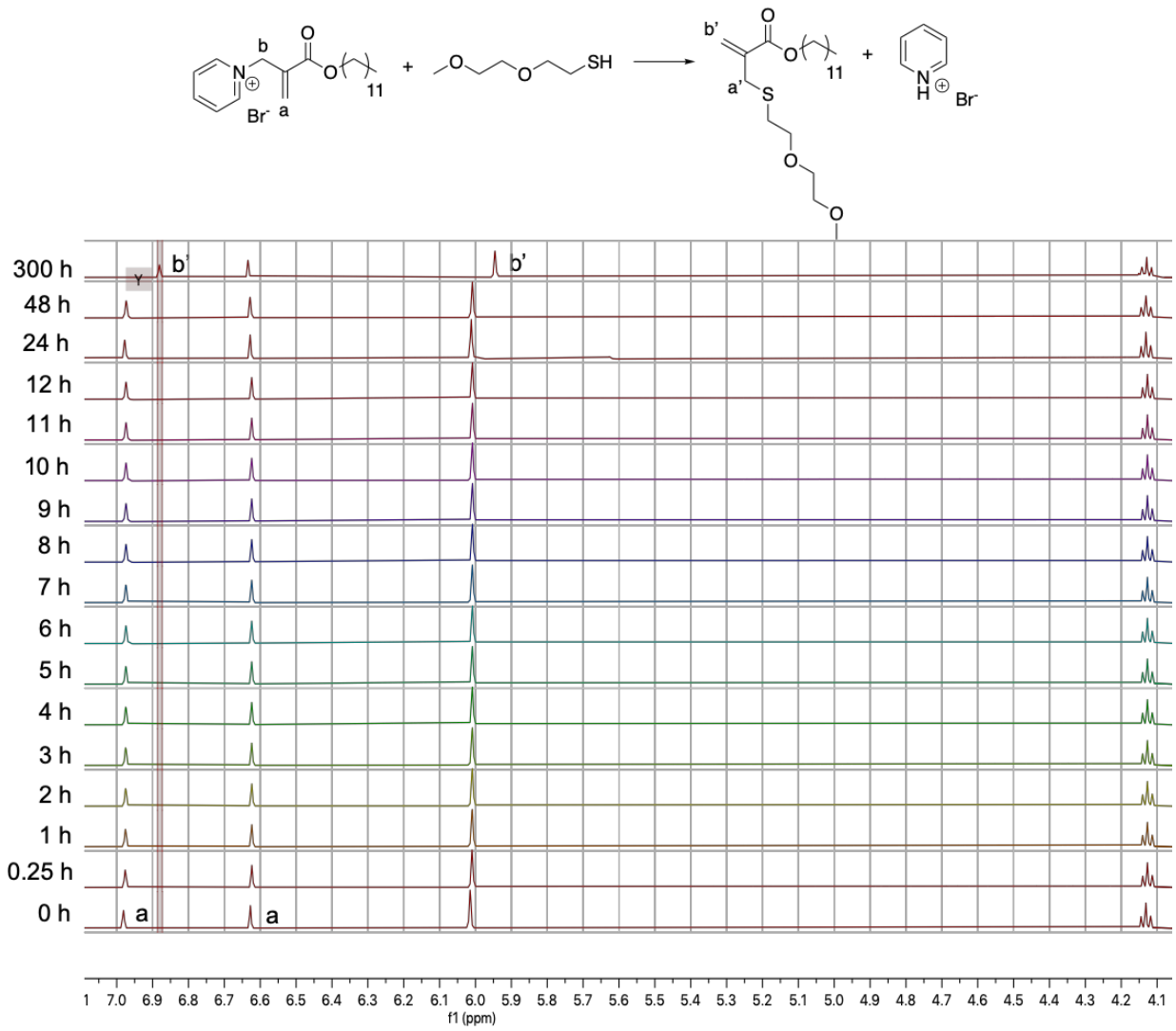

FIGURE 2.55: ^{1}H-NMR kinetics studies of PYR12 with 1.1 equiv. EG_2-SH.

2.4.5. PARTITIONING STUDIES:

Partitioning studies of the product in water vs hexanes were additionally performed to test the fate of the reacted small molecule, its partitioning from water to hexane was tested. 20 mg (56.4 mmol) TEA12 surfactant was dissolved in 500 µL water, followed by the addition of 1.1 equiv. (62.1 mmol) EG2-SH. The product formed as an insoluble precipitate, which was isolated, characterized and confirmed via ^{1}H NMR (Figure 2.56). To this mixture in water, 500 µL of hexane

was added and it was observed that the precipitate partitioned into the hexane layer after shaking (Figure 2.57). Due to volume difference in the emulsion systems, wherein the hexane phase is a fraction of the water, it is likely not all the product is dissolved in the hexane phase; however, this shows the preference of the product to partition into the hexane phase.

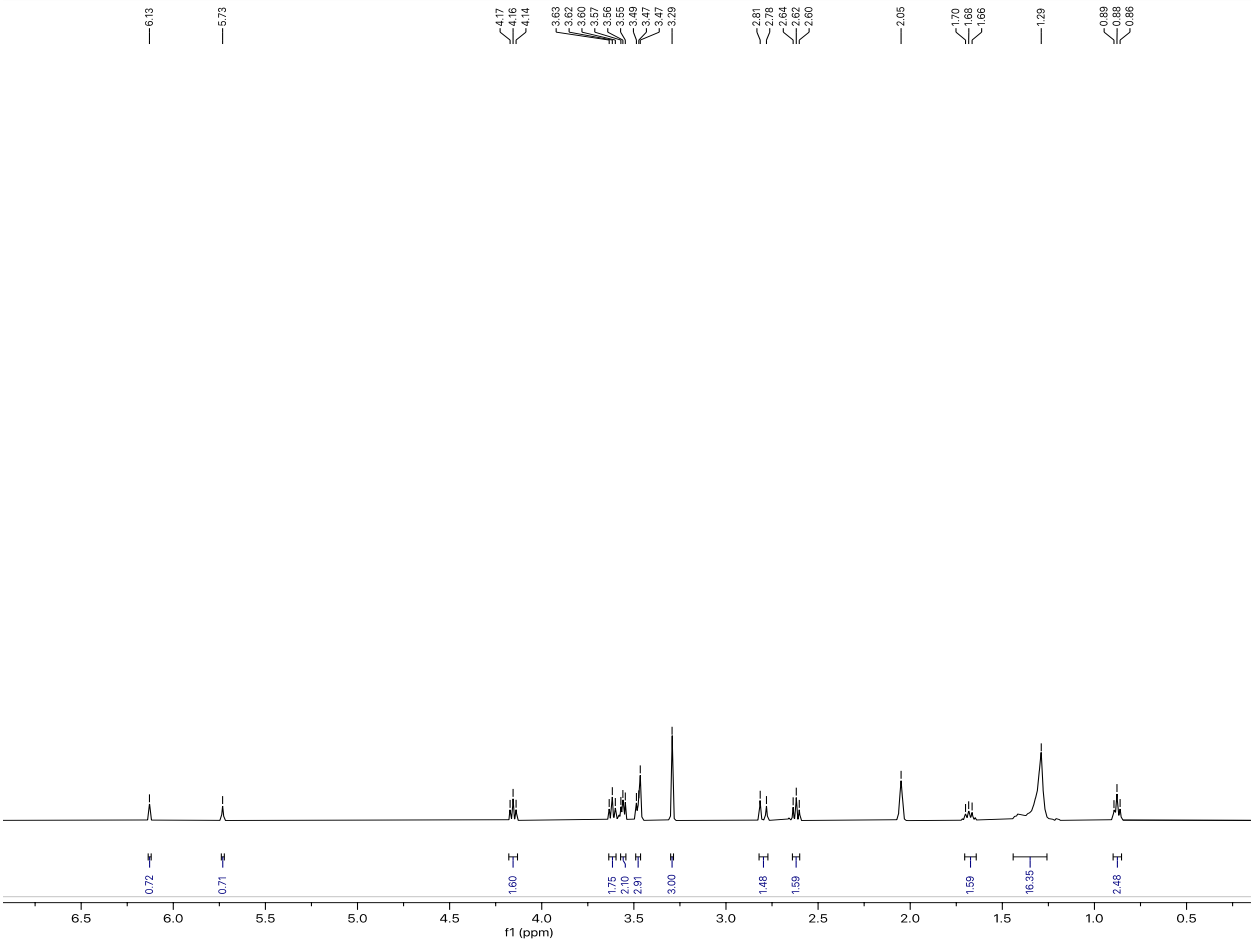

FIGURE 2.56: ^{1}H-NMR of the isolated product

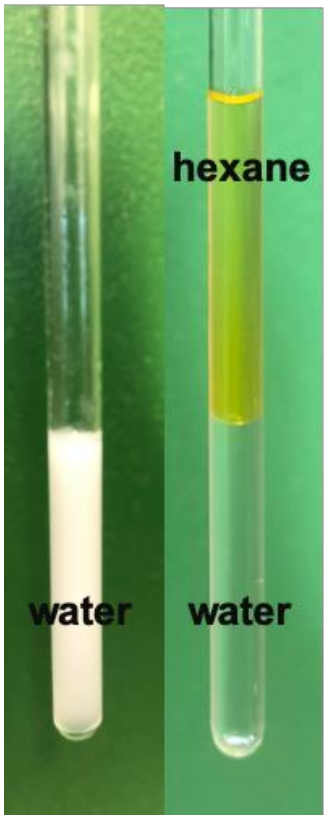

Figure 2.57: Partitioning studies showing the reacted product formed an insoluble product in water, which partitioned into the hexane after shaking.

2.5 CONCLUSIONS

In this work, we have designed covalently triggerable surfactants, based on TMAc chemistry, that respond to specific nucleophilic stimuli and utilized them as interfacial stabilizers of single and double emulsions. We have shown that through the rational design of the surfactant molecules, specific nucleophile triggers reduce surfactant strength through the loss of the charged hydrophilic head group, thus destabilizing HC/W interfaces. The destabilization of HC/W interfaces causes single and double emulsions to burst and undergo morphological changes, respectively, providing a macroscopic response to microscale reactivity. Importantly, the structure of the surfactant molecules imparted tunable kinetic control on the emulsion response through

changes in the leaving group ability. Further, we demonstrated that both small molecule and nanoassembly nucleophiles can be utilized as stimuli. Finally, by combining TMAc-functionalized emulsions with an orthogonally responsive modality, a cascade response was observed, wherein a light-induced release of a nucleophile guest from a nanoassembly resulted in emulsion response. Overall, a formal Michael-type SN2′ reaction has been conveniently utilized to create programmable emulsion systems with significant control. Such emulsion programming capability has implications in sensing, delivery, adhesion, and self-healing applications.

2.6 REFERENCES

1. Bhaskar, S.; Tian, F.; Stoeger, T.; Kreyling, W.; de la Fuente, J. M.; Grazu, V.; Borm, P.; Estrada, G.; Ntziachristos, V.; Razansky, D. Multifunctional Nanocarriers for Diagnostics, Drug Delivery and Targeted Treatment Across Blood-Barrier: Perspectives on Tracking and Neuroimaging. *Part. Fibre Toxicol.,* **2010,** *7,* 1-25.
2. Stasiuk, E. N. B.; Schramm, L. L. The Temperature Dependence of the Critical Micelle Concentrations of Foam-Forming Surfactants. *J. Colloid Interface Sci.,* **1996**, *178*, 324−333.
3. Noudeh, G. D.; Housaindokht, M.; Bazzaz, B. S. F. The Effect of Temperature on Thermodynamic Paramters of Micellization of Some Surfactants. J. Appl. Sci., **2017**, *7*, 42−52.
4. Thongngam, M.; McClements, D. J. Influence of pH, Ionic Strength, and Temperature on Self-Association and Interactions of Sodium Dodecyl Sulfate in the Absence and Presence of Chitosan. Langmuir, **2005**, *21*, 79−86.
5. Israelachvili, J. N. Thermodynamic Principles of Self-Assembly. In Intermolecular and Surface Forces, 3rd; Elsevier Inc.: Burlington, MA, 2011; pp 503−534.

6. Brown, P.; Butts, C. P.; Eastoe, J. Stimuli-Responsive Surfactants. Soft Matter, **2013**, *9,* 2365−2374.

7. Tehranibagha, A.; Holmberg, K. Cleavable Surfactants. Curr. Opin. Colloid Interface Sci., **2007**, *12*, 81−91.

8. Wang, Y.; Xu, H.; Zhang, X. Tuning the Amphiphilicity of Building Blocks: Controlled Self-Assembly and Disassembly for Functional Supramolecular Materials. Adv. Mater., **2009**, *21*, 2849− 2864.

9. Tang, J.; Quinlan, P. J.; Tam, K. C. Stimuli-Responsive Pickering Emulsions: Recent Advances and Potential Applications. Soft Matter, **2015**, *11*, 3512−3529.

10. Liang, C.; Harjani, J. R.; Robert, T.; Rogel, E.; Kuehne, D.; Ovalles, C.; Sampath, V.; Jessop, P. G. Use of CO 2 -Triggered Switchable Surfactants for the Stabilization of Oil-in-Water Emulsions. Energy Fuels, **2012**, *26*, 488−494.

11. Ceschia, E.; Harjani, J. R.; Liang, C.; Ghoshouni, Z.; Andrea, T.; Brown, R. S.; Jessop, P. G. Switchable Anionic Surfactants for the Remediation of Oil-Contaminated Sand by Soil Washing. RSC Adv., **2014**, *4*, 4638−4645.

12. Viricel, W.; Mbarek, A.; Leblond, J. Switchable Lipids: Conformational Change for Fast pH-Triggered Cytoplasmic Delivery. Angew. Chem., Int. Ed. **2015**, *54*, 12743−12747.

13. Asokan, A.; Cho, M. J. Cytosolic Delivery of Macromolecules. 3. Synthesis and Characterization of Acid-Sensitive Bis-Detergents. *Bioconjugate Chem*., **2004**, *15*, 1166−1173.

14. Stjerndahl, M.; van Ginkel, C. G.; Holmberg, K. Hydrolysis and Biodegradation Studies of Surface-Active Esters. *J. Surfactants Deterg*., **2003**, *6*, 319−324.

15. Zeininger, L.; Nagelberg, S.; Harvey, K. S.; Savagatrup, S.; Herbert, M. B.; Yoshinaga, K.; Capobianco, J. A.; Kolle, M.; Swager, T. M. Rapid Detection of Salmonella enterica via Directional Emission from Carbohydrate-Functionalized Dynamic Double Emulsions. *ACS Cent. Sci.* **2019**, *5*, 789−795.

16. Zarzar, L. D.; Kalow, J. A.; He, X.; Walish, J. J.; Swager, T. M. Optical Visualization and Quantification of Enzyme Activity Using Dynamic Droplet Lenses. *Proc. Natl. Acad. Sci. U.S.A.*, **2017**, *114*, 3821−3825.

17. Zarzar, L. D.; Sresht, V.; Sletten, E. M.; Kalow, J. A.; Blankschtein, D.; Swager, T. M. Dynamically Reconfigurable Complex Emulsions via Tunable Interfacial Tensions. *Nature***,** **2015**, *518*, 520− 524.

18. Sakai, K.; Imaizumi, Y.; Oguchi, T.; Sakai, H.; Abe, M. Adsorption Characteristics of Spiropyran-Modified Cationic Surfac- tants at the Silica/Aqueous Solution Interface. *Langmuir*, **2010**, *26*, 9283−9288.

19. Liu, Y.; Jessop, P. G.; Cunningham, M.; Eckert, C. A.; Liotta, C. L. Switchable Surfactants. *Science*, **2006**, *313*, 958−960.

20. McElhanon, J. R.; Zifer, T.; Kline, S. R.; Wheeler, D. R.; Loy, D. A.; Jamison, G. M.; Long, T. M.; Rahimian, K.; Simmons, B. A. Thermally Cleavable Surfactants Based on Furan−Maleimide Diels− Alder Adducts. *Langmuir*, **2005**, *21*, 3259−3266.

21. Minkenberg, C. B.; Florusse, L.; Eelkema, R.; Koper, G. J. M.; van Esch, J. H. Triggered Self-Assembly of Simple Dynamic Covalent Surfactants. *J. Am. Chem. Soc*., **2009**, *131*, 11274−11275.

22. Zentner, C. A.; Anson, F.; Thayumanavan, S.; Swager, T. M. Dynamic Imine Chemistry and Complex Double Emulsion Interfaces. *J. Am. Chem. Soc*. **2019**, *141*, 18048−18055.

23. Jaeger, D. A.; Li, B.; Clark, T. Cleavable Double-Chain Surfactants with One Cationic and One Anionic Head Group that Form Vesicles. *Langmuir,* **1996**, *12*, 4314−4316.

24. Lundberg, D.; Holmberg, K. Nuclear Magnetic Resonance Studies on Hydrolysis Kinetics and Micellar Growth in Solution of Surface-Active Betaine Esters. *J. Surfactants Deterg*., **2004**, *7*, 239−246.

25. Zhuang, J.; Zhao, B.; Meng, X.; Schiffman, J. D.; Perry, S. L.; Vachet, R. W.; Thayumanavan, S. A Programmable Chemical Switch Based on Triggerable Michael Acceptors. *Chem. Sci.*, **2020**, *11*, 2103− 2111.

26. Kippo, T.; Fukuyama, T.; Ryu, I. Regioselective Radical Bromoallylation of Allenes Leading to 2-bromo-substituted 1,5-dienes. *Org. Lett.,* **2011,** *13,* 3864-3867.

27. Snow, A. W.; Foos, E. E. Conversion of Alcohols to Thiols via Tisylate Intermediates. *Synthesis* **2003,** *4,* 509-512**.**

28. Molla, M. R.; Rangadurai, P.; Antony, L.; Swaminathan, S.; de Pablo, J. J.; Thayumanavan, S. Dynamic Actuation of Glassy Polymersomes Through Isomerization of a Single Azobenzene Unit at the Block Copolymer Interface. *Nat. Chem*., **2018**, *10*, 659−666.

29. Levario, T. J.; Zhan, M.; Lim, B.; Shvartsman, S. Y.; Lu, H. Microfluidic Trap Array for Massively Parallel Imaging of Drosophila Embryos. *Nat. Protoc*., **2013**, *8*, 721−736.

30. Nagelberg, S.; Zarzar, L. D.; Nicolas, N.; Subramanian, K.; Kalow, J. A.; Sresht, V.; Blankschtein, D.; Barbastathis, G.; Kreysing, M.; Swager, T. M.; Kolle, M. Reconfigurable and Responsive Droplet- based Compound Micro-lenses. *Nat. Commun*., **2017**, *8*, No. 14673.

CHAPTER 3

3.1 INTRODUCTION

Lipid bio-membranes due to their thin, flexible, and fluid-like properties, allow shape reorganization when it encounters complementary proteins, viruses, or synthetic particles.[1] Most interactions on a cell surface are based on specific receptor-mediated ligand interactions; an important mechanism by which biomolecules and particles can enter and leave an animal cell.[2] This mechanism is advantageous since it can be leveraged in nanomedicine to develop nanoparticles that display complementary surface ligands to selectively adhere to cell receptors, increasing interaction specificity and uptake.[3-5] However, with the advent of nanomedicine, which makes use of nonspecific and specific interactions for drug delivery, there have been growing concerns associated with nanoparticle cytotoxicity as a result of membrane interaction, [6-10]. Biological systems are inherently complex, and to understand more about the interaction process, disentangling the physicochemical process from biological complexities becomes necessary for rationalization. Computational models that use coarse-graining and multi-scale simulations have provided useful clues; however, the complexity of the cellular membrane poses several hurdles for theoretical routes.[10-12] Synthetic lipid membrane platforms such as giant unilamellar vesicles (GUVs) are a simplified alternative that can be utilized as a repeatable and robust experimental model for this purpose.

Mechanisms by which nanoparticles interact with the cell membrane have been of much interest. It is generally agreed upon that the local geometry, ligand density, size, and rigidity of a nanoparticle determine the outcome after interaction with the cellular bio-membrane.[11-13] From the membrane point of view, the interaction process would also depend on the bending elasticity of the membrane and the geometry of the curved membrane.[10] Although synthetic lipid platforms have been previously used to study the effect of polymers and nanoparticles on membrane

morphology, adhesion, and rupture,[12-14] most of these experimental and theoretical studies focus on the impact of non-specific interactions such as electrostatics in inducing changes to membrane morphology.[9,15-21] Results from these studies, however, cannot be fully extended to systems utilizing specific receptor-ligand interactions. Variations in solvation/desolvation contributions, entropic costs, and overall size scale of interaction[22] do not permit this, and studies that seek to fundamentally understand the role of specific receptor-ligand binding in nanoparticle-membrane interactions are rare. As a result, it becomes important that suitable synthetic models capable of mimicking the natural binding event between receptors and ligands displayed on nanoparticles be developed. With synthetic GUV platforms, experimental conditions can be simplified, and it would be possible to retrieve information about the physical rules that regulate the behavior of membranes during this process.

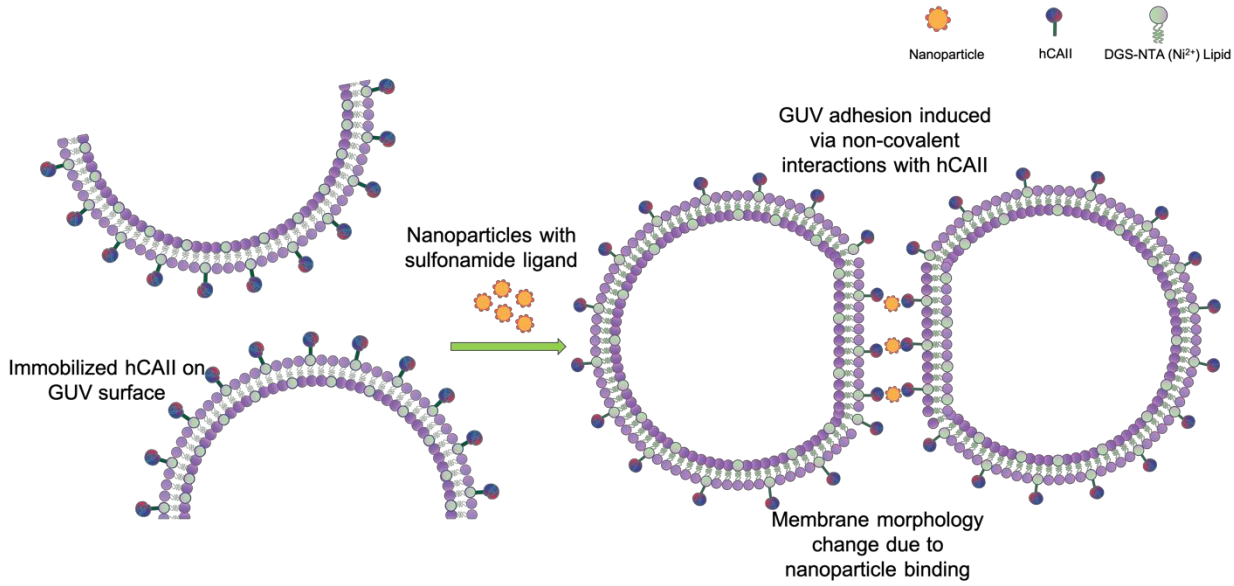

FIGURE 3.1: Schematic showing nanoparticle-induced GUV adhesion via non-covalent binding with immobilized hCAII on GUV surface

In this work, we adopt a strategy to explore specific receptor-mediated nanoparticle binding in GUVs by utilizing hCAII-benzenesulfonamide as the model receptor-ligand (R-L) pair (Figure 3.1). We immobilized hCAII onto the surface of GUVs as a receptor-decorated cell mimic to evaluate the effect of benzenesulfonamide decorated nanoparticles through membrane morphology transformations. These interfacial changes and associated systemic energies were found to be dependent on nanoparticle size, R and L surface densities, individual concentrations of R and L, and finally, overall R:L concentration ratios.

3.2 EXPERIMENTAL SECTION

3.2.1 MATERIALS

All reagents were obtained from commercial sources and used as received without further purification. 18:1 DOPC (1,2-dioleoyl-sn-glycero-3-phosphocholine), cholesterol, 18:1 DGS-NTA (Ni) (1,2-dioleoyl-sn-glycero-3-[(N-(5-amino-1-carboxypentyl)iminodiacetic acid)succinyl] (nickel salt), 18:1 NBD-PE (1,2-dioleoyl-sn-glycero-3-phosphoethanolamine-N-(7-nitro-2-1,3-benzoxadiazol-4-yl) (ammonium salt)) and 18:1 Rhod-PE (1,2-dioleoyl-sn-glycero-3-phosphoethanolamine-N-(lissamine rhodamine B sulfonyl) (ammonium salt)) lipids were purchased from Avanti Polar Lipids, Inc. Tetraethyl orthosilicate, 3-aminoproyltriethoxysilane, 4-(2-Aminoethyl)benzenesulfonamide, N,N'-dicyclohexylcarbodiimide (DCC), rhodamine-tagged dextran (70 kDa), FITC-tagged dextran (70 kDa), silica nanoparticles were purchased from Sigma-Aldrich. Sucrose, tetrahydrofuran (THF), toluene, ammonium hydroxide, and dimethylformamide (DMF) were obtained from Fisher Scientific. Succinic anhydride was obtained from Acros Organics. 190 proof Ethanol was obtained from Pharmco. 4-dimethylaminopyridine was obtained

from Chem-Impex International. Dansylamide (DNSA) was purchased from Aldrich Chemical Company. Perfusion chambers were purchased from Grace Biolabs.

3.2.2 INSTRUMENTAL ANALYSIS

Dynamic light scattering (DLS) measurements were performed on a Malvern Nanozetasizer-ZS operating at 633 nm. Absorbance measurements were performed on a Perkin-Elmer Lambda 35 UV-Visible spectrometer. Fluorescence measurements were performed using a PerkinElmer LS 55 spectrometer. Small volume (~200 µL) absorbance and fluorescence measurements were performed on a Molecular Devices multi-mode plate reader. All optical images were captured using NIS-Elements AR software on a Nikon Ti2-E spinning disk confocal microscope.

3.2.3 METHODS

a. SURFACE MODIFICATION OF SILICA NANOPARTICLES

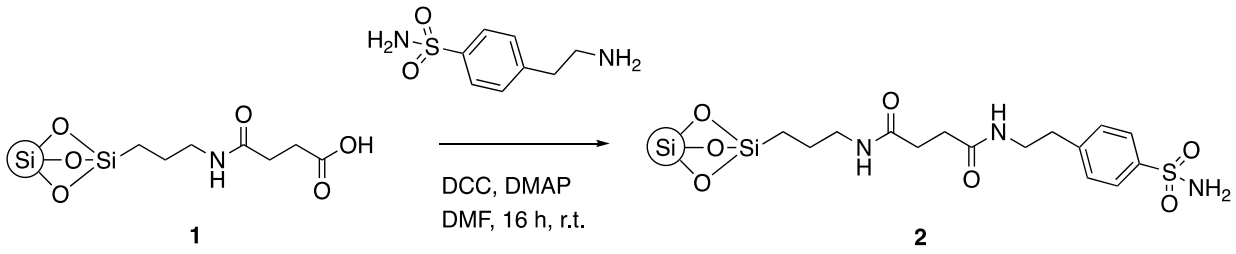

SCHEME 3.1: Surface modification of silica nanoparticles with benzenesulfonamide

Synthesis of **2**: 20 nm, 200 nm, 300 nm, 420 nm silica nanoparticles were surface-functionalized with succinic anhydride to obtain silica-COOH (**1)** using a procedure from literature.[23] To obtain

varying surface densities of sulfonamide on the silica particles, calculations in Table 3.1 and 3.2 were used. It is known that Stöber silica particles contain ~ 4-6 hydroxyl units per nm^2.[23-25]

Table 3.1: Moles, weights, and equivalents of different reagents used for sulfonamide surface density = 2.3 per nm^2

Silica-COOH (**1**)	DCC	DMAP	4-(2-Aminoethyl)benzenesulfonamide	DMF
420 nm (500 mg, 1.670 mmol)	12.2 mg, 59.4 µmol	3.61 mg, 29.7 µmol	11.2 mg, 59.4 µmol,	1.5 mL
300 nm (500 mg, 1.670 mmol)	17.1 mg, 82.9 µmol	5.02 mg, 41.5 µmol	16.6 mg, 82.9 µmol	1.5 mL
200 nm (500 mg, 1.670 mmol)	25.8 mg, 125 µmol	7.56 mg, 62.4 µmol	25.1 mg, 125 µmol	1.5 mL
20 nm (500 mg, 1.670 mmol)	257 mg, 1250 µmol	75.5 mg, 623 µmol	250 mg, 1250 µmol	1.5 mL

Table 3.2: Moles, weights, and equivalents of different reagents used for sulfonamide surface density = 0.27 per nm^2

Silica-COOH (**1**)	DCC	DMAP	4-(2-Aminoethyl)benzenesulfonamide	DMF
420 nm (500 mg, 1.670 mmol)	0.422 mg, 2.51 µmol	0.124 mg, 1.02 µmol	0.410 mg, 2.51 µmol	1.5 mL
300 nm (500 mg, 1.670 mmol)	0.591 mg, 2.92 µmol	0.176 mg, 1.45 µmol	0.581 mg, 2.92 µmol	1.5 mL
200 nm (500 mg, 1.670 mmol)	0.891 mg, 4.34 µmol	0.263 mg, 2.17 µmol	0.870 mg, 4.34 µmol	1.5 mL
20 nm (500 mg, 1.670 mmol)	8.91 mg, 43.2 µmol	2.62 mg, 21.6 µmol	8.64 mg, 43.2 µmol	1.5 mL

In our experiments, we first fixed this value to 10 hydroxyl units per nm^2 to estimate the weight of 4-(2-Aminoethyl)benzenesulfonamide required. An excess value of 10 hydroxyl units was used to ensure the complete functionalization of the silica surface. Based on this, the moles, weights, and equivalents of different reagents required for complete coverage for each silica sample are in Table 3.1. The number of sulfonamides per nm^2 was then determined using a quantification method

discussed in the next section to obtain the maximum number of sulfonamides per nm^2 that can be functionalized for all silica sizes. This value was found to be 2.3 per nm^2. Based on this, the weights of the reagents required for a lower sulfonamide surface density of 0.27 per nm^2 were calculated (Table 3.2). Using these calculations, **1** was weighed in a glass vial and dispersed in 1.3 mL DMF under sonication for 30 minutes. To this, corresponding amounts of DCC and DMAP were added to the vial and stirred for 10 minutes while purging under argon. This was followed by the addition of corresponding amounts of 4-(2-Aminoethyl)benzenesulfonamide (dissolved in a total of 200 µL DMF) under inert conditions . The reaction was left to continue overnight after which silica particles were centrifuged and washed with ethanol 3X, and lyophilized for binding studies.

b. SULFONAMIDE QUANTIFICATION ON SILICA NANOPARTICLES

The amount of sulfonamide functionalized on the silica particles was quantified using UV-Vis. A calibration plot of 4-(2-Aminoethyl)benzenesulfonamide was first made by measuring absorbances at 366 nm (Figure 3.2). The absorbance values of the various amounts of 4-(2-Aminoethyl)benzenesulfonamide used in Scheme 3.1 were then determined at 366 nm before and after reaction with the silica particles. The amount of sulfonamide that was conjugated to the surface of the silica particles was then determined by subtracting the absorbance values before and after completion of the reaction. Tables 3.3-3.4 show the sulfonamide surface density, sulfonamide molarity and total particle number that were calculated from absorbance values. Also note that the sulfonamide molarity can be varied by tuning the total particle number of sulfonamide nanoparticles in solution.

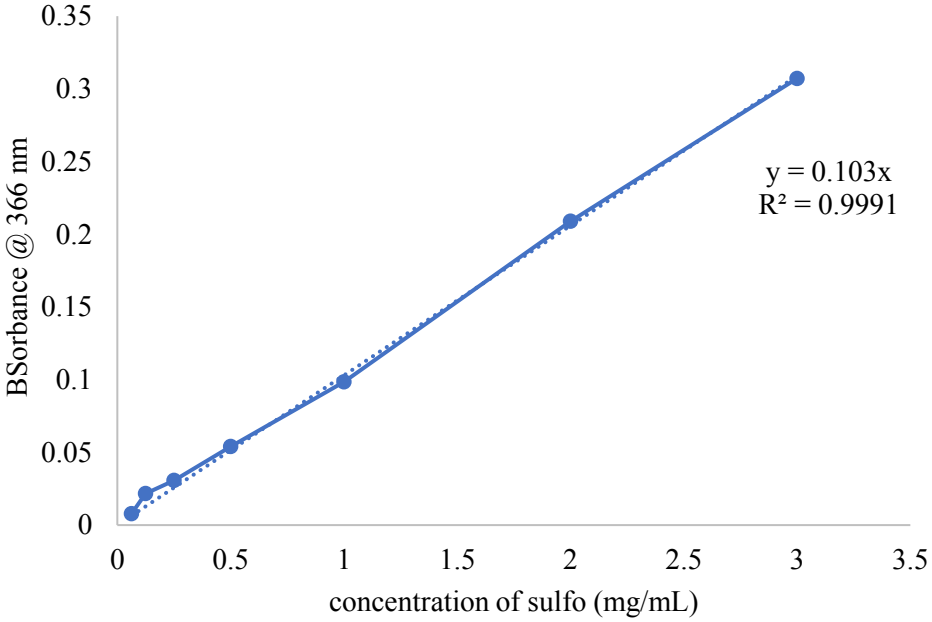

FIGURE 3.2: Calibration plot of 4-(2-Aminoethyl)benzenesulfonamide at 366 nm

Table 3.3: Sulfonamide molarity, surface density and corresponding particle number (at 10 mg/mL surface modified silica solution)

Size of silica nanoparticles (sulfonamide per nm^2 = 2.3)	#sulfonamide per nm^2	[sulfonamide] μM	total number of modified silica particles in 1 mL
400 nm	2.3	1.6	0.08E+10
		3	0.15E+10
		6	0.32E+10
		13	0.65E+10
300 nm	2.3	1.6	0.14E+10
		3	0.27E+10
		6	0.55E+10
		13	1.19E+10
200 nm	2.3	1.6	0.32E+10
		3	0.61E+10
		6	1.21E+10
		13	2.61E+10
20 nm	2.3	1.6	0.33E+12
		3	0.62E+12
		6	1.24E+12
		13	2.68E+12

Table 3.4: Sulfonamide molarity, surface density and corresponding particle number (at 10 mg/mL surface modified silica solution)

Size of silica nanoparticles (sulfonamide per nm^2 = 0.27)	#sulfonamide per nm^2	[sulfonamide] μM	total number of modified silica particles in 1 mL
400 nm	0.276	1.6	0.65E+10
		3	1.22E+10
		6	2.44E+10
		13	5.28E+10
300 nm	0.278	1.6	1.19E+10
		3	2.23E+10
		6	4.46E+10
		13	9.67E+10
200 nm	0.277	1.6	2.61E+10
		3	4.89E+10
		6	9.98E+10
		13	21.21E+10
20 nm	0.275	1.6	2.68E+12
		3	5.03E+12
		6	10.05E+12
		13	21.78E+12

c. HCAII EXPRESSION PROTOCOLS

Green fluorescent protein (GFP) and human carbonic anhydrase II (hCAII) enzyme were expressed using a procedure in literature.[26] Protein constructs for a 6-histidine motif at the N-terminus were made from the original plasmid via standard mutagenesis protocols.

d. HUMAN CARBONIC ANHYDRASE (HCAII) IMMOBILIZATION ON GUVS

Table 3.5: Volumes of fluorescent GUVs and hCAII added for GUV immobilization

RG GUVs (Vol. added/ DGS-NTA(Ni^{2+}) nmol)	FG GUVs (Vol. added/DGS-NTA(Ni^{2+}) nmol)	Total [DGS-NTA(Ni^{2+})] μM	Vol. of hCAII added μL	hCAII nmol	[hCAII] (μM)/surface density (per nm^2)
5 μL RNG0/ -	5 μL FNG0/ -	-	-	-	-
5 μL RNG1/ 0.78	5 μL FNG1/ 0.78	1.56	3.95	1.56	1.56/9.1E-4
5 μL RNG2/ 1.56	5 μL FNG2/ 1.56	3.13	7.96	3.13	3.13/18.3E-4
5 μL RNG3/ 3.13	5 μL FNG3/ 3.13	6.25	15.92	6.25	6.25/37.5E-4
5 μL RNG4/ 6.25	5 μL FNG4/ 6.25	12.5	31.84	12.5	12.5/75E-4

hCAII enzyme containing a polyhistidine (6-histidine) tag at the N-terminus was expressed using the protocols outlined in the previous section. Tris-HCl buffer in the hCAII enzyme samples was then exchanged with 197 mOsm/L glucose solution via spin filtration using 3k MWCO filters. In separate Eppendorf tubes, 5 μL of RGN0-RGN4 GUVs and 5 μL of corresponding FGN0-FGN4 GUVs were then mixed. Assuming that there is a 1:1 coordination between the Ni^{2+} in DGS-NTA(Ni^{2+}) and the histidine tag in hCAII, appropriate volumes of 392.5 μM hCAII were calculated (3.95 – 31.84 μL; 1.56 – 12.5 nmol) and added to the Eppendorf tubes. The final GUV

mixtures contained 1.56, 3.13, 6.25, and 12.5 µM of immobilized hCAII, respectively when diluted to 1 mL (Table 3.5).

e. DNSA BINDING EXPERIMENT

To determine the binding affinity of sulfonamide human carbonic anhydrase II (hCAII) enzyme, a published literature procedure was followed.[27] The binding affinity of sulfonamide nanoparticles with carbonic anhydrase enzyme was estimated via a competitive binding assay with dansylamide (DNSA). The K_d of DNSA with carbonic anhydrase was calculated to be 1 µM, which is in close agreement with the value of 0.9 µM, reported by Nair et al.[28] The K_d of sulfonamide surface-modified silica nanoparticles were found to have a calculated value of 0.25 µM from competitive binding experiments with DNSA.

f. DLS PLOTS OF SURFACE MODIFIED SILICA NANOPARTICLES:

DLS experiments were performed by using 0.1 mg/mL solutions of surface modified silica nanoparticles to confirm size.

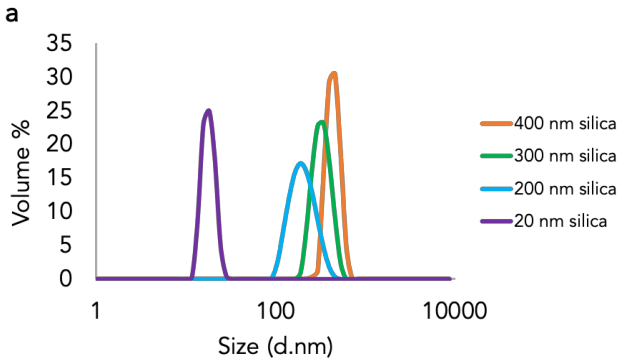

FIGURE 3.3: DLS plots of sulfonamide modified silica nanoparticles

g. HCAII ENZYME SURFACE COVERAGE DETERMINATION ON GUVS

Electroformed GUVs containing rhodamine and FITC- dextran were an average size of 20 μm. This was used to calculate the total number of DGS-NTA (Ni^{2+}) lipid in each GUV. Assuming an average GUV size of 20 μm, the total number of lipids on the outer leaflet of the GUV bilayer was theoretically calculated. From this, the number of DGS-NTA (Ni^{2+}) lipids was estimated based on the amounts doped into the DOPC-cholesterol mixture before electroformation. Assuming there is 1:1 binding between hCAII and DGS-NTA (Ni^{2+}), the number of hCAII enzymes per nm^2 on the GUV surface sample was then calculated (Table 3.6).

Table 3.6: Surface density of hCAII per nm^2 of GUV corresponding to the percent surface coverage of DGS-NTA(Ni^{2+})

% DGS-NTA (Ni^{2+}) doping	[hCAII] μM	# hCAII per nm^2
0.063%	1.56	9.1E-4
0.125%	3.13	18.3E-4
0.25%	6.25	37.5E-4
0.5%	12.5	75.0E-4

h. PREPARATION OF NON-FLUORESCENT GUVS VIA ELECTROFORMATION

Non-fluorescent GUVs were formed via electroformation, using a modified procedure in literature.[29] Briefly, DOPC (1,2-dioleoyl-sn-glycero-3-phosphocholine) (44.6 μL, 25 mg/mL, 1.5 μmol) and cholesterol (15 μL, 25 mg/mL, 1 μmol) were measured into 4 glass vials. The final ratio of DOPC:cholesterol was 3:2, with a total lipid concentration of 2.5 mM. 0.17, 0.33, 0.66, and 1.32 μL (1.56, 3.13, 6.25 and 12.5 nmol respectively) of 10 mg/mL DGS-NTA(Ni^{2+}) lipid were then added to glass vials containing the DOPC-cholesterol mixture. The final lipid formulations

had DGS-NTA(Ni^{2+}) at concentrations of 1.56, 3.13, 6.25, and 12.5 μM and were labeled as N1, N2, N3, N4 respectively. A control lipid mixture, N0, was also formulated with DOPC and cholesterol without DGS-NTA(Ni^{2+}). Each of the lipid formulations, N0-N4, was then smeared as a thin layer on a pair of ITO-coated slides and dried under vacuum for 90 minutes. Each pair of ITO slides were then positioned on either side of a Teflon spacer with the lipid-coated surfaces facing each other and secured to form an electroformation chamber. 197 mOsm/L sucrose solution prepared in distilled water was then injected into each chamber and filled completely. Electroformation was carried out at 50 °C at a sinusoidal applied frequency of 10 Hz and peak-to-peak voltage 2.4 V for 90 min. Post electroformation, the respective GUV solutions, GN0-GN4, were extracted from the chambers and placed into Eppendorf tubes. 197 mOsm/L glucose solution prepared in distilled water was then added to each tube and left undisturbed for 3 h to facilitate GUV sedimentation. The solutions were then gently centrifuged for complete sedimentation of formed GUVs. The supernatant was discarded, and the sedimented GUVs were recovered for further studies.

i. PREPARATION OF FLUORESCENT GUVS VIA ELECTROFORMATION

To prepare fluorescent GUVs, 0.5 mg/mL rhodamine- and FITC-tagged dextran solutions were dissolved in 180 mM sucrose solution. The osmolarities of these dextran solutions were finally adjusted to 197 mOsm/L. Electroformation protocols were then followed by using either 197 mOsm/L rhodamine or FITC-tagged dextran solutions instead of the non-fluorescent sucrose solution used in the previous section. This yielded fluorescent DGS-NTA(Ni^{2+}) containing GUVs encapsulating either rhodamine-dextran (RGN0-RGN4) or fluorescein-dextran (FGN0-FGN4) in

their lumen. To these GUV samples, 197 mOsm/L glucose was added to facilitate sedimentation prior to extraction for further studies.

j. HUMAN CARBONIC ANHYDRASE (HCAII) IMMOBILIZATION ON GUVS

hCAII protein containing a polyhistidine (6-histidine) tag at the N-terminus was expressed using the protocols outlined above. Tris-HCl buffer in the hCAII samples was then exchanged with 197 mOsm/L glucose solution via spin filtration using 3k MWCO filters. In separate Eppendorf tubes, 5 μL of RGN0-RGN4 GUVs and 5 μL of corresponding FGN0-FGN4 GUVs were then mixed. Assuming that there is a 1:1 coordination between the Ni^{2+} in DGS-NTA(Ni^{2+}) and the histidine tag in hCAII, appropriate volumes of 392.5 μM hCAII were calculated (3.95 – 31.84 μL; 1.56 – 12.5 nmol) and added to the Eppendorf tubes. After addition, the final GUV mixtures contained 1.56, 3.13, 6.25, and 12.5 μM of immobilized hCAII, respectively when diluted to 1 mL (Table 3.5). Experiments to confirm protein immobilization on the GUV surface were also performed using green fluorescent protein (GFP) (Control experiments, Figure 3.8).

k. PARTICLE-GUV INTERACTION STUDIES

10 mg of modified sulfonamide silica nanoparticles of various sizes were weighed, and 1 mL distilled water added to make a series of silica nanoparticle solutions of 10 mg/mL. After mixing hCAII and GUV (using values from Table 3.3), the corresponding volumes of the sulfonamide containing silica nanoparticle solutions in Tables 3.7-3.14 were added and incubated at 4°C. The incubated solutions were then diluted to 1 mL with 197 mOsm/L glucose and 20 μL injected into perfusion chambers to obtain optical microscopy images.

Table 3.7: Volumes of sulfonamide nanoparticles added to hCAII immobilized GUVs (420 nm, high sulfonamide surface density)				
[hCAII] μM	The volume of 420 nm particles added (sulfonamide surface density = 2.3 per nm^2) μL			
	1 μM sulfo	3 μM sulfo	6 μM sulfo	13 μM sulfo
1.56	5.95	11.9	23.8	47.6
3.13	5.95	11.9	23.8	47.6
6.25	5.95	11.9	23.8	47.6
12.5	5.95	11.9	23.8	47.6

Table 3.8: Volumes of sulfonamide nanoparticles added to hCAII immobilized GUVs (420 nm, low sulfonamide surface density)				
[hCAII] μM	Volume of 420 nm particles added (sulfonamide surface density = 0.27 per nm^2) μL			
	1 μM sulfo	3 μM sulfo	6 μM sulfo	13 μM sulfo
1.56	49.59	99.17	198.34	396.68
3.13	49.59	99.17	198.34	396.68
6.25	49.59	99.17	198.34	396.68
12.5	49.59	99.17	198.34	396.68

Table 3.9: Volumes of sulfonamide nanoparticles added to hCAII immobilized GUVs (300 nm, high sulfonamide surface density)				
[hCAII] μM	Volume of 300 nm particles added (sulfonamide per nm^2 = 2.3) μL			
	1 μM sulfo	3 μM sulfo	6 μM sulfo	13 μM sulfo
1.56	4.2	8.4	16.81	33.62
3.13	4.2	8.4	16.81	33.62
6.25	4.2	8.4	16.81	33.62
12.5	4.2	8.4	16.81	33.62

Table 3.10: Volumes of sulfonamide nanoparticles added to hCAII immobilized GUVs (300 nm, low sulfonamide surface density)				
[hCAII] μM	Volume of 300 nm particles added (sulfonamide surface density = 0.27 per nm^2) μL			
	1 μM sulfo	3 μM sulfo	6 μM sulfo	13 μM sulfo
1.56	32.35	64.69	129.39	258.79
3.13	32.35	64.69	129.39	258.79
6.25	32.35	64.69	129.39	258.79
12.5	32.35	64.69	129.39	258.79

Table 3.11: Volumes of sulfonamide nanoparticles added to hCAII immobilized GUVs (200 nm, high sulfonamide surface density)				
[hCAII] μM	Volume of 200 nm particles added (sulfonamide per nm^2 = 2.3) μL			
	1 μM sulfo	3 μM sulfo	6 μM sulfo	13 μM sulfo
1.56	2.81	5.61	11.22	22.44
3.13	2.81	5.61	11.22	22.44
6.25	2.81	5.61	11.22	22.44
12.5	2.81	5.61	11.22	22.44

Table 3.12: Volumes of sulfonamide nanoparticles added to hCAII immobilized GUVs (200 nm, low sulfonamide surface density)				
[hCAII] μM	Volume of 200 nm particles added (sulfonamide surface density = 0.27 per nm^2) μL			
	1 μM sulfo	3 μM sulfo	6 μM sulfo	13 μM sulfo
1.56	21.75	43.51	87.01	174.02
3.13	21.75	43.51	87.01	174.02
6.25	21.75	43.51	87.01	174.02
12.5	21.75	43.51	87.01	174.02

Table 3.13: Volumes of sulfonamide nanoparticles added to hCAII immobilized GUVs (20 nm, high sulfonamide surface density)				
[hCAII] μM	Volume of 20 nm particles added (sulfonamide per nm^2 = 2.3) μL			
	1 μM sulfo	3 μM sulfo	6 μM sulfo	13 μM sulfo
1.56	0.28	0.56	1.12	2.25
3.13	0.28	0.56	1.12	2.25
6.25	0.28	0.56	1.12	2.25
12.5	0.28	0.56	1.12	2.25

Table 3.14: Volumes of sulfonamide nanoparticles added to hCAII immobilized GUVs (20 nm, low sulfonamide surface density)				
[hCAII] μM	Volume of 20 nm particles added (sulfonamide surface density = 0.27 per nm^2) μL			
	1 μM sulfo	3 μM sulfo	6 μM sulfo	13 μM sulfo
1.56	2.29	4.58	9.17	18.34
3.13	2.29	4.58	9.17	18.34
6.25	2.29	4.58	9.17	18.34
12.5	2.29	4.58	9.17	18.34

3.3 RESULTS AND DISCUSSION:

To explore the interfacial GUV morphology effects induced by receptor-mediated nanoparticle binding, a model receptor was immobilized on the surface of the lipid membrane and subsequently allowed to interact with nanoparticles bearing complementary ligands. Human Carbonic Anhydrase II (hCAII) protein was chosen as the model receptor due to its relevance as a surface biomarker in several diseases and syndromes.[30] A library of sulfonamides, which are complementary ligands of hCAII, is also known.[30] For surface immobilization of hCAII, a known interaction between Ni^{2+} with polyhistidine amino-acid motifs was used to our advantage.[31] hCAII was expressed to contain a 6-histidine tag and then introduced to GUVs electroformed with Ni^{2+} to facilitate immobilization. In addition, the hCAII surface densities on the GUVs were tuned by varying the total amount of Ni^{2+} doped into the lipid membrane. Assuming that there is 1:1 binding between the Ni^{2+} and hCAII, the final receptor surface densities after immobilization were calculated to be 0, 9.1E-4, 18.3E-4, 37.5E-4, or 75E-4 per nm^2. These surface densities translate to a total concentration of 0, 1.56, 3.13, 6.25, and 12.5 μM hCAII, respectively. Next, a series of silica nanoparticles were surface modified to display benzenesulfonamide, a complementary ligand of hCAII (Scheme 3.1, Tables 3.1-3.2). Since the introduction of these nanoparticles facilitates non-covalent interfacial binding with the hCAII, changes in GUV membrane morphology are expected to occur post binding. In the following sections, we explore the effects of receptor/ligand surface density, nanoparticle size, and overall ratios of receptor and ligand concentrations on this receptor-mediated nanoparticle interaction process.

3.3.1 EFFECT OF HCAII SURFACE DENSITY ON NANOPARTICLE BINDING

The surface density of hCAII immobilized on the GUV surface were seen to influence the extent of nanoparticle binding and induces varying GUV membrane morphologies. To explore this, hCAII surface density on the GUVs was varied between 0 – 75E-4 per nm^2, whereas, the sulfonamide nanoparticles were held at a constant size of 420 nm, total sulfonamide concentration of 13 μM, and sulfonamide surface density of 2.3 per nm^2. As a result, any changes in the system would be a result of hCAII surface density variation. Due to the presence of multiple sulfonamide ligands on the nanoparticle surface, a single nanoparticle can establish contacts with multiple receptors at any given time. Due to this property of nanoparticle multivalency, inter-GUV adhesion was expected to occur. However, the extent of this adhesion would be dependent on hCAII surface density and will be reflected in the adhesion angles between adhered GUVs. This may be used as a qualitative estimate of the adhesion energy at the GUV interface. Figure 3.4 shows the morphology changes observed after introducing 420 nm sulfonamide particles (sulfonamide concentration of 13 μM and surface density of 2.3 per nm^2) at various hCAII surface densities. At a hCAII surface density of 9.1E-4 per nm^2, nanoparticle introduction did not induce any changes in the system (Figure 3.4a). Since there was no interaction between GUVs, the contact angle of adhesion here was assigned a value of 0°. However, at a higher surface density of 18.3E-4 per nm^2, adhesion was observed between the GUVs, and the average contact angle in the samples was measured to be 37.3° (Figures 3.4c, 3.4k). At a value of 37.5E-4 per nm^2, adhesion became visibly stronger, as evidenced by the increase in average adhesion angle to 118.8° (Figures 3.4e, 3.4k). At the highest surface density of 75E-4 per nm^2, the largest adhesion angles were also observed and amounted to an average of 140.7° (Figure 3.4g, 3.4k). Interestingly, at 75E-4 per nm^2 surface density, about 10% of the GUVs also exhibited a “swallowing” phenomenon as evidenced by the

presence of FITC-dextran containing GUVs within GUVs containing rhodamine-dextran, or vice-versa (Figure 3.4i). In addition, at 37.5E-4 and 75E-4 per nm^2 hCAII, GUV lysis was observed after ~ 36 h of incubation as evidenced by the leakage of the dextran-dye in the surrounding GUV environment (Figures 3.4f and 3.4h). However, at lower hCAII surface densities of 9.1E-4 and 18.3E-4, no lysis was observed even after 80 h of incubation with the sulfonamide nanoparticles (Figures 3.4b and 3.4d).

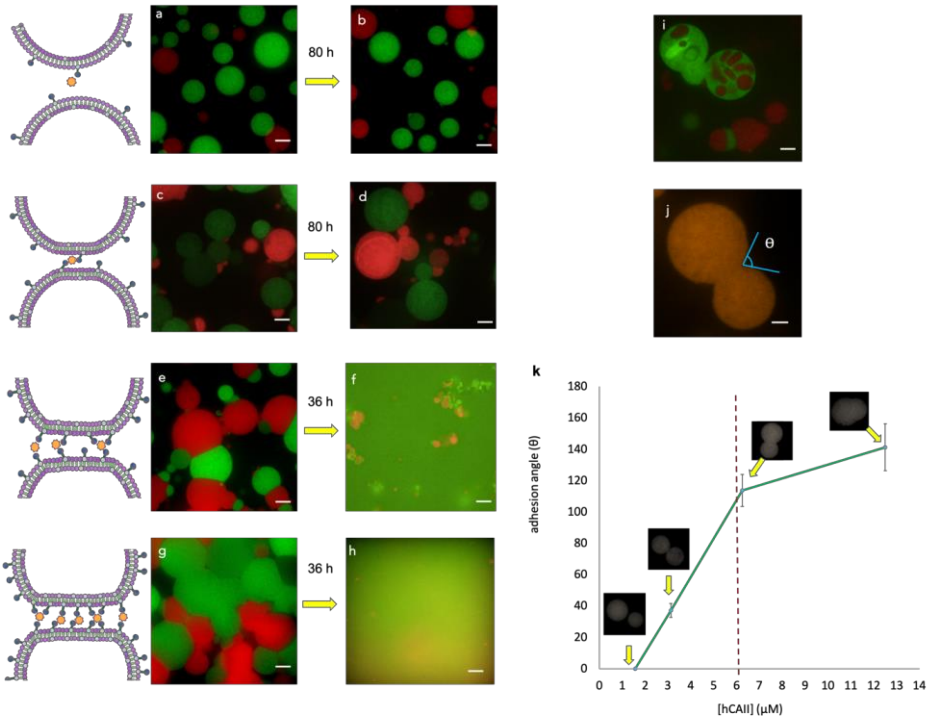

FIGURE 3.4: Composite microscopy images showing extents of GUV adhesion at varying hCAII surface densities. Nanoparticles were fixed at 420 nm, 13 μM sulfonamide concentration, and surface density of 2.3 per nm^2. a-b) No adhesion with nanoparticle addition at 9.1E-4 per nm^2 hCAII after 80 h; c-d) maintenance of GUV adhesion with nanoparticle addition at 18.3E-4 per nm^2 hCAII even after 80h ; e-f) adhesion followed by rupture with nanoparticle addition at 37.5E-4 per nm^2 hCAII; g-h) adhesion followed by rupture with nanoparticle addition at 75E-4 per nm^2 hCAII; i) swallowing observed with nanoparticle addition at 75E-4 per nm^2 hCAII; j) Image showing how adhesion angles were measured in GUV samples; k) Plot of adhesion angle vs. [hCAII] (angles were measured 1h after nanoparticle addition). Scale bar is 20 μm.

3.3.2 ESTIMATION OF ADHESION STRENGTH

An estimation of adhesion strength was made by utilizing average adhesion angles obtained in the previous section in terms of the work of adhesion (W). Generally, the shape of a vesicle is determined by a combination of W, membrane tension ($\boldsymbol{\tau}$), and bending modulus of the lipid membrane (κ). While κ affects the shape of the membrane over smaller length scales, the membrane tension affects the GUV shape over larger scales of length. Considering that value of κ is small for a DOPC/Chol membrane, the membrane shape will be dominated by $\boldsymbol{\tau}$ rather than κ. In this tension dominated regime, it would be possible to obtain actual adhesion energy values[32] using Young's equation,

$$W = 2\boldsymbol{\tau}(1-\cos\theta)$$

where θ is the contact angle between the vesicles. Since the value of $\boldsymbol{\tau}$ is unknown in our experiments, we estimated the upper limit of W for our system using an approximate $\boldsymbol{\tau}$ value. In general, the values of $\boldsymbol{\tau}$ in GUVs composed of a DOPC/Chol membrane can range between the μN/m and mN/m range. The value of maximum $\boldsymbol{\tau}$ for DOPC/Chol just below lysis is usually in the mN/m range.[27,28] Hence, if we consider an approximate $\boldsymbol{\tau}$ value of 1 mM/m, the upper value of W at the largest contact angle value (140.7°) would be 3.55 mJ/m^2. The lower limit of W would be zero since at low amounts of enzyme or ligand, no adhesion was observed. From these values, the range of W in our GUV system is anticipated to be between 0 – 3.55 mJ/m^2.

3.3.3 INFLUENCE OF CONCENTRATION RATIO OF RECEPTOR AND LIGAND

In this section, the effect of the receptor (R) and ligand (L) concentrations, and subsequently the R:L concentration ratio were explored and were all found to influence GUV

adhesion. Receptor and ligand concentrations were varied by keeping the nanoparticle size and sulfonamide density a constant (at 420 nm and 2.3 per nm^2, respectively). The values of contact angles were obtained at different R:L ratios in Figures 3.5a and 3.6a. A closer look at these values reveals a trend in adhesion based on the total concentrations of hCAII and sulfonamide in the sample. When the receptor and ligand concentrations were increased gradually but maintained at a constant R:L value of ~1, the average adhesion angles were also seen to increase and measured to be 0°, 30.4°, 109.2°, and 140.7° respectively (highlighted by the diagonal green boxes in Figure 3.6a). However, when the R:L ratio was not maintained at 1, the values of adhesion angles were dependent on whether the receptor or ligand concentration "limited" the binding event. For example, when the concentration of the receptor or ligand was limited to 3 μM, adhesion angles were close to each other and are highlighted by the red boxes in Figure 4a. A similar observation can be made when the concentration was limited to 6 μM (highlighted by yellow boxes in Figure 3.6a). Corresponding W values were also calculated and can also be found in Figure 3.6a.

Next, the effect of R:L ratio was explored at a lower sulfonamide surface density of 0.27 per nm^2 at the same nanoparticle size of 420 nm. It was observed that at both sulfonamide surface densities of 2.3 and 0.27 per nm^2, the corresponding adhesion angles (and W values) at various R:L ratios were similar to each other when compared (Figure 3.5a-b, 3.6a-b). As seen previously, an increasing trend was obtained when the receptor and ligand concentrations were increased gradually but maintained at R:L ~1. The similarity of these angles even at the lower sulfonamide density suggests that the nanoparticle size is a crucial parameter that directs membrane morphology changes, and we sought to explore the effects of size in the next section.

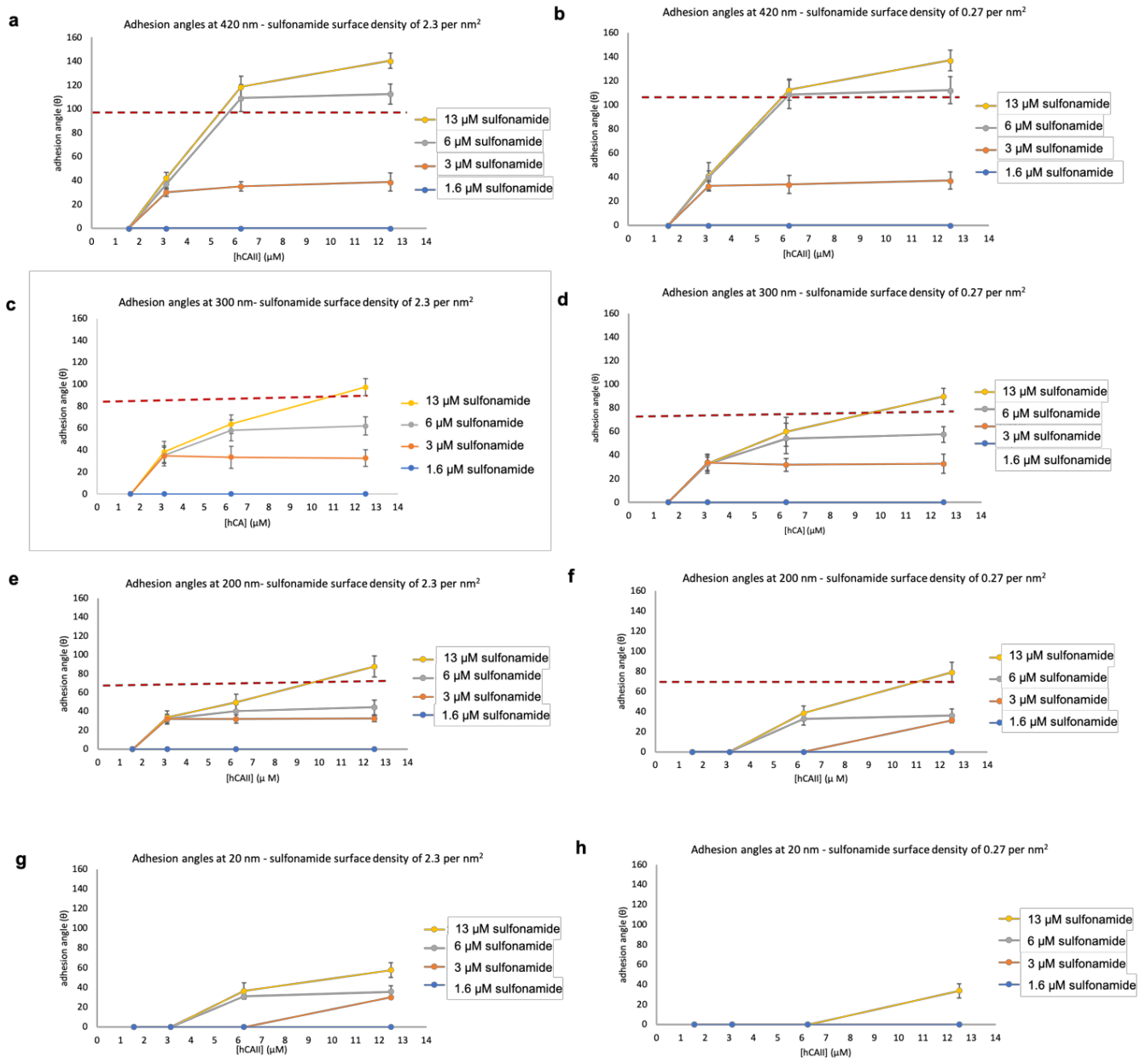

FIGURE 3.5: Influence of R:L ratio at various sizes. a) Plots of average adhesion angles at 420 and at sulfonamide surface density of 2.3 per nm^2; b) plots of average adhesion angles at 420 and at sulfonamide surface density of 0.27 per nm^2; c) plots of average adhesion angles at 300 nm and at sulfonamide surface density of 2.3 per nm^2; d) plots of average adhesion angles at 300 nm and at sulfonamide surface density of 0.27 per nm^2; e) plots of average adhesion angles at 200 nm and at sulfonamide surface density of 2.3 per nm^2; f) plots of average adhesion angles at 200 nm and at sulfonamide surface density of 0.27 per nm^2; g) plots of average adhesion angles at 20 nm and at sulfonamide surface density of 2.3 per nm^2; h) plots of average adhesion angles at 20 and at sulfonamide surface density of 0.27 per nm^2.

3.3.4 INFLUENCE OF CONCENTRATION RATIO OF RECEPTOR AND LIGAND (AT DECREASING NANOPARTICLE SIZES)

Nanoparticle size was seen play a role in GUV morphology change at varying receptor/ligand concentrations and R:L ratios. To study the effects of size, 300 nm, 200 nm, and 20 nm silica nanoparticles were surface-modified with benzenesulfonamide (Scheme 3.1, Tables 3.1-3.2). First, studies were performed while maintaining the sulfonamide surface density at ~2.3 per nm^2 to directly compare with the results obtained at 420 nm. As a result, any changes in adhesion angles while maintaining sulfonamide surface density would be attributed to a size decrease. This is based on the premise that as the nanoparticle size grows, its surface area also increases, making it less challenging to establish multivalent surface contacts on GUVs (Figure 3.7a). In addition, the property of steric exclusion would come into play since the exposed surface area of the nanoparticle after initial binding would be greatly reduced in the case of the 20 nm particle compared to a particle that is 420 nm. This, in turn, would result in a lower affinity of the smaller particle to recruit and establish multivalent contacts between receptors on adjacent GUVs, leading to an overall decrease in the extent of adhesion and W values. On comparing the adhesion angles obtained for 300 nm, 200 nm, and 20 nm nanoparticles, the corresponding adhesion angles and W were seen to decrease based on size across all concentrations of hCAII and sulfonamide (Figures 3.5a, c, e, g, and Figures 3.6a, c, e, g). In general, the observed trend in corresponding contact angles was 420 nm > 300 nm > 200 nm > 20 nm. This suggests that steric exclusion and a decreased ability to establish multivalent contacts with GUVs does play a role during the binding process as result of size decrease. In addition, at all sizes, there was an overall increase in adhesion angles as sulfonamide and hCAII concentrations were increased but maintained at a R:L ratio of ~ 1. Again, at R:L ratios greater and less than 1, the angles and W values were dependent on whether

the receptor or ligand limited binding (Figures 3.5a, c, e, g and 3.6a, c, e, g). Studies were also done at a lower sulfonamide surface density of 0.27 per nm^2 across all sizes (Figures 3.5b, d, e, f and 3.6b, d, e, f). At 300 nm, a drastic change in angles were not observed at a lower sulfonamide surface density and were similar to those obtained at the surface density of 2.3 per nm^2 (Figure 3.5c-d, 3.6c-d). Overall, the angles at 300 nm and respective W values increased when hCAII and sulfonamide concentrations increased while maintaining the R:L ratio of 1. When this ratio was not maintained, receptor or ligand concentration limited binding was again observed. However, a lower sulfonamide surface density greatly influenced binding when the size was 200 nm or 20 nm (Figures 3.5e-f, 3.6e-f, 3.5g-h, 3.6g-h). For 200 nm particles at the lower density, adhesion angles fell to 0° when sulfonamide or hCAII concentrations approached a concentration of 3 μM or lower (Figure 3.6f). This effect was especially magnified in the case of the 20 nm particles at the lower surface density, where adhesion was observed only at 12.5 μM hCAII and 13 μM sulfonamide, and at all other concentrations, the angles were found to be 0° (Figure 3.6h).

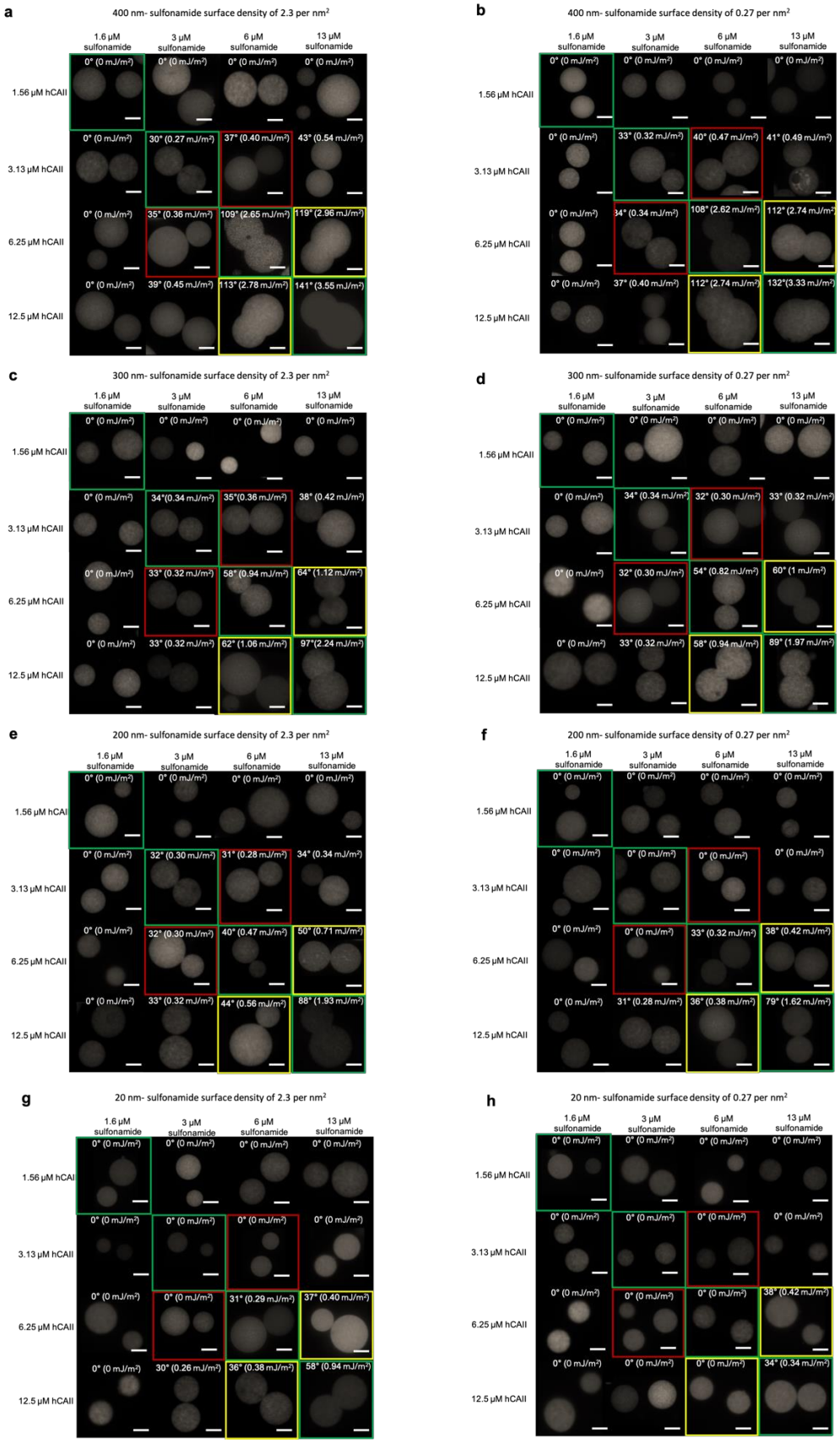
a
400 nm- sulfonamide surface density of 2.3 per nm²
1.6 µM sulfonamide
3 µM sulfonamide
6 µM sulfonamide
13 µM sulfonamide
1.56 µM hCAII
3.13 µM hCAII
6.25 µM hCAII
12.5 µM hCAII
0° (0 mJ/m²)
30° (0.27 mJ/m²)
37° (0.40 mJ/m²)
43° (0.54 mJ/m²)
35° (0.36 mJ/m²)
109° (2.65 mJ/m²)
119° (2.96 mJ/m²)
39° (0.45 mJ/m²)
113° (2.78 mJ/m²)
141° (3.55 mJ/m²)
b
400 nm- sulfonamide surface density of 0.27 per nm²
33° (0.32 mJ/m²)
40° (0.47 mJ/m²)
41° (0.49 mJ/m²)
108° (2.62 mJ/m²)
112° (2.74 mJ/m²)
37° (0.40 mJ/m²)
112° (2.74 mJ/m²)
132°(3.33 mJ/m²)
c
300 nm- sulfonamide surface density of 2.3 per nm²
34°(0.34 mJ/m²)
35°(0.36 mJ/m²)
38° (0.42 mJ/m²)
33° (0.32 mJ/m²)
58° (0.94 mJ/m²)
64° (1.12 mJ/m²)
33° (0.32 mJ/m²)
62° (1.06 mJ/m²)
97°(2.24 mJ/m²)
d
300 nm- sulfonamide surface density of 0.27 per nm²
34° (0.34 mJ/m²)
32° (0.30 mJ/m²)
33° (0.32 mJ/m²)
32° (0.30 mJ/m²)
54° (0.82 mJ/m²)
60° (1 mJ/m²)
33° (0.32 mJ/m²)
58° (0.94 mJ/m²)
89° (1.97 mJ/m²)
e
200 nm- sulfonamide surface density of 2.3 per nm²
32° (0.30 mJ/m²)
31° (0.28 mJ/m²)
34° (0.34 mJ/m²)
32° (0.30 mJ/m²)
40° (0.47 mJ/m²)
50° (0.71 mJ/m²)
33° (0.32 mJ/m²)
44° (0.56 mJ/m²)
88° (1.93 mJ/m²)
f
200 nm- sulfonamide surface density of 0.27 per nm²
33° (0.32 mJ/m²)
38° (0.42 mJ/m²)
31° (0.28 mJ/m²)
36° (0.38 mJ/m²)
79° (1.62 mJ/m²)
g
20 nm- sulfonamide surface density of 2.3 per nm²
31° (0.29 mJ/m²)
37° (0.40 mJ/m²)
30° (0.26 mJ/m²)
36° (0.38 mJ/m²)
58° (0.94 mJ/m²)
h
20 nm- sulfonamide surface density of 0.27 per nm²
38° (0.42 mJ/m²)
34° (0.34 mJ/m²)

FIGURE 3.6: Influence of concentration ratio of receptor and ligand at varying nanoparticle size: the green boxes indicate the representative angles obtained when R:L is ~1; red boxes indicate the representative angles when binding is limited by a concentration of 3 μM ; yellow boxes indicate the representative angles when binding is limited by a concentration of 6 μM. a) Optical images of representative adhesion angles at 400 nm and sulfonamide surface density of 2.3 per nm^2; b) Optical images of representative adhesion angles at 400 nm and sulfonamide surface density of 0.27 per nm^2; c) Optical images of representative adhesion angles at 300 nm and sulfonamide surface density of 2.3 per nm^2; d) Optical images of representative adhesion angles at 300 nm and sulfonamide surface density of 0.27 per nm^2; e) Optical images of representative adhesion angles at 200 nm and sulfonamide surface density of 2.3 per nm^2; f) Optical images of representative adhesion angles at 200 nm and sulfonamide surface density of 0.27 per nm^2; g) Optical images of representative adhesion angles at 20 nm and sulfonamide surface density of 2.3 per nm^2; h) Optical images of representative adhesion angles at 20 nm and sulfonamide surface density of 0.27 per nm^2. In all images corresponding W values are indicated in parentheses. Scale bar is 5 μm.

3.3.5 NANOPARTICLE-GUV INTERACTION MODELS

Particle-GUV interaction models provide useful information to explain the variation in adhesion extents seen in the previous sections (Figure 3.6). In cases where no adhesion was observed, it is hypothesized that the surface density of the receptor and/or sulfonamide ligand is below the threshold required to facilitate multivalent contacts on the GUV surface. As a result, it would be impossible for the sulfonamide nanoparticles to initiate binding with hCAII on adjacent GUVs (Figure 3.7b). In samples where only adhesion was the outcome of the interaction, the surface densities of hCAII or sulfonamide are such that multivalent interactions with hCAII can be facilitated, and inter-GUV adhesion can be maintained over time (Figure 3.7c). Under these conditions, the nanoparticles are also hypothesized to be present superficially at the GUV membrane interface and remain only partially wrapped by the membrane, as shown. This would fail to cause any significant change in the GUV membrane tension, and as a result, it would be

difficult for the system to transition to lysis. For the outcomes that involve adhesion followed by lysis, hCAII and sulfonamide surface densities are large enough for the particles to first establish multivalent contacts between adjacent GUVs. However, since the number of contacts would be higher than in Figure 5c, these nanoparticles can additionally get wrapped almost completely by the membrane with increasing time, as shown in Figure 3.7d. Subsequent membrane stretching due to this wrapping process would then lead to an increase in membrane tension until it reaches the membrane lysis point. In Figure 3.5, the points at which lysis occurs are shown by the dotted

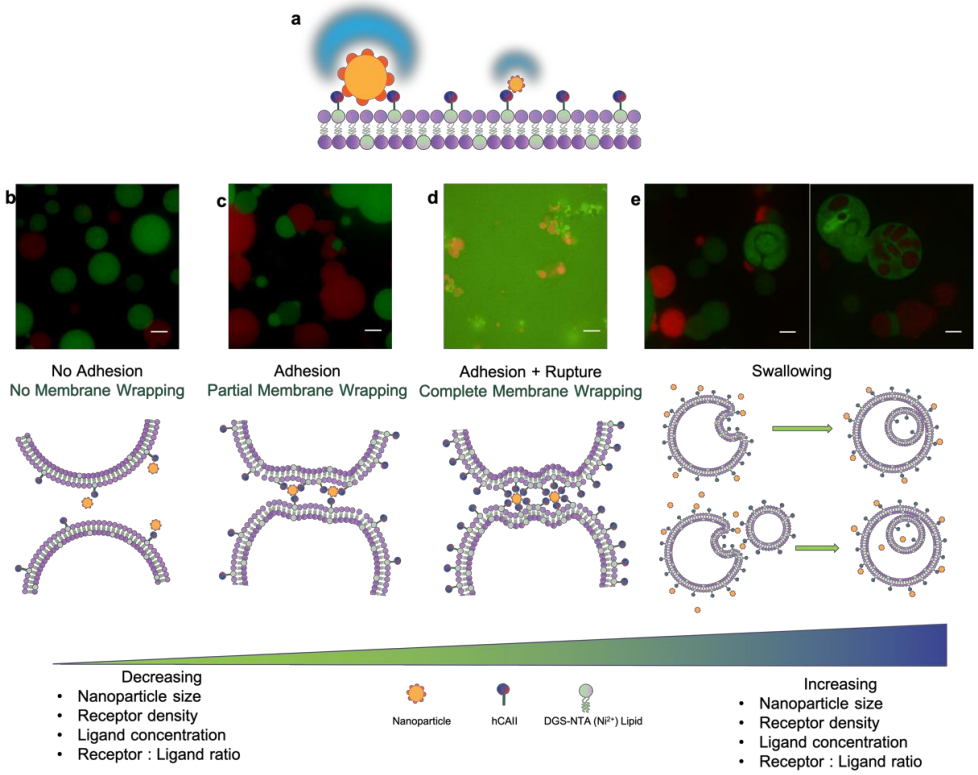

FIGURE 3.7: Nanoparticle-GUV interaction models. a) Illustration showing the influence of nanoparticle size on binding and steric exclusion leading to insufficient/weak binding due to smaller exposed surface area in a smaller nanoparticle b) no adhesion observed at insufficient surface coverages of hCAII or sulfonamide; c) adhesion without lysis due to partial membrane binding around nanoparticles; d) adhesion followed by lysis due to complete membrane wrapping around nanoparticles; e) swallowing observed in GUVs when 420 nm particles were introduced at 13 M sulfonamide and sulfonamide surface density of 2.3 per nm^2. Scale bar = 20 µm.

red lines. Since rupture was observed to start occurring at adhesion angles close to 78°, the minimum W value to facilitate lysis can be roughly estimated to be ~ 1.58 mJ/m^2. Finally, the "swallowing" phenomenon observed at 420 nm (Figure 3.7e) is believed to be a result of morphology changes induced in the membrane during interfacial nanoparticle interactions. When these fluctuations induce the opportune morphology, smaller GUVs may be produced within the same GUV internally. Alternatively, larger GUVs may also interact with adjacent smaller ones through receptor-nanoparticle binding, where this event finally leads to the smaller GUV to be engulfed over time.

3.4 CONTROL EXPERIMENTS

3.4.1 GFP IMMOBILIZATION ON GUVS:

To confirm the immobilization of hCAII on the surface of the GUVs via coordination with Ni^{2+}, microscopy experiments were performed using rhodamine-dextran containing GUVs and GFP protein. The presence of a green ring around the GUV encapsulating rhodamine dextran dye confirms the immobilization of GFP on the surface of the GUV via coordination with Ni^{2+} (Figure 3.8).

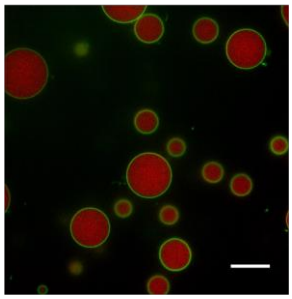

FIGURE 3.8: Composite image of rhodamine-dextran containing GUV (red channel) immobilizing GFP (green channel).

3.4.2 VESICLE SWALLOWING STUDIES WITH MEMBRANE-TAGGED GUVS:

To confirm vesicle swallowing, imaging experiments were performed using membrane-labeled GUVs instead of encapsulating a dextran dye within the GUV lumen. For labeling GUV membrane, either NBD tagged- or rhodamine tagged-lipid was doped into the DOPC-cholesterol at 0.5% total lipid concentration. The presence of differently colored vesicles within the larger vesicle suggests that the swallowing process happened after introducing the sulfonamide modified silica nanoparticles and not inherently formed during the GUV electroformation process (Figure 3.9).

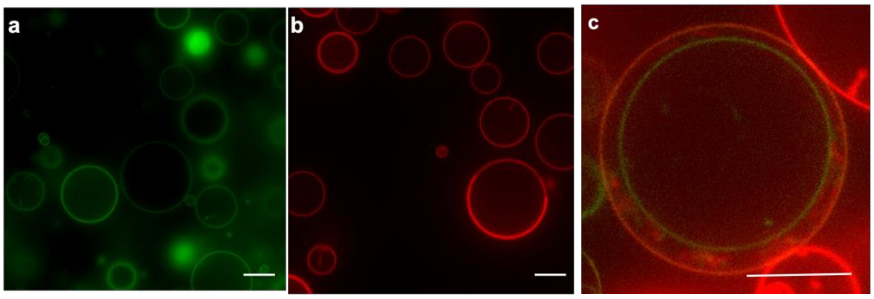

FIGURE 3.9: Membrane labeling experiments to confirm vesicle swallowing. a) Image of GUVs containing NBD-tagged lipid in the membrane (Scalebar is 20 μm); b) Image of GUVs containing rhodamine-tagged lipid in the membrane (Scalebar is 20 μm); c) Composite image of NBD membrane-tagged GUV within rhodamine membrane-tagged GUV confirming swallowing process (Scale bar is 10 μm).

3.4.3 STUDIES AT NO HCAII IMMOBILIZATION:

Experiments were performed to confirm that GUVs containing no surface immobilized hCAII did not show adhesion. 10 mg of sulfonamide-modified silica nanoparticles were weighed, and 1 mL distilled water added to obtain a solution of 10 mg/mL. Studies were done by incubating 10 μL of GUVs with no hCAII and adding 400 μL of the corresponding 10 mg/mL solution containing sulfonamide-modified silica nanoparticles of varying sizes. The samples were diluted

to 1 mL and imaged by injecting 20 µL of the GUV-nanoparticle mixture into perfusion chambers. Microscopy images in Figure 3.10 show that the hCAII immobilized GUVs remain separated from each other after introducing nanoparticles with no sulfonamide.

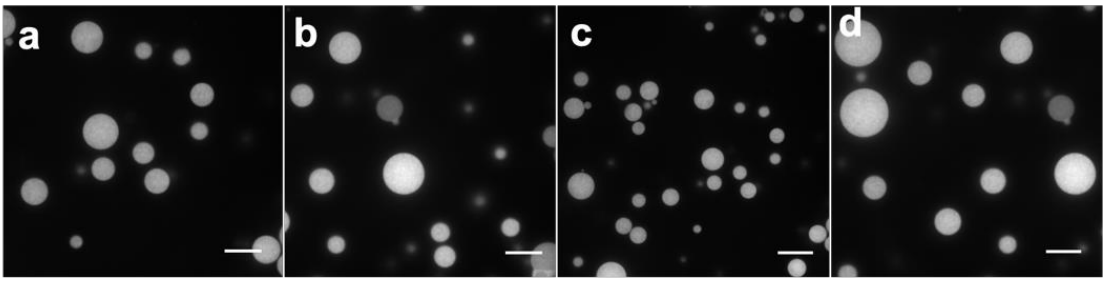

FIGURE 3.10: Control experiments showing that GUVs remain separated from each other when no hCAII was present on the surface of GUVs a) with 420 nm sulfonamide modified silica nanoparticles; b) with 300 nm sulfonamide modified silica nanoparticles; c) with 200 sulfonamide modified silica nanoparticles; d) with 20 nm sulfonamide modified silica nanoparticles. Scale bar is 20 µm.

3.4.4 Studies with unmodified silica nanoparticles:

Experiments were performed to confirm that unmodified silica nanoparticles did not induce adhesion between GUVs. Studies were done at highest hCAII concentration by incubating 10 µL of the GUV sample with 400 µL unmodified silica nanoparticles. The samples were diluted to 1

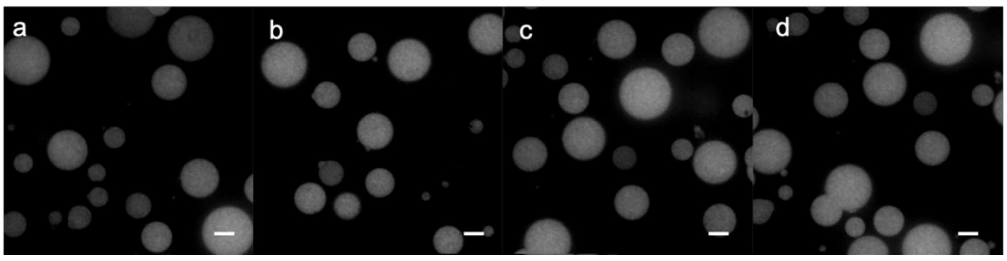

FIGURE 3.11: Control experiments showing that GUVs remain separated from each other when non-functionalized a) 420 nm silica nanoparticles were used; b) 300 nm silica nanoparticles were used; c) 200 silica nanoparticles were used; d) 20 nm silica nanoparticles were used. Scale bar is 20 µm.

mL and imaged by injecting 20 μL of the GUV-nanoparticle mixture into perfusion chambers. Microscopy images in Figure 3.11 show that the hCAII immobilized GUVs remain separated from each other after introducing nanoparticles with no sulfonamide.

3.5 CONCLUSIONS

We used a synthetic GUV-based platform to immobilize a model receptor, hCAII, to evaluate the interfacial membrane effects of complementary sulfonamide-based nanoparticles. The introduction of sulfonamide nanoparticles led to GUV adhesion via receptor-mediated binding, and adhesion strength could be qualitatively estimated through the angles of adhesion. Overall, it was found that interfacial changes and associated systemic energies were found to be dependent on nanoparticle size, R and L surface densities, individual concentrations of the R and L, and overall R:L concentration ratio. At a certain sulfonamide and hCAII surface density, it was found that the nanoparticle size influenced adhesion strength and followed the trend: 420 nm > 300 nm > 200 nm > 20 nm. Adhesion was also dependent on the concentration ratios of the receptor and ligand, with a ratio of R:L ~ 1 being most favorable for adhesion. These results indicate that the combined effects of nanoparticle multivalency and steric exclusion play a crucial role in determining the outcome after the interfacial binding process. We also estimated an approximate range for the work of adhesion during nanoparticle binding and was calculated to be between 0 – 3.55 mJ/m^2. Within this range, systemic instabilities started to occur at 1.58 mJ/m^2, making the system transition from adhesion to lysis. Our simple synthetic model also is extended as a platform to study the effects of any other receptor-ligand pair and can have vast implications in the fields of synthetic biology, nanotechnology, and medicine.

3.6 REFERENCES

1. Watson, H. Biological Membranes. *Essays Biochem.* **2015**, *59,* 43-69.

2. Barrow, E.; Nicola, A. V. Multiscale Perspectives of Virus Entry via Endocytosis. *Virol. J.* **2013**, *10,* 177-186.

3. Friedman, A. D.; Claypool, S. E.; Liu, R. The Smart Targeting of Nanoparticles. *Curr. Pharm. Des.* **2013**, *19,* 6315-6329.

4. Yu, B.; Tai, H. C.; Xue, W.; Lee, J. L.; Lee, R. J. Receptor-Targeted Nanocarriers for Therapeutic Delivery to Cancer. *Mol. Membr. Biol.* **2013**, *27,* 286-298.

5. Rosenblum D.; Joshi, N.; Karp, J.; Peer, D. Progress and Challenges Towards Targeted delivery of Cancer Therapeutics. *Nat. Comm.* **2018**, 9, 1410-1421.

6. Zhang, S.; Gap, H.; Bao, G. Physical Principles of Nanoparticle Cellular Endocytosis. *ACS Nano.* **2015,** *9*, 8655-8671**.**

7. Rodriguez-Hernandez, A. G.; Vazquez-Duhalt, R.; Huerta-Saquero, A. Nanoparticle-Plasma Membrane Interaction: Thermodyanimcs, Toxicity and Cellular Response. *Curr. Med. Chem.* **2020**, *27*, 3330-3345.

8. Claudia, C.; Schneemilch, M.; Gaisofrd, S.; Quirke, N. Nanoparticle-Membrane Interactions. *J. Exp. Nanosci.* **2018**, *13*, 62-81.

9. Chen, K. L.; Bothun, G. D. Nanoparticles Meet Cell Membranes: Probing Non-specific Interaction Using Model Membranes. *Environ. Sci. Tech*. **2014**, *48*, 873-880.

10. Rossi, G.; Monticelli, L. Gold Nanoparticles in Model Biological Membranes: A Computational Perspective. *Biochim. Biophys. Acta Biomembr.* **2016**, *1858,* 2380-2389.

11. Li, Y.; Chen, X.; Gu, N. Computational Investigation of Interaction between Nanoparticles and Membranes: Hydrophobic/Hydrophilic Effect. *J. Phys. Chem. B* **2008**, *51,* 16647-16653.

12. Lai, K.; Wang, B.; Zhang, Y.; Zheng, Y. Computer Simulation Study of Nanoparticle Interaction with a Lipid Membrane under Mechanical Stress. *Phys. Chem. Chem. Phys.* **2013**, *15,* 270-278.

13. Rasel, M. A. I; Singh, S.; Nguyen, T. D.; Afara, I. O.; Gu, Y. Impact of Nanoparticle Uptake on the Biophysical Properties of Cell for biomedical Engineering Applications. *Sci. Rep*. **2019**, *9*, 5849-5861.

14. Behzadi, S.; Serphooshan, V.; Tao, W.; Hamaly, M.; Alkawareek, M. Y.; Dreaden, E. C.; Brown, D.; Alkilany, A. M.; Farokhzas, O. C.; Mahmoudi, M. Cellular Uptake of Nanoparticles: Journey Inside the Cell. *Chem. Soc. Rev.* **2017**, *46*, 4218-4244.

15. Mourdikoudis, S.; Pallares, R. M.; Thanh, N. T. K. Characterization Techniques for Nanoparticles: Comparison and Complementarity upon Studying Nanoparticle Properties. *Nanoscale* **2018**, *10*, 12871-12934.

16. McMahon, H.; Boucrot, E. Membrane Curvature at a Glance. *J. Cell Sci*. **2015**, *128*, 1065-1070.

17. Ting, C.; Wang, Z.-G. Interaction of a Charged Nanoparticle with a Lipid Membrane: Implication for Gene Delivery. *Biophys. J.* **2011**, *100*, 1288-1297.

18. Duan, H.; Li, J.; Zhang, H.; Qiu, F.; Yang, Y. Conformations of a Charged Vesicle Interacting with an Oppositely Charged Particle. *J. Biol. Phys.* **2018**, *44*, 1-16.

19. Farnoud, A.; Nazemidashtarjandi, S. Emerging Investigator Series: Interaction of Engineered Nanomaterials with the Cell Plasma Membrane, What Have We Learned from Membrane Models? *Environ. Sci. Nano*. **2019**, *6*, 13-40.

20. Zuraw-Weston, S.; Wood, D.; Torres, I. K.; Lee, Y.; Wang, L.-S.; Jiang, Z.; Lazaro, G. R.; Wang, S.; Rodal, A. A.; Hagen, M.; Rotello, V. M. Dinsmore, A. D. Nanoparticles Binding to Lipid Membranes: from Vesicle-Based Gels to Vesicle Tubulation and Destruction. *Nanoscale* **2019**, *11*, 18464-18474.

21. Cao, R.; Kumar, D.; Dinsmore, A. D. Vesicle-based Gel via Polyelectrolyte-Induced Adhesion: Structure, Rheology, and Response. *Langmuir* **2021**, *37*, 1714-1724.

22. Mondal, J.; Friesner, R. A.; Berne, B. J. Role of Desolvation in Thermodynamics and Kinetics of Ligand Binding to a Kinase. *J. Chem. Theory Comput.* **2014,** *10,* 5696-5705.

23. An, Y.; Chem, M.; Xue, Q.; Liu, W. Preparation and Self-Assembly of Carboxylic Acid Functionalization. *J. Coll. Interface Sci*., **2007**, *311*, 507-213.

24. Zhuravlev, L. T. The Surface Chemistry of Amorphous Silica. Zhuravlev Model. *Colloids Surf.* **2000**, *173*, 1-38.

25. Madeley, J. D.; Richmond, R. C. A Procedure for Determining the Concentration of Hydroxyl Groups on Silica Surfaces. *Z. Anorg. Allg. Chem.,* **1972**, *389*, 92–96.

26. Zentner, C. A.; Anson, F.; Thayumanavan, S.; Swager, T. M. Dynamic Imine Chemistry at Complex Double Emulsion Interfaces. *J. Am. Chem. Soc.,* **2019**, *141*, 18048-18055.

27. Wang, S. C.; Zambie, D. B. Fluorescence Analysis of Sulfonamide Binding to Carbonic Anhydrase. *Biochem. Mol. Biol. Edu*., **2006**, *34*, 364-368.

28. Nair, S.; Krebs, K. J. F.; Christianson, D. W.; Fierke, C. A. Structural Basis of Inhibitor Affinity to Variants of Human Carbonic Anhydrase II. *Biochemistry*, **1995**, *34*, 3981–3989.

29. Herold, C.; Chwastek, G.; Schwille, P.; Petrov, E. P. Efficient Electroformation of Supergiant Unilamellar Vesicles Containing Cationic Lipids on ITO-Coated Electrodes. *Langmuir* **2012**, *28*, 5518-5521.

30. Krishnamurthy,V. M.; Kaufman, G. K.; Urbach, A. R.; Gitlin, I.; Gudiksen, K. L.; Weibel,D. B.; Whitesides, G. M. Carbonic Anhydrase as a Model for Biophysical and Physical-Organic Studies of Proteins and Protein-Ligand Binding. *Chem. Rev.* **2008**, *108*, 946-1051.

31. Kelly, D. F.; Dukovski, D.; Walz, T. Monolayer Purification: A Rapid Method for Isolating Protein Complexes for Single-Particle Microscopy. Proc. Natl. Acad. Sci. U.S.A. **2008**, *105*, 4703-4708.

32. Yanagisawa, M.; Yoshida, T.; Furuta, M.; Nakata, S.; Tokita, M. Adhesive Force between Paired Microdroplets coated with Lipid Monolayers. *Soft Matter* **2013**, *9,* 5891-5897.

CHAPTER 4

4.1 INTRODUCTION

In the previous chapters, covalent, and non-covalent interactions were used to bring about interfacial destabilization and morphology changes in surfactant and lipid-based supramolecular

assemblies respectively. These processes mimic some of the interfacial processes occurring at the interface of various cellular components. Next, we turn our attention towards chemotactic activity of biological systems. Various supramolecular assemblies found in Nature exhibit fascinating dynamical chemotactic properties and stimuli-responsive behaviors.[1-2] For example, during different phases of growth, development and sustenance, cells can sense the density and distribution of extracellular matrix (ECM) molecules via surface proteins and through the formation of complexes.[1-2] Through selective recognition and binding of ligands, crucial control over cellular activity can be obtained.[3-5] Leukocytes for example, which form a part of the immune system, displays a unique chemotactic ability to sense and react to an external "threat". This dynamic capability is controlled by a complex network of protein-protein and protein-carbohydrate interfacial interactions.[10-16] Initially, these cells scan the surface of blood capillaries via rolling, however, they start to slow down in the presence of surface markers indicative of an infection, and eventually stop and release inflammatory signals to combat the foreign material.[1,4-9] The development of synthetic systems/materials that mimics the complexity and autonomous fidelity of the immune system is certainly a daunting challenge. It would be a breakthrough in many fields if similar autonomous functionalities exhibited in biological systems can be introduced into synthetic platforms for selective binding, dynamic scanning/movement, and reaction to ligand density, (Figure 4.1a). However, to achieve this goal, fundamental insights must be obtained on the molecular factors controlling the selective non-covalent interactions and the complex interplay (and competition) between them at the interface.

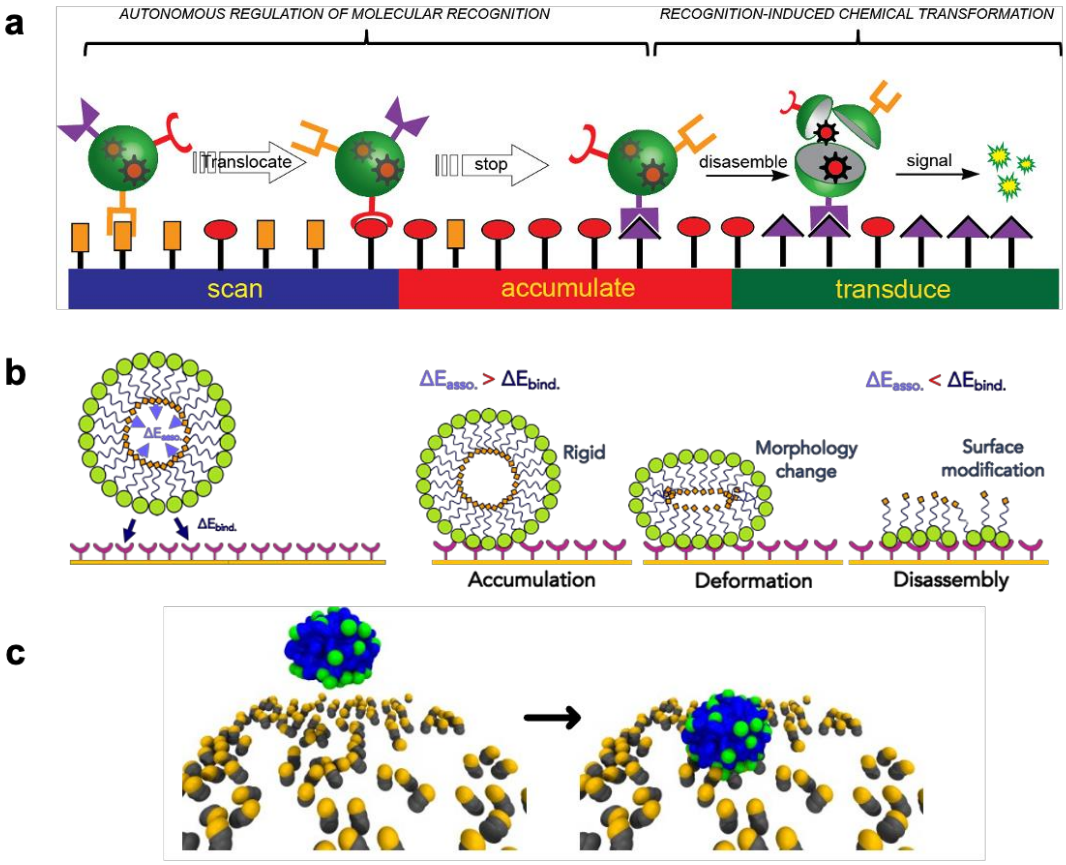

FIGURE 4.1: Multivalent adhesion and chemotaxis in natural and synthetic assemblies. a) Cells can bind and autonomously, translocate on surfaces by rolling, and sample them to release inflammatory signals in the presence of high densities of surface markers indicative of an infection. b). ΔE_{bind} vs ΔE_{ass} competition. Upon interaction with a surface, the nanoparticle morphology depends on the competition between the monomers-receptors interactions and the monomer-monomer self-assembly energy. If ΔE_{ass} prevails, accumulation can be expected; and if ΔE_{bind} dominates, deformation or disassembly of the nanoparticle can be expected. c) Example molecular model of a supramolecular NP (monomers colored in blue and green) before (left) and after adhesion (right) on a ligand-coated surface (ligands in gray, active binding groups in orange). (Figure 4.1 c obtained from reference 29)

Some notable platforms that provide design guidelines for the development of such systems are based on synthetic supramolecular structures obtained via self-assembly of molecular units,

such as fibers, vesicles, tubes, etc., which can actively respond to selective stimuli.[6-12] Micellar assemblies that selectively disassemble upon specific binding of proteins to complementary ligands present in the structure of the self-assembling dendron units have been also been reported.[13] In other reports, responsive nanoparticles (NPs) capable of surface binding, autonomous moving and releasing encapsulated guests under specific biological stimuli have been studied.[14-17] For example, *Liao et al.* studied the correlation of the surface density of active binding groups on gold nanoparticles and their diffusion rate during their interaction with supported lipid bilayer membranes. They were able to show that a reduction in the density of the active binding groups accelerates the diffusion of nanoparticles on the lipid bilayer surface.[18] However, despite notable advances in surface modification and control, several technical experimental limitations persist and prevent the rational design of chemotactic functional materials.[19] Tracking and observation of the movement of soft nanoparticles on surfaces have proven to be a challenge due to resolution limitations associated with current characterization techniques.[20-21] At drastically small spatiotemporal scales, it is difficult to gain sufficient insight into various molecular factors and processes that govern chemotactic responsive behavior since these materials have to be observed sub-molecular resolution. As a result, molecular models and computer simulations have become fundamental to reach such goals. Recent studies have used minimalistic coarse-grained (CG) models to study the adhesion and dynamics of nanoparticles/cells onto ligand-functionalized surfaces[22,23,24,25]. Similar minimalistic CG models have also allowed the monitoring of the rolling process of a deformable or soft spherical cell model on surfaces under the presence of an external flow.[23] These studies however, treat nanoparticles as a single soft spheres, and allow the observation of the tendency of a sphere covered by ligands to autonomously move onto a surface to maximize the multivalent interactions with the surface. However, finer-level models are

required to support the development of self-assembled nanoparticles that can respond to a surface chemical gradient via rolling, subsequently getting triggered to exhibit controlled responses such as disassembly, and release of encapsulated guest molecules after the rolling process. This requires modeling techniques to visualize the self-assembled nanoparticles as an assembly of monomers rather than as a single soft sphere. At the same time, it would also be desirable to keep the resolution in the molecular models high enough to maintain a chemical relevance, and to obtain molecularly relevant insights. *In silico* simulations coupled with traditional experimental techniques would allow the development and response of supramolecular polymeric materials to different biorelevant stimuli, such as changes in temperature, salts, solvents, light, etc.[13,31,32]. However, it should be kept in mind that intriguing bioinspired properties such as chemotaxis are intrinsically dynamic, and it is important that the dynamic behavior of chemotactic assemblies be observed at sub-molecular resolution to obtain molecularly relevant information on how to control them.

This collaborative work describes a reverse multiscale modeling approach to reach this goal. Minimalistic CG models were used to study the chemotactic behavior of functionalized supramolecular assemblies on a complementary surface. Instead of using hypothetical examples, these models focused on a realistic example of trimer-based supramolecular assemblies developed within our group. Specifically, this chapter focuses on the interaction outcome of supramolecular assemblies when it comes in contact in a complementary surface. These computational studies were also supported by various experimental techniques such as super-resolution microscopy, AFM and contact angle studies to obtain more insight into the binding interaction process. This combined multiscale approach offers a flexible platform toward the rational design of assembled structures with programmable autonomous chemotactic properties.

4.2 EXPERIMENTAL

4.2.1 MATERIALS:

All reagents were obtained from commercial sources and used as received without further purification. Poly-L-lysine coated glass slides were purchased from Thermo Scientific. Reagents for the synthesis of various trimers can be obtained from the dissertation work by Dr. Manisha Shivrayan, UMass-Amherst.[28]

4.2.2 INSTRUMENTAL:

^{1}H and ^{13}C NMR spectra of synthesized molecules were recorded on a Bruker DPX-400 MHz calibrated against trimethylsilyl (TMS) standard. Dynamic light scattering (DLS) measurements were performed on a Malvern Nanozetasizer-ZS operating at 633 nm. Structural Illumination Super-Resolution Microscopy studies were performed on a Nikon A1R-SIMe. Contact angle measurements were performed on a Attension Theta from Biolin Scientific contact angle goniometer. AFM studies were done on a Jupiter XR AFM instrument (Oxford Instruments/Asylum Research)

4.2.3 METHODS

a. Simulations and computational models:

All simulations were conducted using GROMACS 2018.6[49,50] patched with PLUMED 2.5[51]. The VMD visualization suite was used to display and render the simulated systems. Details on the various parameters used for building computational models and simulation runs have been outlined in detail by Pavan et al.[29]

b. Synthesis of trimers

The structures of 1, 2 and 3 COOH trimers used are in Figure 4.2. Synthetic protocols used to synthesize these trimers can be obtained from the dissertation work by Dr. Manisha Shivrayan, UMass-Amherst.[28]

c. General formulation of trimer micellar assemblies

1 mg/mL solutions of trimers were used in all experiments unless otherwise noted. 1 mg of either 1, 2 or 3 COOH trimers were first dissolved in 100 μL acetone in a glass vial. To this, 1 mL DI water was added dropwise under continuous stirring. The vial was left uncapped overnight with constant stirring to allow the evaporation of acetone. Trimer solutions were recovered the following day for further use.

d. Structural Illumination Microscopy (SIM)

The quantification and rearrangement of trimeric assemblies on positively charged polylysine surfaces was carried out via Structural Illumination Microscopy (SIM). First, 1 mg of either 1, 2 or 3 COOH trimer was dissolved in 100 μL acetone. To this, a 1 mg/mL solution of DiD (1,1'-Dioctadecyl-3,3,3',3'-Tetramethylindodicarbocyanine4-Chlorobenzenesulfonate Salt) was loaded at 10 v/v%. 1 mL DI water was then added dropwise and stirred overnight to obtain trimeric assemblies dispersed in water and non-covalently encapsulating DiD dye. Solutions of the trimeric assemblies were then diluted to 0.05 mg/mL for SIM experiments. For experiments with SIM, a glass chamber setup was fabricated. Briefly, two pieces of clear double-sided tape of dimensions 1 cm x 3cm x 70 μm were placed on the poly-L-lysine functionalized glass slide 1 cm

apart. A coverslip was then placed over the double-sided tape to form a thin chamber. For all experiments with SIM, 20 μL of the solution containing trimeric assemblies were injected into the glass chamber and the chamber washed 3X with 50 μL DI water to flush out any assemblies that were not bound to the polylysine surface. The assemblies were excited with a 640 nm laser to obtain a fluorescence signal from the encapsulated DiD to enable visualization of adhered assemblies on the surface. Captured images were then used to determine extent of particle binding on the polylysine surface and for quantification.

e. Dynamic Light Scattering (DLS) and zeta potential measurements:

Dynamic Light Scattering (DLS) experiments to obtain particle size were performed by diluting 50 μL of the trimer nanoparticle solutions to 1 mL in a cuvette. The size and charge of the trimeric nanoparticles was determined via dynamic light scattering (DLS).

f. Contact angle studies:

Contact angle studies were performed on polylysine coated glass slides to determine the extent of interaction of the trimer nanoparticles based on charge. For these, 1 mg/mL solutions of 1, 2 and 3 COOH in DI water were used. Studies were performed in the static mode, where the contact angle was determined by slowing dropping 5 μL of the trimer solution on the surface of the polylysine glass slide.

g. AFM studies

AFM studies were done in the AC mode. AC40 tips with a spring constant of 0.07-0.14 N/m, and which can operate between 17-55 kHz were used. The actual drive frequency was 29 kHz due to damping effects from immersing the tip in an aqueous sample.

4.3 RESULTS AND DISCUSSION

The ability to track and monitor the dynamic behavior of soft assemblies on receptor-displaying surfaces is crucial to design and develop supramolecular nanoparticles with chemotactic abilities. We start by considering a supramolecular nanoparticle possessing surface ligands composed of self-assembled units, which can establish specific interactions with a complementary functionalized surface (Figure 4.1b). It is hypothesized that the fate of an individual nanoparticle upon surface adhesion will depend on the strength of between the self-assembled units in the assembly (E_{ass}) compared to the strength of multivalent interactions on the complementary surface (E_{bind}). While the former governs the stability of the assembly, the latter relates to the strength of specific interactions between the surface ligands present on the nanoparticle and the complementary receptors on the surface. E_{bind} would also depend on the possibility to establish multivalent interactions involving multiple groups at the same time, which is based on the density of the groups on the nanoparticle and surface. Self-assembled polymeric nanoparticles and micelles are far from behaving as rigid spheres. Being soft entities, they can deform upon interaction on a surface to establish multiple contacts, thereby enlarging the contact area (Figure 1b). The interplay between E_{ass} and E_{bind} would produce different scenarios upon nanoparticle binding to the surface and the outcomes may be presented as (i) rigid adhesion for $E_{ass} >> E_{bind}$, where nanoparticle binding has a negligible effect on nanoparticle integrity (ii) a soft adhesion

accompanied by nanoparticle deformation (for $E_{ass} \sim E_{bind}$), or (iii) disassembly of the nanoparticle after surface interaction (for $E_{ass} << E_{bind}$).

To study the nature of interaction of these supramolecular assemblies based on E_{ass} and E_{bind}, and to predict interaction outcomes, coarse-grained (CG) minimalistic molecular models were used (e.g., Figure 4.1c). Specifically, self-assembling trimers were used for these models. The trimers contain hydrophobic decyl chains and hydrophilic polyethylene glycol moieties, and contain either 1, 2 or 3 carboxylic acid units per amphiphilic unit (Figure 4.2).

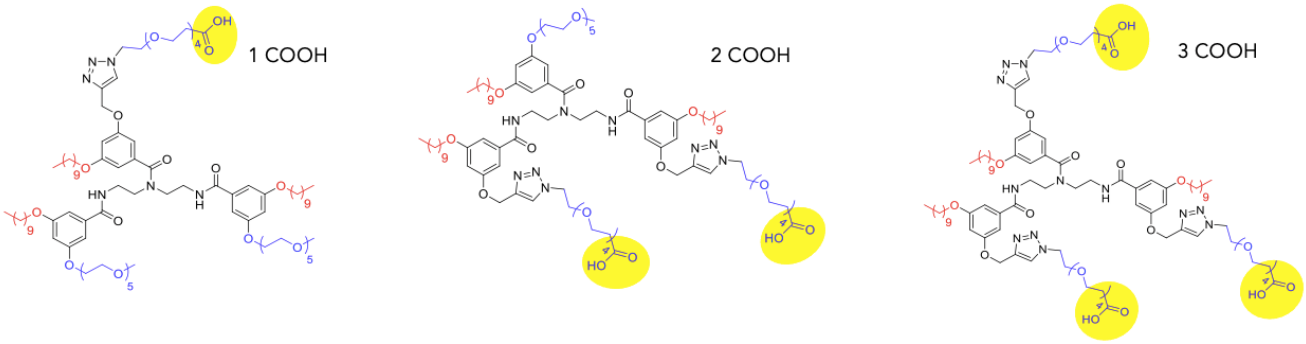

FIGURE 4.2: Structures of trimers used in this work

Due to their amphiphilic nature, these trimers self-assemble as micellar nanoparticles with various densities of the carboxylic acid (-COOH) functionality being exposed on the surface. For computational models, the amphiphilic units carrying 1, 2 or 3 $-COO^-$ were designated charges of -1e, -2e and -3e respectively per unit. Following this, all atom (AA) models were developed for these amphiphilic units. The behavior of individual amphiphiles in aqueous solution were first characterized via AA-MetaD simulations, followed by the amphiphile-amphiphile dimerization free-energy to estimate the strength of the interactions between the amphiphiles in solution (details can be obtained from the work done by Pavan et al.[29]). With this implicit-solvent fine CG model, a nanoparticle model could be generated, each of which composed 44 amphiphilic units. These

self-assembled nanoparticles. Also spontaneously sequestered and encapsulated 10 CG guest beads (Figure 4.3b, violet) during a CG-MetaD simulation. A model of a flat surface decorated

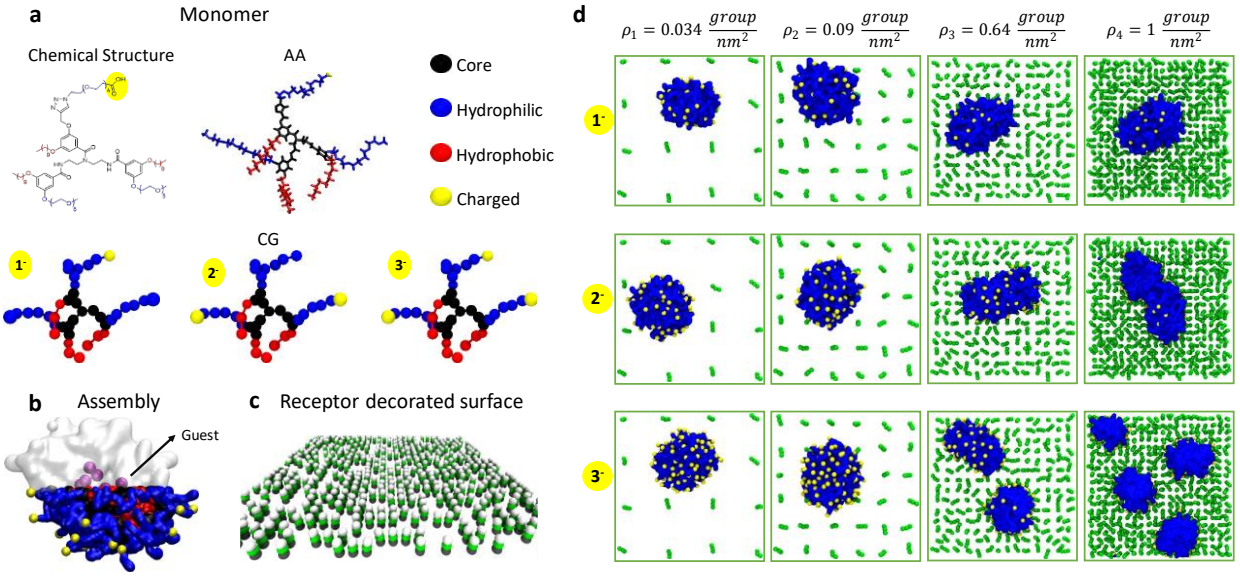

FIGURE 4.3. Submolecular-resolution CG models to study self-assembled NPs and their adhesion onto functionalized surfaces. a) Chemical structure, all-atom (AA) and fine coarse-grained (CG) models of facially amphiphilic modular dendrons. These self-assembling units are composed of a branched core (in black), hydrophobic groups (red) which triggers self-assembly in aqueous solution, and hydrophilic groups (red), which can be functionalized in different ways (i.e. with COO^- charged groups, in yellow, in the example studied herein). b) Fine CG model of a NP obtained via self-assembly of 44 dendrons in water. Guest CG particles (in purple) are incapsulated spontaneously in the NP, and used to monitor guest release upon eventual NP disassembly. c) CG model of a surface functionalized with $+1e$ charged groups (dark green CG beads are constrained in their position, while the topmost white ones carry a $+1e$ charge. d) CG-MD simulation of static NP adhesion to surfaces characterized by different densities of receptor groups. Snaphots taken after 1 μs of CG-MD showing NP destabilization and disassembly upon adhesion may be observed while increasing the charge densities on the surface and on the NP. (figure obtained from reference 29).

with positively charged CG receptor groups was also developed. In this, the receptor groups were modeled as 3 CG beads, where the bottom one is constrained in its position, and the topmost one is +1*e* charged (Figure 4.3c). Four surface densities were also modeled (ρ_1, ρ_2, ρ_3, ρ_4), up to a maximum density of ρ_4 = 1 positively charged-group per nm^2 (Figure 4.3d), in the order of experimentally reported density values for amino-grafted surfaces.[44–47] These CG models were used to study the nanoparticle adhesion on the surface. In particular, the behavior of the nanoparticle following the adhesion process was studied. CG-MetaD simulations of NPs composed of dendrons bearing 1, 2 or 3 COO^- charged groups carried a total nanoparticle charge of -44*e*, -88*e* and -132*e* respectively. On binding to the surface with increasing densities of receptor groups (Figure 3d: from ρ_1 to ρ_4), it was observed that the behavior of the NP upon binding is strictly related to the strength of the multivalent nanoparticle-surface interactions. This was dependent on the density of charges present on the target surface, ρ, and those presented on the nanoparticle surface due to varying numbers of COO^- charged groups. When the contacts are established between the nanoparticle carrying 132 negative charge units and the surface of density ρ_4, simulations predict disassembly of the charged nanoparticle. Complete details on the parametrization of the AA and CG models can be obtained by referring to the work done by Pavan et al.[29]

To determine the nanoparticle interaction outcome and to test the validity of the theoretical models, experimental studies were also carried out using super-resolution microscopy, AFM and contact angle measurements. To carry out experimental studies, the trimer-based self-assemblies were formulated in an aqueous solution at neutral pH. Under these conditions, the -COOH moieties exist as carboxylate ions (-COO-), and zeta potentials of these self-assembled nanoparticles were determined experimentally. 1, 2 and 3 COOH trimer nanoparticles possessed similar

hydrodynamic radii of ~ 200 nm (Figure 4.4), and the charge was found to be decreasing with the increase in the number of COOH functional groups. Nanoparticles were found to possess increasing negative zeta potentials of -20, -40 and -60 mV, based on the numbers of -COO^- the trimers carried (Figure 4.5).

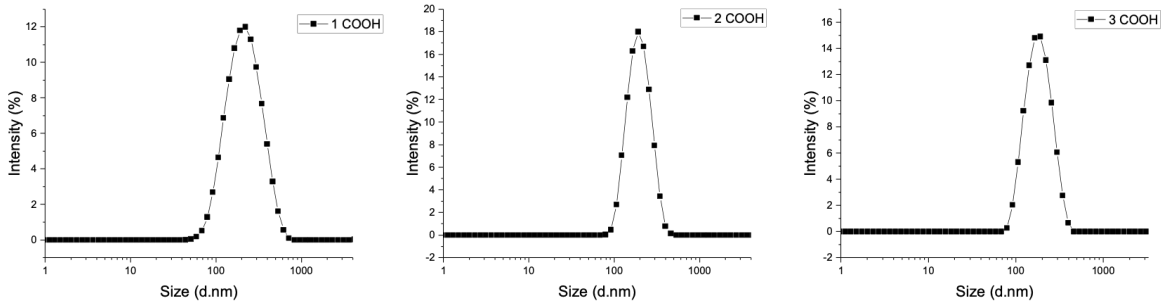

FIGURE 4.4: DLS plot of 1, 2 and 3 COOH trimers

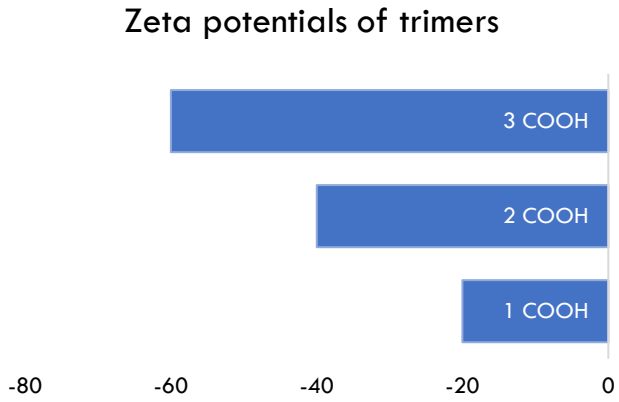

FIGURE 4.5: Zeta potentials of 1, 2 and 3 COOH trimeric assemblies showing surface charge.

Preliminary adhesion studies with 1, 2 or 3-COOH nanoparticles were carried out by using a positively charged surface in the form of poly-L-lysine coated glass slides. After injection onto the functionalized slides, super-resolution microscopy revealed the presence of various amounts of particles on the surface as evidenced in the microscopy images (Figure 4.5). Quantification studies

were also carried out, it was apparent that there was a correlation between the number of nanoparticles bound to the surface and surface charge it carried. In these experimental studies, the following trend was observed on binding as a function of charge 1-COO^- > 2-COO^- > 3-COO^-.

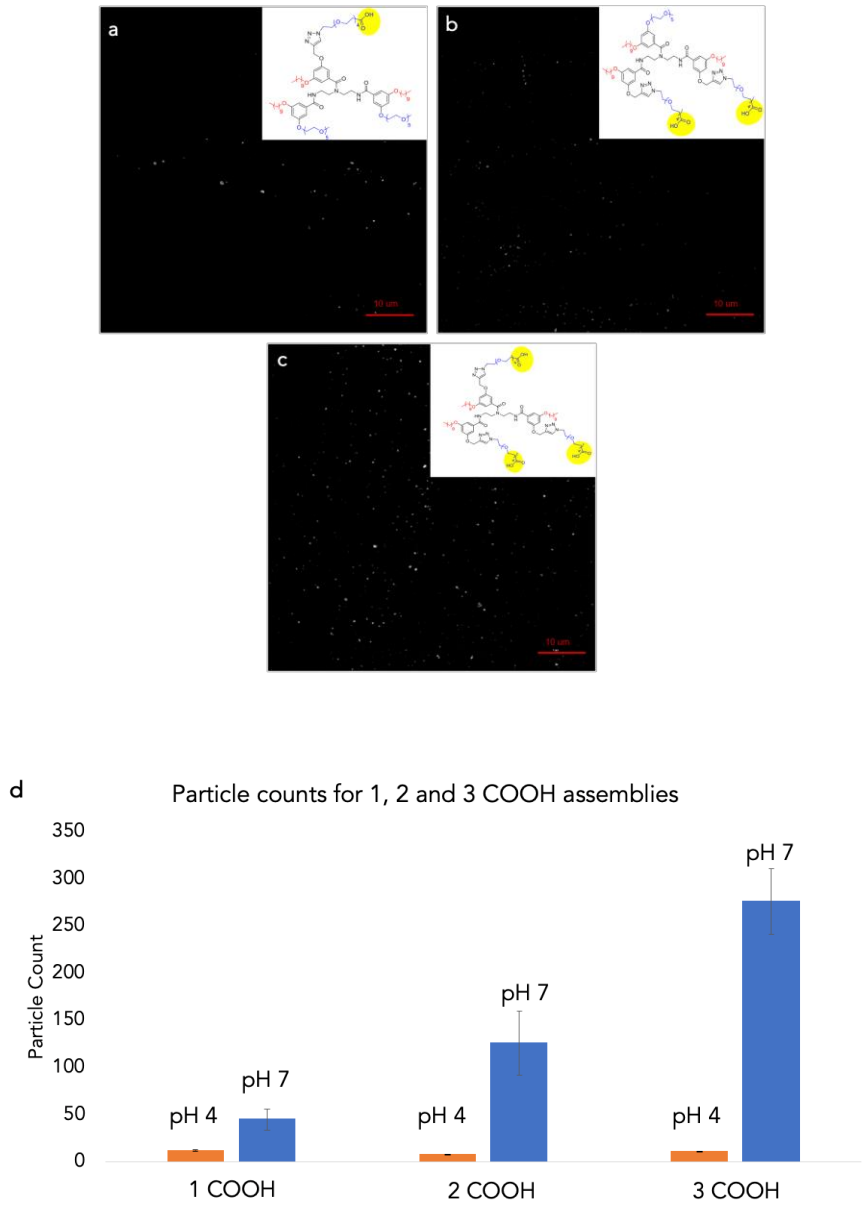

FIGURE 4.6**:** Quantification of nanoparticle binding. a) Micrographs of polylysine surfaces qualitatively showing the extent of 1, 2 and 3 COOH binding on polyysine surfaces; b) Average numbers of particles bound on the polylysine surface. Quantitation was performed on the micrographs using Nikon Elements. Scalebar = 1 µm

To determine the extent of adhesion, and possible disassembly of the micelles on the polylysine surface, AFM measurements were also carried out. The hypothesis is as follows: since the trimer-base nanoparticles are soft, they are prone to deformation upon establishing multivalent contacts on a complementary surface. The extent of deformation on a positively charged surface would also be dependent on amount of negative surface charge that a nanoparticle carries, and as a result, a variation in particle height should be observed after interaction. Based on this hypothesis, the 3-COO- nanoparticles should show the largest extent of deformation on the poly-L-lysine surface since they carry the highest negative charge. AFM experiments revealed that there was a change in average height of the nanoparticles based on the negative surface charge they carried (Figure 4.6). Although all trimer assemblies were of the same size initially, there was a gradual decrease in height of the assemblies and followed the trend 1-COO^- > 2-COO^- > 3COO^- with average height values of ~ 12 nm, 8 nm, and 4 nm respectively. The difference in height profiles suggests that the assemblies can deform due to their soft nature while in contact with the charged surface. The extent of deformation is consistent with the extent of negative charge they carried.

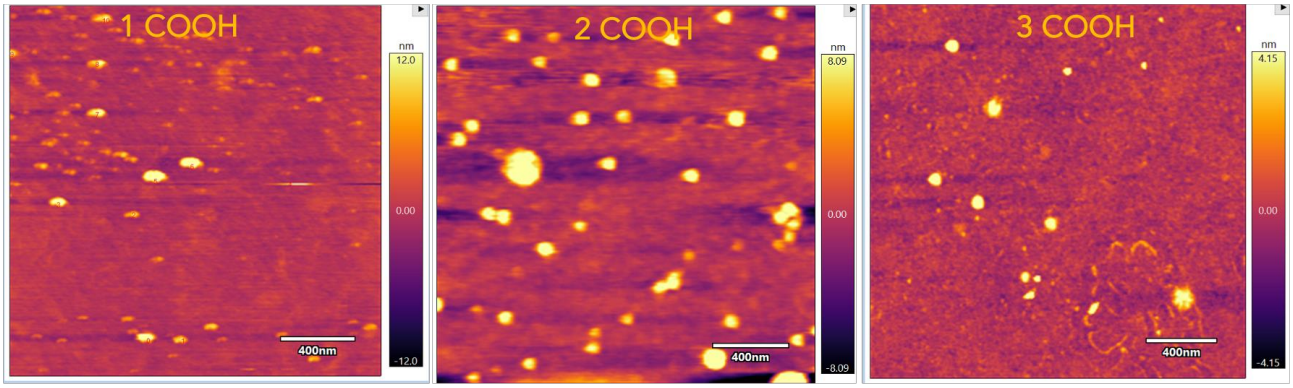

FIGURE 4.7: AFM height measurements showing the average heights of the particles on the polylysine surface.

Contact angle measurements were also carried out to test if nanoparticles carrying higher negative surface charge disassembled on the positively charged poly-L-lysine slide. It is hypothesized that the contact angles on a positively charged surface should be less than 90 degrees and the contact angles should decrease as 1-COO^- < 2-COO^- < 3COO^- due to the zeta potential trend they exhibit. However, if the nanoparticles disassemble on the surface, the contact angle should transition from being less than 90 degrees to greater than 90 degrees since disassembly would reveal the hydrophobic decyl chains of the trimer units. Contact angles studies show a decrease in contact angles with an increase in negative surface charge, however, no disassembly was detected since all the angles remained less than 90 degrees (Figure 4.8).

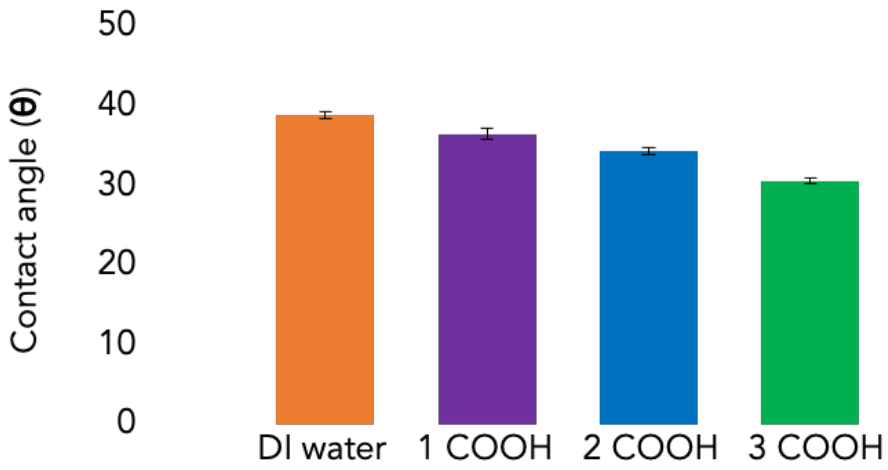

FIGURE 4.8: Contact angles of the various trimer assemblies compared with the contact angle obtained for DI water.

4.4 CONCLUSIONS:

In this work we have designed a concerted computational strategy to investigate supramolecular NPs with interesting chemotactic and density-responsive bioinspired properties. We have used a combination of multiscale molecular models and advanced simulation approaches to track, monitor, and ultimately to understand the dynamic behavior of the self-assembled nanoparticles on receptor-grafted surfaces. Moving from minimalistic to finer coarse grain models, we uncover the physical basis that control the chemotactic behavior of the nanoparticle. We demonstrate the key role played by the competition between the self-assembly stability of the nanoparticle (E_{ass}) and the strength of the interaction between the nanoparticle and the surface (E_{bind}). Such E_{ass} *vs.* E_{bind} competition controls the autonomous motion of the nanoparticle along chemical gradients (as in the absence of the motion would be Brownian) and the fate of the nanoparticle. Using soft nanoparticles made of modular self-assembling multivalent dendrons as an example case study, we provide chemical relevance to our results, showing chemical routes to achieve controlled bioinspired chemotaxis in artificial self-assembled systems. By tuning the nanoparticle surface charge and the chemical structure of the monomer units (e.g. the nature of the hydrophobic groups in the self-assembling dendrons) it would be possible in principle to control how the nanoparticle binds to the surface, its spontaneous diffusion following chemical gradients, its rolling, stopping, and, in the case of an external stimulus (i.e. a flux), even nanoparticles disassembly and guest-release in controlled spots of the surface. The results discussed herein suggest that such *in silico* experiments can be extremely valuable for augmenting our understanding of how to customize the structure of the self-assembling units to control the stability of the NP, the E_{bind}/E_{ass} balance, and the dynamic behavior and fate of these chemotactic NPs. Furthermore, we show that it is in principle possible, once the features of a target surface are

known, to rationally design or customize *ad hoc* the NPs to achieve controllable chemotaxis in artificial molecular systems.

4.5 REFERENCES:

1. de Oliveira, S.; Rosowski, E. E.; Huttenlocher, A. Neutrophil Migration in Infection and Wound Repair: Going Forward in Reverse. *Nat. Rev. Immunol.*, **2016**, *16*, 378-291.
2. Stuelten, C. H.; Parent, C. A.; Montell, D. J. Cell Motility in Cancer Invasion and Metastasis: Insights from Simple Model Organisms. *Nat. Rev. Cancer*. **2018***, 18*, 296-312.
3. Trepat, X.; Wasserman, M.; Angelini, T.; Millet, E.; Weltz, D. A.; Butler, J. P.; Fredberg, J. J. Physical Forces during Collective Cell Migration. *Nat. Phys.,* **2009**, *5*, 426-430.
4. Tambe, D. T.; Corey Hardin, C.; Angelini, T. E.; Rajendran, K.; Park, C. Y.; Serra-Picamal, X.; Zhou, E. H.; Zaman, M. H.; Butler, J. P.; Weitz, D. A.; Fredberg, J. J.; Trepat, X. Collective Cell Guidance by Cooperative Intercellular Forces. *Nat. Mater.* **2011**, *10*, 469–475.
5. Roca-Cusachs, P.; Sunyer, R.; Trepat, X. Mechanical Guidance of Cell Migration: Lessons from Chemotaxis. *Curr. Opin*. *Cell Biol.*, **2013**, *25*, 543-549.
6. Datta, S.; Kato, Y.; Higashiharaguchi, S.; Aratsu, K.; Isobe, A.; Saito, T.; Prabhu, D. D.; Kitamoto, Y.; Hollamby, M. J.; Smith, A. J.; et al. Self-Assembled Poly-Catenanes from Supramolecular Toroidal Building Blocks. *Nature*, **2020**, *583*, 400–405.
7. Mishra, A.; Dhiman, S.; George, S. J. ATP-Driven Synthetic Supramolecular Assemblies: From ATP as a Template to Fuel. *Angew. Chem. Int. Ed.*, **2021**, *60,* 2740-2756.
8. Yan, X.; Wang, F.; Zheng, B.; Huang, F. Stimuli-Responsive Supramolecular Polymeric Materials. *Chem. Soc. Rev.,* **2012**, *41*, 6042-6065

9. Aida, T.; Meijer, E. W.; Stupp, S. I. Functional Supramolecular Polymers. *Science*, **2012**, *17*, 813-817.

10. Xu, F.; Pfeifer, L.; Crespi, S.; Leung, F. K.-C.; Stuart, M. C. A.; Wezenberg, S. J.; Feringa, B. L. From Photoinduced Supramolecular Polymerization to Responsive Organogels. *J. Am. Chem. Soc.* **2021**, *143*, 5990–5997.

11. Bochicchio, D.; Kwangmettatam, S.; Kudernac, T.; Pavan, G. M. How Defects Control the Out-of-Equilibrium Dissipative Evolution of a Supramolecular Tubule. *ACS Nano* **2019**, *13*, 4322–4334.

12. Roy, I.; Bobbala, S.; Young, R. M.; Beldjoudi, Y.; Nguyen, M. T.; Cetin, M. M.; Cooper, J. A.; Allen, S.; Anamimoghadam, O.; Scott, E. A.; et al. A Supramolecular Approach for Modulated Photoprotection, Lysosomal Delivery, and Photodynamic Activity of a Photosensitizer. *J. Am. Chem. Soc.* **2019**, *141*, 12296–12304.

13. Amado Torres, D.; Garzoni, M.; Subrahmanyam, A. V.; Pavan, G. M.; Thayumanavan, S. Protein-Triggered Supramolecular Disassembly: Insights Based on Variations in Ligand Location in Amphiphilic Dendrons. *J. Am. Chem. Soc.* **2014**, *136*, 5385–5399.

14. Zarzar, L. D.; Aizenberg, J. Stimuli-Responsive Chemomechanical Actuation: A Hybrid Materials Approach. *Acc. Chem. Res.* **2014**, *47*, 530-539.

15. Semenov, S. N.; Kraft, L. J.; Ainla, A.; Zhao, M.; Baghbanzadeh, M.; Campbell, V. E.; Kang, K.; Fox, J. M.; Whitesides, G. M. Autocatalytic, Bistable, Oscillatory Networks of Biologically Relevant Organic Reactions. *Nature*, **2016**, *537*, 656-660.

16. Cui, J.; Daniel, D.; Grinthal, A.; Lin, K.; Aizenberg, J. Dynamic Polymer Systems with Self-Regulated Secretion for the Control of Surface Properties and Material Healing. *Nat. Mater.*, **2015**, *14,* 790-795.

17. Liu, J.; Xu, H.; Tang, X.; Xu, J.; Jin, Z.; Li, H.; Wang, S.; Gou, J.; Jin, X. Simple and Tunable Surface Coatings via Polydopamine for Modulating Pharmacokinetics, Cell Uptake and Biodistribution of Polymeric Nanoparticles. *RSC Adv.* **2017**, *7*, 15864–15876.

18. Liao, Y. H.; Lin, C. H.; Cheng, C. Y.; Wong, W. C.; Juo, J. Y.; Hsieh, C. L. Monovalent and Oriented Labeling of Gold Nanoprobes for the High-Resolution Tracking of a Single-Membrane Molecule. *ACS Nano* **2019**, *13*, 10918–10928.

19. Di Iorio, D.; Huskens, J. Surface Modification with Control over Ligand Density for the Study of Multivalent Biological Systems. *ChemistryOpen*, **2020**, *9*, 53-66.

20. Yue, Y.; Gao, Y.; Yu, Y. "Waltz" of Cell Membrane-Coated Nanoparticles on Lipid Bilayers: Tracking Single Particle Rotation in Ligand-Receptor Binding. *ACS Nano* **2018**, *12*, 11871–11880.

21. Taylor, R. W.; Mahmoodabadi, R. G.; Rauschenberger, V.; Giessl, A.; Schambony, A.; Sandoghdar, V. Interferometric Scattering Microscopy Reveals Microsecond Nanoscopic Protein Motion on a Live Cell Membrane. *Nat. Photonics*, **2019**, *13*, 480-487.

22. Wang, M.; Ravindranath, S. R.; Rahim, M. K.; Botvinick, E. L.; Haun, J. B. Evolution of Multivalent Nanoparticle Adhesion via Specific Molecular Interactions. *Langmuir*, **2016**, *32***,** 13124-13136**.**

23. Lin, L.; Zeng, X. Computational Study of Cell Adhesion and Rolling in Flow Channel by Meshfree Method. *Comput. Methods Biomech. Biomed. Engin.,* **2017**, *20,* 832-841.

24. Arya, G.; Panagiotopoulos, A. Z. Log-Rolling Micelles in Sheared Amphiphilic Thin Films. *Phys. Rev. Lett.,* **2005**, *95,* 18801-18804**.**

25. Curk, T.; Dobnikar, J.; Frenkel, D. Optimal Multivalent Targeting of Membranes with Many Distinct Receptors. *Proc. Natl. Acad. Sci.*, **2017**, *114*, 7210-7215**.**

26. Molla, M. R.; Rangadurai, P.; Pavan, G. M.; Thayumanavan, S. Experimental and Theoretical Investigations in Stimuli Responsive Dendrimer-Based Assemblies. *Nanoscale*. **2015**, *7*, 3817-3837.

27. Torchi, A.; Bochicchio, D.; Pavan, G. M. How the Dynamics of a Supramolecular Polymer Determines Its Dynamic Adaptivity and Stimuli-Responsiveness: Structure-Dynamics-Property Relationships from Coarse-Grained Simulations. *J. Phys. Chem. B,* **2018**, *122*, 4169-4178.

28. Shivrayan, S. Design of Responsive Oligomeric and Polymeric Interfaces for Sensing and Controlled Release Applications. Ph.D. Dissertation, University of Massachusetts-Amherst, Amherst, MA, 2021.

29. Lionello, C.; Gardin, A.; Cardellini, A.; Bochicchio, D.; Shivrayan, M.; Fernandez, A.; Thayumanavan, S.; Pavan, G. M. Politecnico di Torino. Unpublished work, **2021**.

CHAPTER 5

5.1 SUMMARY

The work in this thesis was inspired by different autonomous processes in Nature to fundamentally study various structural and energetic changes that underlie self-regulated processes at the molecular level. The understanding of concepts and molecular mechanisms driving different functions can promote the development of intelligent devices that can actively adapt and interact as complex molecular systems.

In Chapter 2, covalently triggerable surfactants were designed using the TMAc platform. TMAc surfactants were designed to stabilize interfaces of single and double emulsions and were tailored to respond to nucleophilic stimuli. Our results demonstrate how these designer surfactants, after successful incorporation into single emulsions and dynamic double emulsions, enable them to respond to thiol or amine small molecule nucleophiles, polyvalent particles, or induce release of reactants from photoactivated capsules. These surfactants, in addition to being trigger selective, also demonstrated kinetic tunability. We were also able to achieve direct polyvalent assembly-assembly contact that initiated covalent surface modifications in both reactive-surfactant stabilized emulsion systems. Through the integration of light sensitive polymerosomes based on azobenzene that exhibits non-equilibrium behavior, in *situ* on demand release of a small molecule trigger and subsequent morphological changes were also obtained in the emulsion system, thereby offering another method for system tunability. Although not as intricate and highly evolved, our system in many ways resembles the molecular recognition and interaction processes seen in biological systems. We also demonstrated non-biological implications through the application in the triggered formation of PU foam, which is reminiscent of the conversion of microscopic events into macroscopically observable phenomena commonly seen in biological processes.

In Chapter 3, a simplistic membrane model was used to explore the effects of receptor mediated non-covalent nanoparticle binding on membrane morphology and integrity. A systematic analysis of the effect of nanoparticle size, receptor coverage on the membrane, ligand density and overall receptor-ligand concentration ratios. It was seen that the sulfonamide-based particles were able to induce adhesion between the GUVs, and adhesion strength could be quantitatively determined my measuring the values of contact angles between the GUVs. We observed that these overall angles increased as particle size increased and, showed a variation depending on receptor and ligand surface coverages for each nanoparticle size. We also estimated an approximate work of adhesion value for these experiments to be in the range of 0 – 3.55 mJ/m^2. This platform is easily tunable for any receptor-ligand pair and may be extended to study other aspects of membrane-mediated processes. From these studies, we observe membrane destabilization at ~ 1.58 mJ/m^2. This fundamental study would be useful in determining the threshold ligand concentration based on the unique receptor densities seen on cells to design nanoparticles capable of interacting specifically with surface cell receptors. Such a strategy would eliminate nanoparticle-induced cytotoxicity in drug delivery studies. In addition, the triggered rupture of GUVs seen at high receptor/ligand concentration can be made of for developing membrane-based controlled delivery systems with implications in self-healing and controlled polymerization applications.

Chapter 4 focused on the design of a concerted computational strategy to investigate the development of supramolecular assemblies with chemotactic and density-responsive bioinspired properties. A multiscale approach was utilized with advanced simulation techniques to track, monitor, and ultimately to understand the dynamic behavior of the self-assembled particles on receptor-grafted surfaces. It was demonstrated that the competition between the energy that holds the self-assembly together and the strength of the interaction between the self-assembly and the

surface dictated the outcome and fate of the assembly after interaction with a surface. We also provided chemical relevance to our results, by using self-assembling oligomers, showing potential chemical routes to achieve controlled bioinspired chemotaxis in artificial self-assembled systems. These results show how in principle, it would be possible to control the binding process of a nanoparticle on a complementary surface, and enable its spontaneous diffusion along a gradient, to facilitate nanoparticle disassembly and guest-release in controlled spots of the surface.

5.2 FUTURE DIRECTIONS:

GUVs models to understand exocytosis

GUVs, due to their ability to serve as artificial cell models, can be used to study more about the process of exocytosis of nanoparticles. Exocytosis can occur via two different modes – full fusion or partial release[1-4]. It would be possible to understand which of these modes are favored by altering GUV lipid composition, by using lipids of varying charge and head group volumes to alter membrane tension[5-7]. It is reasonable to assume that the bending modulus on the lipid compositions would greatly influence the mechanism by which contents are released from the interior of a cellular compartment. It would also be possible to incorporate different proteins of interest on the GUV surface to identify if a combination of membrane composition and surface proteins influence the overall process of exocytosis. It would also be useful to quantify what percentage of the contents are released due to exocytosis. These findings may be helpful to identify how exocytosis plays a role in chemical signal messaging and cell-cell communication[8-9].

GUVs models to understand receptor clustering

GUVs are robust models to study several biological functions pertinent to the cell membrane. In Chapter 3, we used protein-ligand interactions to study how nanoparticle size, rigidity, receptor/ligand density and distribution all play a role in inducing membrane morphology change by using a well-known interaction between carbonic anhydrase and a sulfonamide ligand to study these changes. This GUV platform is easily customizable to incorporate other membrane receptors, and subsequently study other interactions that are not well understood. A continuation of this work could focus on understanding receptor clustering on the cell surface to obtain insight into the mechanism that cells use to change and adapt their affinity towards ligands[10-13]. For example, with T-cell receptors, it would be possible to better understand and explain the difference between naive and memory T-cell response due to pre-clustering of the receptors using simple GUV models[14-16].

Computational studies for the rational design of protein surfaces to enable chemotaxis

The results obtained in Chapter 4 suggests that *in silico* experiments can be extremely valuable for developing design guidelines on the structure of the self-assembling units to control the stability and dynamic behavior of a nanoparticle while interacting with a surface. Once the features of a target surface are determined, it would also be possible to rationally design or customize nanoparticles to enable chemotaxis in artificial molecular systems.[17-19] This could bring us closer to designing functional mimics that are able to recognize user-defined antigen signatures. It would also be useful to use these methods to assess how protein complexes can be developed to bind to cell subsets with increased specificity. By using a logic-gated approach via a combination of various non-covalent interactions seen in biological systems, a deeper

understanding of underlying principles of tissues and systems comprising multiple cell types can be obtained, which may be key in understanding the progression of complex diseases.

5.3 REFERENCES:

1. Mellander, L. J. Kurczy, M. E.; Majafinobar, N.; Dunavall, J.; Ewing, A. G.; Cans, A.-S. Two Modes of Exocytosis in an Artificial Cell. *Sci. Rep.,* **2014**, *4,* 3847-3856.
2. Wu, L. G.; Hamid, E.; Shin, W. Chiang, H. C. Exocytosis and Endocytosis: Modes, Functions, and Coupling Mechanisms. *Annu. Rev. Physiol.* **2014**, *76,* 301-331.
3. Martin, T. F. J. Tuning Exocytosis for Speed: Fast and Slow Modes. *Biochim. Biophys. Acta.,* **2003**, *1641*, 157.
4. Ren, L.; Mellander, L.; Keighron, J.; Cans, A.-S.; Kurczy, M. E.; Svir, I.; Oleinick, A.; Amatore, C.; Ewing, A. G. The Evidence for Open and Closed Exocytosis as the Primary Release Mechanism. *Q. Rev. Biophys*., **2016**, *49*, e12-e28.
5. Reddy, A. S.; Warshavaik, D. T.; Chachisvillis, M. Effect of Membrane Tension on the Physical Properties of DOPC Lipid Bilayer Membrane. *Biochim. Biophys. Acta.,* **2012**, *1818*, 2271-2281.
6. Sreekumari, A.; Lipowsky, R. Lipids with Bulky Head Groups Generate Large Membrane Curvatures by Small Compositional Asymmetries. *J. Chem. Phys.,* **2018**, *149*, 084901-084915.
7. Anishkin, A.; Loukin, S. H.; Jifareng, J.; Kung, C. Feeling the Hidden Mechanical Forces in Lipid Bilayer is an Original Sense. *Proc. Natl. Acad. Sci. U.S.A.,* **2014**, *22*, 7898-7905.
8. Gucek, A.; Vardjan, N.; Zorec, R. Exocytosis in Astrocytes: Transmitter Release and Membrane Signal Regulation. *Neurochem. Res.*, **2012**, *37*, 2351-2363.

9. Bezzi, P.; Gundersen, V.; Galbete, J. L.; Seifert, G.; Steinhauser, C.; Pilati, E.; Volterra, A. Astrocytes contain a Vesicular Compartment that is Competent for Regulated Exocytosis of Glutamate. *Nat. Neurosci.*, **2004**, *7*, 613-620.
10. Fenz, S. F.; Smith, A.-S.; Merkel, R.; Sengupta, K. Inter-Membrane Adhesion Mediated by Mobile Linkers: Effect of Receptor Shortage. *Soft Matter*, **2011**, *7*, 952-962.
11. Glazier, R. Salaita, K. Supported Lipid Bilayer Platforms To probe Cell Mechanobiology. *Biochim. Biophys. Acta.,* **2017**, *1859*, 1465-1482.
12. Feng, Z.; Wu, X.; Zhang, M. Presynaptic Bouton Compartmentalization and Postsynaptic Density-Mediated Glutamate Receptor Clustering via Phase Separation. *Neuropharmacol*., **2021**, *183,* 108622- 108631.
13. Barteit, S. M.; Chervyachkova, E.; Ricken, J. Wegner, S. V. Mimicking Adhesion in Minimal Synthetic Cells. *Adv. Biosys.,* **2019**, *3,* 180033-1800342.
14. Germain, R. T-Cell Signaling: The Importance of Receptor Clustering. *Curr. Biol.* **1997**, *7,* 640-644.
15. Krummel, M. F.; Sjaastad, M. D.; Wulfing, C.; Davis, M. M. Differential Clustering of CD4 and CD3 ζ During T cell Recognition. *Science*, **2000**, *289*, 1349-1352.
16. Minguet, S.; Swamy, M.; Alarcon, B.; Luescher, I. F. Schamel W. W. A. Full Activation of the T Cell Receptor Requires Both Clustering and Conformational Changes at CD3. *Immunity*, **2007**, *26*, 43-54.
17. Codrean, M. T.; Lauga, E.; Artificial Chemotaxis of Phoretic Swimmers: Instantaneous and Long-Time Behavior. *J. Fluid. Mech*., **2018**, *856*, 921-957.

18. Lagzi, I. Chemical Robotics – Chemotactic Drug Carriers. *Cent. Eur. J. Med*., **2013**, *2*, 377-382.

19. Baraban, L.; Harazim, S. M. Sanchez, S.; Schmidt, O. G. Chemotactic Behavior of Catalytic Motors in Microfluidic Channels. *Angew. Chem*., **2013**, *125*, 5662-5666.

BIBLIOGRAPHY

1. An, Y.; Chem, M.; Xue, Q.; Liu, W. Preparation and Self-Assembly of Carboxylic Acid Functionalization. *J. Coll. Interface Sci*., **2007**, *311*, 507-213.

2. Andreasson, J.; Pischel, U. Molecules with a Sense of Logic: A progress Report. *Chem. Soc. Rev.*, **2015**, *44*, 1053-1069.

3. Aida, T.; Meijer, E. W.; Stupp, S. I. Functional Supramolecular Polymers. *Science*, **2012**, *17*, 813-817.

4. Aizenberg, J.; Weaver, J. C.; Thanawala, M. S.; Sundar, V. C.; Morse, D. E.; Skeleton of Euplectella sp.: Structural Hierarchy from the Nanoscale to the Macroscale. *Science*, **2005**, *309,* 275-278.

5. Amado Torres, D.; Garzoni, M.; Subrahmanyam, A. V.; Pavan, G. M.; Thayumanavan, S. Protein-Triggered Supramolecular Disassembly: Insights Based on Variations in Ligand Location in Amphiphilic Dendrons. *J. Am. Chem. Soc.* **2014**, *136*, 5385–5399.

6. Anishkin, A.; Loukin, S. H.; Jifeng, J.; Kung, C. Feeling the Hidden Mechanical Forces in Lipid Bilayer is an Original Sense. *Proc. Natl. Acad. Sci. U.S.A.,* **2014**, *22*, 7898-7905.

7. Arya, G.; Panagiotopoulos, A. Z. Log-Rolling Micelles in Sheared Amphiphilic Thin Films. *Phys. Rev. Lett.,* **2005**, *95,* 18801-18804**.**

8. Asokan, A.; Cho, M. J. Cytosolic Delivery of Macromolecules. 3. Synthesis and Characterization of Acid-Sensitive Bis-Detergents. *Bioconjugate Chem*., **2004**, *15*, 1166−1173.

9. Aviram, A. Molecules for Memory, Logic, and Amplification. *J. Am. Chem. Soc.* **1988,** *110,* 5687-5692.

10. Avrahm, R.; Yarden, Y. Feedback Regulation of EGFR Signaling: Decision Making by Early and Delayed Loops. *Nat. Rev. Mol. Cell Biol.* **2011,** *12,* 104-117.

11. Baraban, L.; Harazim, S. M. Sanchez, S.; Schmidt, O. G. Chemotactic Behavior of Catalytic Motors in Microfluidic Channels. *Angew. Chem*., **2013**, *125*, 5662-5666.

12. Barrow, E.; Nicola, A. V. Multiscale Perspectives of Virus Entry via Endocytosis. *Virol. J.* **2013**, *10,* 177-186.

13. Barteit, S. M.; Chervyachkova, E.; Ricken, J. Wegner, S. V. Mimicking Adhesion in Minimal Synthetic Cells. *Adv. Biosys.,* **2019**, *3,* 180033-1800342.

14. Behzadi, S.; Serphooshan, V.; Tao, W.; Hamaly, M.; Alkawareek, M. Y.; Dreaden, E. C.; Brown, D.; Alkilany, A. M.; Farokhzas, O. C.; Mahmoudi, M. Cellular Uptake of Nanoparticles: Journey Inside the Cell. *Chem. Soc. Rev.* **2017**, *46*, 4218-4244.

15. Bezzi, P.; Gundersen, V.; Galbete, J. L.; Seifert, G.; Steinhauser, C.; Pilati, E.; Volterra, A. Astrocytes contain a Vesicular Compartment that is Competent for Regulated Exocytosis of Glutamate. *Nat. Neurosci.*, **2004**, *7*, 613-620.

16. Bhaskar, S.; Tian, F.; Stoeger, T.; Kreyling, W.; de la Fuente, J. M.; Grazu, V.; Borm, P.; Estrada, G.; Ntziachristos, V.; Razansky, D. Multifunctional Nanocarriers for Diagnostics, Drug Delivery and Targeted Treatment Across Blood-Barrier: Perspectives on Tracking and Neuroimaging. *Part. Fibre Toxicol.,* **2010,** *7,* 1-25.

17. Blum, A. P.; Kammeyer, J. K.; Rush, A. M.; Callmann, C. E.; Hahn, M. E.; Gianneschi, N. C. Stimuli-Responsive Nanomaterial for Biomedical Applications. *J. Am. Chem. Soc.* **2015**, *137*, 2140.

18. Bochicchio, D.; Kwangmettatam, S.; Kudernac, T.; Pavan, G. M. How Defects Control the Out-of-Equilibrium Dissipative Evolution of a Supramolecular Tubule. *ACS Nano* **2019**, *13*, 4322–4334.

19. Brandman, O.; Ferrell, J. E.; Li, R.; Meyer, T. Interlinked Fast and Slow Positive Feedback Loops Drive Reliable Cell Decisions. *Science*, **2005,** *310,* 496-498.

20. Brown, P.; Butts, C. P.; Eastoe, J. Stimuli-Responsive Surfactants. *Soft Matter* **2013**, *9*, 2365−2374.

21. Cao, R.; Kumar, D.; Dinsmore, A. D. Vesicle-based Gel via Polyelectrolyte-Induced Adhesion: Structure, Rheology, and Response. *Langmuir* **2021**, *37*, 1714-1724.

22. Cao, Z.; Wang, G. Multi-Stimuli-Responsive Polymer Materials: Particles, Films, and Bulk Gels. *Chem. Re*c., **2016**, *16*, 1398-1435.

23. Ceschia, E.; Harjani, J. R.; Liang, C.; Ghoshouni, Z.; Andrea, T.; Brown, R. S.; Jessop, P. G. Switchable Anionic Surfactants for the Remediation of Oil-Contaminated Sand by Soil Washing. RSC Adv., **2014**, *4*, 4638−4645.Charitou, T.; Bryan, K.; Lynn, D. J. Using Biological Networks to Integrate, Visualize and Analyze Genomics Data. *Gen. Sel. Evol*. **2016**, *48*, 27-38.

24. Clark, R.; Judd, J.; Lasek-Nesselquist, E.; Montgomery, S.A.; Hoffmann, J. G.; Derbyshire, K. M.; Gray, T. A. Direct Cell-cell Contact Activates SigN to Express the ESX-4 Secretion System in *Mycobacterium smegmatis*. *PNAS.* **2018,** *115*, 6595-6603.

25. Chen, K. L.; Bothun, G. D. Nanoparticles Meet Cell Membranes: Probing Non-specific Interaction Using Model Membranes. *Environ. Sci. Tech*. **2014**, *48*, 873-880.

26. Cheng, C.; McGoniga, P. R.; Stoddary, J. F; Astumian, R. D. Design and Synthesis of Non-Equilibrium Systems. Design and Synthesis of Non-Equilibrium Systems. *ACS Nano.* **2015,** *9,* 8672-8688.

27. Claudia, C.; Schneemilch, M.; Gaisofrd, S.; Quirke, N. Nanoparticle-Membrane Interactions. *J. Exp. Nanosci.* **2018**, *13*, 62-81.

28. Codrean, M. T.; Lauga, E.; Artificial Chemotaxis of Phoretic Swimmers: Instantaneous and Long-Time Behavior. *J. Fluid. Mech*., **2018**, *856*, 921-957.

29. Colberg, P. H.; Reigh, S. Y.; Robertson, B.; Kapral, R. Chemistry in Motion: Tiny Synthetic Motors. *Acc. Chem. Res.* **2014,** *47,* 3504-3511. Curk, T.; Dobnikar, J.; Frenkel, D. Optimal Multivalent Targeting of Membranes with Many Distinct Receptors. *Proc. Natl. Acad. Sci.*, **2017**, *114*, 7210-7215**.**

30. Cui, J.; Daniel, D.; Grinthal, A.; Lin, K.; Aizenberg, J. Dynamic Polymer Systems with Self-Regulated Secretion for the Control of Surface Properties and Material Healing. *Nat. Mater.*, **2015**, *14,* 790-795.

31. Datta, S.; Kato, Y.; Higashiharaguchi, S.; Aratsu, K.; Isobe, A.; Saito, T.; Prabhu, D. D.; Kitamoto, Y.; Hollamby, M. J.; Smith, A. J.; et al. Self-Assembled Poly-Catenanes from Supramolecular Toroidal Building Blocks. *Nature*, **2020**, *583*, 400–405.

32. de Oliveira, S.; Rosowski, E. E.; Huttenlocher, A. Neutrophil Migration in Infection and Wound Repair: Going Forward in Reverse. *Nat. Rev. Immunol.*, **2016**, *16*, 378-291.

33. De Silva, A. P.; Uchiyama, S. Molecular Logic and Computing. Nat. Nanotech. **2007,** *2,* 399-410.

34. Di Iorio, D.; Huskens, J. Surface Modification with Control over Ligand Density for the Study of Multivalent Biological Systems. *ChemistryOpen*, **2020**, *9*, 53-66.

35. Duan, H.; Li, J.; Zhang, H.; Qiu, F.; Yang, Y. Conformations of a Charged Vesicle Interacting with an Oppositely Charged Particle. *J. Biol. Phys.* **2018**, *44*, 1-16.

36. Dykstra, M.; Cherukuri, A.; Sohn, H.; Tzeng, S.-J.; Pierce, S. Location is Everything: Lipid Rafts and Immune Cell Signaling. *Ann. Rev. Immunol.* **2003,** *21*, 457-481.

37. Ebnesajjad, S. Polymerization Surfactants. In Fluoroplastics, Second Edition, Vol. 1 William Andrew Publishing, 2015, pp 76-94.

38. Farnoud, A.; Nazemidashtarjandi, S. Emerging Investigator Series: Interaction of Engineered Nanomaterials with the Cell Plasma Membrane, What Have We Learned from Membrane Models? *Environ. Sci. Nano*. **2019**, *6*, 13-40.

39. Feng, Z.; Wu, X.; Zhang, M. Presynaptic Bouton Compartmentalization and Postsynaptic Density-Mediated Glutamate Receptor Clustering via Phase Separation. *Neuropharmacol*., **2021**, *183,* 108622- 108631.

40. Fenz, S. F.; Smith, A.-S.; Merkel, R.; Sengupta, K. Inter-Membrane Adhesion Mediated by Mobile Linkers: Effect of Receptor Shortage. *Soft Matter*, **2011**, *7*, 952-962.

41. Friedman, A. D.; Claypool, S. E.; Liu, R. The Smart Targeting of Nanoparticles. *Curr. Pharm. Des.* **2013**, *19,* 6315-6329.

42. Furuya, M.; Kikuta, J.; Fujimori, S.; Seno, S.; Maeda, H.; Shirazaki, M.; Uenaka, M.; Mizuno, Y.; Iwamoto, Y.; Morimoto, A.; Hashmoto, K.; Ito, T.; Isogai, Y.; Kashii, M.; Kaito, T.; Ohba, S.; Chung, U.; Lichtler, A.; Kikuchi, K.; Matsuda, H.; Yoshikawa, H.; Ishii, M. Direct Cell-Cell Contact between Mature Osteoblasts and Osteoclasts Dynamically Controls their Functions in vivo. *Nat. Commun*., **2018**, *9,* 300-311.

43. Gao, J.; Zhuang, J.; Wang, F.; Raghupathi, K. R.; Thayumanavan, S. Protein AND Enzyme Gated Supramolecular Disassembly. *J. Am. Chem. Soc.,* **2014***, 136,* 2220-2223.

44. Glazier, R. Salaita, K. Supported Lipid Bilayer Platforms To probe Cell Mechanobiology. *Biochim. Biophys. Acta.,* **2017**, *1859*, 1465-1482.

45. Germain, R. T-Cell Signaling: The Importance of Receptor Clustering. *Curr. Biol.* **1997**, *7,* 640-644.

46. Gnesotto, F.S.; Mura, F.; Gladrow, J.; Broedersz, C. P. Broken Detailed Balance and Non-Equilibrium Dynamics in Living Systems: A Review. *Rep. Prog. Phys.* **2018**, *81*, 1-32.

47. Grzybowski, B. A.; Fitzner, K. Paczesny, J.; Granick, S. From Dynamic Self-Assembly to Networked Chemical Systems. *Chem. Soc. Rev.,* **2017**, *46*, 5647

48. Gucek, A.; Vardjan, N.; Zorec, R. Exocytosis in Astrocytes: Transmitter Release and Membrane Signal Regulation. *Neurochem. Res.*, **2012**, *37*, 2351-2363.

49. Herold, C.; Chwastek, G.; Schwille, P.; Petrov, E. P. Efficient Electroformation of Supergiant Unilamellar Vesicles Containing Cationic Lipids on ITO-Coated Electrodes. *Langmuir* **2012**, *28*, 5518-5521.

50. Israelachvili, J. N. Thermodynamic Principles of Self-Assembly. In Intermolecular and Surface Forces, 3rd; Elsevier Inc.: Burlington, MA, 2011; pp 503−534.

51. Jaeger, D. A.; Li, B.; Clark, T. Cleavable Double-Chain Surfactants with One Cationic and One Anionic Head Group that Form Vesicles. *Langmuir,* **1996**, *12*, 4314−4316.

52. Jones, M. R.; Mirkin, C. A. Self-Assembly Gets New Direction. *Nature*, **2012**, *491*, 42-43.

53. Katz, E.; Privman, V. Enzyme-Based Logic Systems for Information Processing. *Chem. Soc. Rev.*, **2010**, *39*, 1835-1857.

54. Katz, E. Biocomputing-Tools, Aims, Perspectives. *Curr. Opin. Biotechnol.*, **2015**, *34*, 202 -208.

55. Kelly, D. F.; Dukovski, D.; Walz, T. Monolayer Purification: A Rapid Method for Isolating Protein Complexes for Single-Particle Microscopy. Proc. Natl. Acad. Sci. U.S.A. **2008**, *105*, 4703-4708.

56. Kippo, T.; Fukuyama, T.; Ryu, I. Regioselective Radical Bromoallylation of Allenes Leading to 2-bromo-substituted 1,5-dienes. *Org. Lett.,* **2011,** *13,* 3864-3867.

57. Krishnamurthy,V. M.; Kaufman, G. K.; Urbach, A. R.; Gitlin, I.; Gudiksen, K. L.; Weibel,D. B.; Whitesides, G. M. Carbonic Anhydrase as a Model for Biophysical and Physical-Organic Studies of Proteins and Protein-Ligand Binding. *Chem. Rev.* **2008**, *108*, 946-1051.

58. Krummel, M. F.; Sjaastad, M. D.; Wulfing, C.; Davis, M. M. Differential Clustering of CD4 and CD3 ζ During T cell Recognition. *Science*, **2000**, *289*, 1349-1352.

59. Lai, K.; Wang, B.; Zhang, Y.; Zheng, Y. Computer Simulation Study of Nanoparticle Interaction with a Lipid Membrane under Mechanical Stress. *Phys. Chem. Chem. Phys.* **2013**, *15,* 270-278.

60. Lagzi, I. Chemical Robotics – Chemotactic Drug Carriers. *Cent. Eur. J. Med*., **2013**, *2*, 377-382.

61. Lehn, J.-M. Supramolecular Chemistry – Concepts and Perspectives; VCH: Weinheim, Germany, 1995; Chapter 9.

62. Lehn, J. M. Towards Self-Organization and Complex Matter. *Science*, **2002**, *295*, 2400-2403.

63. Levario, T. J.; Zhan, M.; Lim, B.; Shvartsman, S. Y.; Lu, H. Microfluidic Trap Array for Massively Parallel Imaging of Drosophila Embryos. *Nat. Protoc*., **2013**, *8*, 721−736.

64. Li, Y.; Chen, X.; Gu, N. Computational Investigation of Interaction between Nanoparticles and Membranes: Hydrophobic/Hydrophilic Effect. *J. Phys. Chem. B* **2008**, *51,* 16647-16653.

65. Liang, C.; Harjani, J. R.; Robert, T.; Rogel, E.; Kuehne, D.; Ovalles, C.; Sampath, V.; Jessop, P. G. Use of CO 2 -Triggered Switchable Surfactants for the Stabilization of Oil-in-Water Emulsions. Energy Fuels, **2012**, *26*, 488−494.

66. Lin, L.; Zeng, X. Computational Study of Cell Adhesion and Rolling in Flow Channel by Meshfree Method. *Comput. Methods Biomech. Biomed. Engin.,* **2017**, *20,* 832-841.

67. Lionello, C.; Gardin, A.; Cardellini, A.; Bochicchio, D.; Shivrayan, M.; Fernandez, A.; Thayumanavan, S.; Pavan, G. M. Politecnico di Torino. Unpublished work, **2021**.

68. Liu, J.; Xu, H.; Tang, X.; Xu, J.; Jin, Z.; Li, H.; Wang, S.; Gou, J.; Jin, X. Simple and Tunable Surface Coatings via Polydopamine for Modulating Pharmacokinetics, Cell Uptake and Biodistribution of Polymeric Nanoparticles. *RSC Adv.* **2017**, *7*, 15864–15876.

69. Liu, Y.; Jessop, P. G.; Cunningham, M.; Eckert, C. A.; Liotta, C. L. Switchable Surfactants. *Science*, **2006**, *313*, 958−960.

70. Love, J. C.; Estroff, L. A.; Kriebel, J. K.; Nuzzo, R. G.; Whitesides, G. M. Self-assembled Monolayers of Thiolates on Metals as a Form of Nanotechnology. *Chem. Rev.*, **2005**, *105*, 1103-1170.

71. Lundberg, D.; Holmberg, K. Nuclear Magnetic Resonance Studies on Hydrolysis Kinetics and Micellar Growth in Solution of Surface-Active Betaine Esters. *J. Surfactants Deterg*., **2004**, *7*, 239−246.

72. Madeley, J. D.; Richmond, R. C. A Procedure for Determining the Concentration of Hydroxyl Groups on Silica Surfaces. *Z. Anorg. Allg. Chem.,* **1972**, *389*, 92–96.

73. Martin, T. F. J. Tuning Exocytosis for Speed: Fast and Slow Modes. *Biochim. Biophys. Acta.,* **2003**, *1641*, 157.

74. McMahon, H.; Boucrot, E. Membrane Curvature at a Glance. *J. Cell Sci*. **2015**, *128*, 1065-1070.

75. McElhanon, J. R.; Zifer, T.; Kline, S. R.; Wheeler, D. R.; Loy, D. A.; Jamison, G. M.; Long, T. M.; Rahimian, K.; Simmons, B. A. Thermally Cleavable Surfactants Based on Furan−Maleimide Diels− Alder Adducts. *Langmuir*, **2005**, *21*, 3259−3266.

76. Mellander, L. J. Kurczy, M. E.; Majafinobar, N.; Dunavall, J.; Ewing, A. G.; Cans, A.-S. Two Modes of Exocytosis in an Artificial Cell. *Sci. Rep.,* **2014**, *4,* 3847-3856.

77. Merindol, R.; Walther, A. Materials Learning from Life: Concepts for Active, Adaptive and Autonomous Molecular Systems. *Chem. Soc. Rev.* **2017,** *46,* 5588-5619. Minguet, S.; Swamy, M.; Alarcon, B.; Luescher, I. F. Schamel W. W. A. Full Activation of the T Cell Receptor Requires Both Clustering and Conformational Changes at CD3. *Immunity*, **2007**, *26*, 43-54.

78. Minkenberg, C. B.; Florusse, L.; Eelkema, R.; Koper, G. J. M.; van Esch, J. H. Triggered Self-Assembly of Simple Dynamic Covalent Surfactants. *J. Am. Chem. Soc*., **2009**, *131*, 11274−11275.

79. Mishra, A.; Dhiman, S.; George, S. J. ATP-Driven Synthetic Supramolecular Assemblies: From ATP as a Template to Fuel. *Angew. Chem. Int. Ed.*, **2021**, *60,* 2740-2756.

80. Molla, M. R.; Rangadurai, P.; Antony, L.; Swaminathan, S.; de Pablo, J. J.; Thayumanavan, S. Dynamic Actuation of Glassy Polymersomes Through Isomerization of a Single Azobenzene Unit at the Block Copolymer Interface. *Nat. Chem*., **2018**, *10*, 659−666.

81. Molla, M. R.; Rangadurai, P.; Pavan, G. M.; Thayumanavan, S. Experimental and Theoretical Investigations in Stimuli Responsive Dendrimer-Based Assemblies. *Nanoscale*. **2015**, *7*, 3817-3837.

82. Mondal, J.; Friesner, R. A.; Berne, B. J. Role of Desolvation in Thermodynamics and Kinetics of Ligand Binding to a Kinase. *J. Chem. Theory Comput.* **2014,** *10,* 5696-5705.

83. Moreira, A. F.; Dias, D. R. Correia, I. J. Stimuli-Responsive Mesoporous Silica Nanoparticles for Cancer Therapy: A Review. *Micropor. Mesopor. Mat.* **2016,** *236,* 141-157.

84. Mourdikoudis, S.; Pallares, R. M.; Thanh, N. T. K. Characterization Techniques for Nanoparticles: Comparison and Complementarity upon Studying Nanoparticle Properties. *Nanoscale* **2018**, *10*, 12871-12934.

85. Nair, S.; Krebs, K. J. F.; Christianson, D. W.; Fierke, C. A. Structural Basis of Inhibitor Affinity to Variants of Human Carbonic Anhydrase II. *Biochemistry*, **1995**, *34*, 3981–3989.

86. Nagelberg, S.; Zarzar, L. D.; Nicolas, N.; Subramanian, K.; Kalow, J. A.; Sresht, V.; Blankschtein, D.; Barbastathis, G.; Kreysing, M.; Swager, T. M.; Kolle, M. Reconfigurable and Responsive Droplet- based Compound Micro-lenses. *Nat. Commun*., **2017**, *8*, No. 14673.

87. Noudeh, G. D.; Housaindokht, M.; Bazzaz, B. S. F. The Effect of Temperature on Thermodynamic Paramters of Micellization of Some Surfactants. J. Appl. Sci., **2017**, *7*, 42−52.

88. Orback, R.; Willner, B.; Willner, I. Catalytic Nucleic Acids (DNAzymes) as Functional Units for Logic Gates and Computing Circuits: From Basic Principles to Practical Applications. *Chem. Commun.*, **2015**, 51, 4144 -4160.

89. Orbán, M.; Dekepper, P.; Epstein, I. R.; Kustin, K. New Family of Homogenous Chemical Oscillators: Chlorite-Iodate-Substrate. *Nature* **1981**, *292*, 816-818.

90. Orbán, M.; Dekepper, P.; Epstein, I. R. Minimal Bromate Oscillator Bromate-Bromide-Catalyst. *J. Am. Chem. Soc.*, **1982**, *104*, 2657-2658.

91. Pasparakis, G.; Vamvakaki, M. Multiresponsive Polymers: Nano-sized Assemblies, Stimuli-Sensitive Gels and Smart Surfaces. *Polym. Chem.* **2011,** *2,* 1234-1248.

92. Pu, F.; Ren, J.; Qu, X. Recent Advances in the Construction of Nanozyme-Based Logic Gates. *Biophys. Rep.* **2020**, 6, 245-255.

93. Rábai, G.; Beck, M. T.; Kustin, K.; Epstein, I. R. Sustained and Damped pH Oscillation in the Periodate-Thiosulfate Reaction in a Continuous-Flow Stirred Tank Reactor. *J. Phys. Chem.*, **1989**, *93*, 2853-2858.

94. Rasel, M. A. I; Singh, S.; Nguyen, T. D.; Afara, I. O.; Gu, Y. Impact of Nanoparticle Uptake on the Biophysical Properties of Cell for biomedical Engineering Applications. *Sci. Rep*. **2019**, *9*, 5849-5861.

95. Ren, L.; Mellander, L.; Keighron, J.; Cans, A.-S.; Kurczy, M. E.; Svir, I.; Oleinick, A.; Amatore, C.; Ewing, A. G. The Evidence for Open and Closed Exocytosis as the Primary Release Mechanism. *Q. Rev. Biophys*., **2016**, *49*, e12-e28.

96. Reddy, A. S.; Warshavaik, D. T.; Chachisvillis, M. Effect of Membrane Tension on the Physical Properties of DOPC Lipid Bilayer Membrane. *Biochim. Biophys. Acta.,* **2012**, *1818*, 2271-2281.

97. Roca-Cusachs, P.; Sunyer, R.; Trepat, X. Mechanical Guidance of Cell Migration: Lessons from Chemotaxis. *Curr. Opin*. *Cell Biol.*, **2013**, *25*, 543-549.

98. Rodriguez-Hernandez, A. G.; Vazquez-Duhalt, R.; Huerta-Saquero, A. Nanoparticle-Plasma Membrane Interaction: Thermodyanimcs, Toxicity and Cellular Response. *Curr. Med. Chem.* **2020**, *27*, 3330-3345.

99. Rosenblum D.; Joshi, N.; Karp, J.; Peer, D. Progress and Challenges Towards Targeted delivery of Cancer Therapeutics. *Nat. Comm.* **2018**, 9, 1410-1421.

100. Rossi, G.; Monticelli, L. Gold Nanoparticles in Model Biological Membranes: A Computational Perspective. *Biochim. Biophys. Acta Biomembr.* **2016**, *1858,* 2380-2389.

101. Roy, I.; Bobbala, S.; Young, R. M.; Beldjoudi, Y.; Nguyen, M. T.; Cetin, M. M.; Cooper, J. A.; Allen, S.; Anamimoghadam, O.; Scott, E. A.; et al. A Supramolecular Approach for Modulated Photoprotection, Lysosomal Delivery, and Photodynamic Activity of a Photosensitizer. *J. Am. Chem. Soc.* **2019**, *141*, 12296–12304.

102. Sakai, K.; Imaizumi, Y.; Oguchi, T.; Sakai, H.; Abe, M. Adsorption Characteristics of Spiropyran-Modified Cationic Surfac- tants at the Silica/Aqueous Solution Interface. *Langmuir*, **2010**, *26*, 9283−9288.

103. Sanchez-Madrid, F.; del Pozo, M.A. Leukocyte Polarization in Cell Migration and Immune Interactions. *EMBO. J.* **1999**, *18*, 501-511 (1999).

104. Semenov, S. N.; Kraft, L. J.; Ainla, A.; Zhao, M.; Baghbanzadeh, M.; Campbell, V. E.; Kang, K.; Fox, J. M.; Whitesides, G. M. Autocatalytic, Bistable, Oscillatory Networks of Biologically Relevant Organic Reactions. *Nature*, **2016**, *537*, 656-660.

105. Siegel, R. Stimuli Sensitive Polymers and Self-regulated Drug Delivery Systems: A Very Partial Review. *J. Control. Release.* **2014,** *190,* 337-351.

106. Shen, H.; Miller, J. F.; Fan, X.; Kolwyck, D.; Ahmed, R.; Harty, J. T. Compartmentalization of Bacterial Antigens: Differential Effects on Priming of CD8 T-cells and Protective Immunity. *Cell*, **1992,** *92*, 535-545.

107. Shivrayan, S. Design of Responsive Oligomeric and Polymeric Interfaces for Sensing and Controlled Release Applications. Ph.D. Dissertation, University of Massachusetts-Amherst, Amherst, MA, 2021.

108. Snow, A. W.; Foos, E. E. Conversion of Alcohols to Thiols via Tisylate Intermediates. *Synthesis* **2003,** *4,* 509-512**.**

109. Springer, T. A. Adhesion Receptors of the Immune System. *Nature*, **1990**, *346*, 425-434.

110. Sreekumari, A.; Lipowsky, R. Lipids with Bulky Head Groups Generate Large Membrane Curvatures by Small Compositional Asymmetries. *J. Chem. Phys.,* **2018**, *149*, 084901-084915.

111. Stasiuk, E. N. B.; Schramm, L. L. The Temperature Dependence of the Critical Micelle Concentrations of Foam-Forming Surfactants. *J. Colloid Interface Sci.,* **1996**, *178*, 324−333.

112. Steed, J.W.; Atwood, J.L. Supramolecular Chemistry; Wiley: Chichester, UK, 2000.

113. Stjerndahl, M.; van Ginkel, C. G.; Holmberg, K. Hydrolysis and Biodegradation Studies of Surface-Active Esters. *J. Surfactants Deterg*., **2003**, *6*, 319−324.

114. Stuelten, C. H.; Parent, C. A.; Montell, D. J. Cell Motility in Cancer Invasion and Metastasis: Insights from Simple Model Organisms. *Nat. Rev. Cancer*. **2018***, 18*, 296-312.

115. Tang, J.; Quinlan, P. J.; Tam, K. C. Stimuli-Responsive Pickering Emulsions: Recent Advances and Potential Applications. *Soft Matter*, **2015**, *11*, 3512−3529.

116. Taylor, R. W.; Mahmoodabadi, R. G.; Rauschenberger, V.; Giessl, A.; Schambony, A.; Sandoghdar, V. Interferometric Scattering Microscopy Reveals Microsecond Nanoscopic Protein Motion on a Live Cell Membrane. *Nat. Photonics*, **2019**, *13*, 480-487.

117. Tambe, D. T.; Corey Hardin, C.; Angelini, T. E.; Rajendran, K.; Park, C. Y.; Serra-Picamal, X.; Zhou, E. H.; Zaman, M. H.; Butler, J. P.; Weitz, D. A.; Fredberg, J. J.; Trepat, X. Collective Cell Guidance by Cooperative Intercellular Forces. *Nat. Mater.* **2011**, *10*, 469–475.

118. Tehranibagha, A.; Holmberg, K. Cleavable Surfactants. *Curr. Opin. Colloid Interface Sci*. **2007**, *12*, 81−91.

119. Ting, C.; Wang, Z.-G. Interaction of a Charged Nanoparticle with a Lipid Membrane: Implication for Gene Delivery. *Biophys. J.* **2011**, *100*, 1288-1297.

120. Terenzio, M.; Schiavo, G.; Fainzilber, M. Compartmentalized Signaling in Neurons: From Cell biology to Neuroscience. *Neuron*, **2017,** *96*, 667-679.

121. Thongngam, M.; McClements, D. J. Influence of pH, Ionic Strength, and Temperature on Self-Association and Interactions of Sodium Dodecyl Sulfate in the Absence and Presence of Chitosan. Langmuir, **2005**, *21*, 79−86.

122. Torchi, A.; Bochicchio, D.; Pavan, G. M. How the Dynamics of a Supramolecular Polymer Determines Its Dynamic Adaptivity and Stimuli-Responsiveness: Structure-Dynamics-Property Relationships from Coarse-Grained Simulations. *J. Phys. Chem. B,* **2018**, *122*, 4169-4178.

123. Torchilin, V. Multifunctional, Stimuli-Sensitive Nanoparticulate Systems for Drug Delivery. *Nat. Rev. Drug Discov.* **2014,** *13***,** 813–827.

124. Trepat, X.; Wasserman, M.; Angelini, T.; Millet, E.; Weltz, D. A.; Butler, J. P.; Fredberg, J. J. Physical Forces during Collective Cell Migration. *Nat. Phys.,* **2009**, *5*, 426-430.

125. Tu, Y.; Peng, F.; Adawy, A.; Men, Y.; Abdelmohsen, L. K. E. A.; Wilson, D. A. Mimicking the Cell: Bio-Inspired Functions of Supramolecular Assemblies. *Chem. Rev.* **2016,** *2,* 2023-2078.

126. Viricel, W.; Mbarek, A.; Leblond, J. Switchable Lipids: Conformational Change for Fast pH-Triggered Cytoplasmic Delivery. Angew. Chem., Int. Ed. **2015**, *54*, 12743−12747.

127. Wang, M.; Ravindranath, S. R.; Rahim, M. K.; Botvinick, E. L.; Haun, J. B. Evolution of Multivalent Nanoparticle Adhesion via Specific Molecular Interactions. *Langmuir*, **2016**, *32***,** 13124-13136**.**

128. Wang, S. C.; Zambie, D. B. Fluorescence Analysis of Sulfonamide Binding to Carbonic Anhydrase. *Biochem. Mol. Biol. Edu*., **2006**, *34*, 364-368.

129. Wang, Y.; Xu, H.; Zhang, X. Tuning the Amphiphilicity of Building Blocks: Controlled Self-Assembly and Disassembly for Functional Supramolecular Materials. *Adv. Mater.* **2009**, *21*, 2849− 2864.

130. Watson, H. Biological Membranes. *Essays Biochem.* **2015**, *59,* 43-69.

131. Whitesides, G. M.; Grzybowski, B. A. Self-Assembly at All Scales. *Science*, **2002**, *295*, 2418-2421. Witt, D.; Klajn, R.; Barski, P.; Grzybowski, B. A. Applications, Properties and

Synthesis of ω-Functionalized n-Alkanethiols and Disulfides – The Building Blocks of Self-Assembled Monolayers. *Curr. Org. Chem.*, **2004**, *8,* 1763-1797.

132. Wu, C. C.; Wan, S.; Hou, W. J.; Zhang, L. Q.; Xu, J. H.; Cui, C.; Wang, Y. Y.; Hu, J.; Tan, W. H. A Survey of Advancements in Nucleic Acid-Based Logic Gates and Computing for Applications in Biotechnology and Biomedicine. *Chem. Commun.*, **2015**, *51*, 3723-3734.

133. Wu, L. G.; Hamid, E.; Shin, W. Chiang, H. C. Exocytosis and Endocytosis: Modes, Functions, and Coupling Mechanisms. *Annu. Rev. Physiol.* **2014**, *76,* 301-331.

134. Xu, F.; Pfeifer, L.; Crespi, S.; Leung, F. K.-C.; Stuart, M. C. A.; Wezenberg, S. J.; Feringa, B. L. From Photoinduced Supramolecular Polymerization to Responsive Organogels. *J. Am. Chem. Soc.* **2021**, *143*, 5990–5997.

135. Yadav, S.; Kumar, A. K.; Kumar, P. Nanoscale Self-Assembly for Therapeutic Delivery. *Front. Bioeng. Biotechnol,* **2020,** *8,* 1-24.

136. Yan, X.; Wang, F.; Zheng, B.; Huang, F. Stimuli-Responsive Supramolecular Polymeric Materials. *Chem. Soc. Rev.,* **2012**, *41*, 6042-6065.

137. Yanagisawa, M.; Yoshida, T.; Furuta, M.; Nakata, S.; Tokita, M. Adhesive Force between Paired Microdroplets coated with Lipid Monolayers. *Soft Matter* **2013**, *9,* 5891-5897.

138. Yu, B.; Tai, H. C.; Xue, W.; Lee, J. L.; Lee, R. J. Receptor-Targeted Nanocarriers for Therapeutic Delivery to Cancer. *Mol. Membr. Biol.* **2013**, *27,* 286-298.

139. Yue, Y.; Gao, Y.; Yu, Y. “Waltz” of Cell Membrane-Coated Nanoparticles on Lipid Bilayers: Tracking Single Particle Rotation in Ligand-Receptor Binding. *ACS Nano* **2018**, *12*, 11871–11880.

140. Zabock, A.; Ley, K. Hold on to your Endothelium: Postarrest Steps of the Leucocyte Adhesion Cascade. *Immunity,* **2006**, 25, 185-187.

141. D.; Aizenberg, J. Stimuli-Responsive Chemomechanical Actuation: A Hybrid Materials Approach. *Acc. Chem. Res.* **2014**, *47*, 530-539.

142. Zarzar, L. D.; Kalow, J. A.; He, X.; Walish, J. J.; Swager, T. M. Optical Visualization and Quantification of Enzyme Activity Using Dynamic Droplet Lenses. *Proc. Natl. Acad. Sci. U.S.A*., **2017**, *114*, 3821−3825.

143. Zarzar, L. D.; Sresht, V.; Sletten, E. M.; Kalow, J. A.; Blankschtein, D.; Swager, T. M. Dynamically Reconfigurable Complex Emulsions via Tunable Interfacial Tensions. *Nature***, 2015**, *518*, 520− 524.

144. Zeininger, L.; Nagelberg, S.; Harvey, K. S.; Savagatrup, S.; Herbert, M. B.; Yoshinaga, K.; Capobianco, J. A.; Kolle, M.; Swager, T. M. Rapid Detection of Salmonella enterica via Directional Emission from Carbohydrate-Functionalized Dynamic Double Emulsions. *ACS Cent. Sci.* **2019**, *5*, 789−795.

145. Zentner, C. A.; Anson, F.; Thayumanavan, S.; Swager, T. M. Dynamic Imine Chemistry at Complex Double Emulsion Interfaces. *J. Am. Chem. Soc.,* **2019**, *141*, 18048-18055.

146. Zhang, S.; Gap, H.; Bao, G. Physical Principles of Nanoparticle Cellular Endocytosis. *ACS Nano.* **2015,** *9*, 8655-8671**.**

147. Zhuang, J.; Zhao, B.; Meng, X.; Schiffman, J. D.; Perry, S. L.; Vachet, R. W.; Thayumanavan, S. A Programmable Chemical Switch Based on Triggerable Michael Acceptors. *Chem. Sci.* **2020**, *11*, 2103− 2111.

148. Zhuravlev, L. T. The Surface Chemistry of Amorphous Silica. Zhuravlev Model. *Colloids Surf.* **2000**, *173*, 1-38.

149. Zuraw-Weston, S.; Wood, D.; Torres, I. K.; Lee, Y.; Wang, L.-S.; Jiang, Z.; Lazaro, G. R.; Wang, S.; Rodal, A. A.; Hagen, M.; Rotello, V. M. Dinsmore, A. D. Nanoparticles Binding to Lipid Membranes: from Vesicle-Based Gels to Vesicle Tubulation and Destruction. *Nanoscale* **2019**, *11*, 18464-18474.